

Scanning Transmission X-ray Microscopy of Magnetotactic Bacteria

**Understanding Magnetosome Formation
and Organization using Scanning
Transmission X-ray Microscopy – X-ray
Magnetic Circular Dichroism**

By

SAMANBIR KALIRAI, B. Sc.

A Thesis

Submitted to the School of Graduate Studies

in Partial Fulfillment of the Requirements

for the Degree

Master of Science

McMaster University

© Copyright by Sam Kalirai, September 2012

MASTER OF SCIENCE (2012)
(Chemistry and Chemical Biology)

McMaster University
Hamilton, Ontario

TITLE: Understanding Magnetosome Formation and
 Organization using Scanning Transmission X-ray
 Microscopy – X-ray Magnetic Circular Dichroism

AUTHOR: Samanbir Kalirai, B.Sc. (McMaster University)

SUPERVISOR: Professor A. P. Hitchcock

NUMBER OF PAGES: xi, 101

Abstract

Magnetotactic bacteria (MTB) are ubiquitous, multi-phylogenetic bacteria that actively synthesize chains of magnetic, membrane bound; single domain magnetite (Fe_3O_4) or greigite (Fe_3S_4) crystals, termed magnetosomes in order to better navigate to their preferred chemical environment using the Earth's magnetic field. Discovered in 1963, the field is now focused on understanding magnetosome chain formation and associated processes through genetic studies as well as analytical techniques such as Transmission Electron Microscopy (TEM) and Scanning Transmission X-ray Microscopy – X-ray Magnetic Circular Dichroism (STXM-XMCD).

This thesis performed studies on *Candidatus Magnetovibrio blakemorei* strain MV-1 using STXM at the C 1s, O 1s, Ca 2p and Fe 2p edges. STXM-XMCD was used to determine the magnetism of individual magnetosomes and quantitatively determine magnetic properties such as the magnetic moment of individual chains. A sub-population of MV-1 cells was identified as having anomalous magnetic orientations of magnetosome sub-chains when separated spatial gaps. The frequency of this event and the underlying implications to magnetosome formation are discussed.

Acknowledgments

I am extremely grateful to Prof. Adam Hitchcock for his guidance and mentorship. Adam gave me my first taste of scientific research and has instilled in me a great enthusiasm about scientific learning and teaching that I hope to now pay forward. Despite the amount of scientific knowledge I have amassed under him, I am most grateful for the ideas of what scientific research means that he has endowed in me. Adam has also provided extremely insightful discussion and feedback whilst giving me the best possible environment to explore and think independently which I believe has made me a better scientist. I hope that everyone is able to experience this freedom, independence and support in their scientific careers. Thank you Adam.

I would also like to thank Prof. Dennis A. Bazylinski. What started as collaboration has turned into what I believe are now a mentorship and a friendship. Dennis' enthusiasm for MTB research is remarkable and after he graciously invited Adam and me to see his lab it was obvious why. Gracious is a word that defines Dennis. Despite his limited time, he has given us the utmost support and mentorship. He has prepared and sent samples on a dime, happy to drop everything else on his plate. Dennis has travelled far and wide to collect MTB samples so we could look at them in the STXM. He has provided us with support in writing papers, writing reports and writing proposals. All of this support for what could be such a simple collaboration and he has not once said no.

For this I am extremely grateful to have had you as a collaborator and a friend. I cannot thank you enough Dennis.

Furthermore I would like to thank the support staffs that have helped me at the Advanced Light Source, Canadian Light Source and McMaster University. In particular I would like to thank Jian Wang, Chithra Karunakaran, Tolek Tyliczszak and Marcia Reid for their tireless support.

I would also like to thank my group members, past and present for their insightful discussions, camaraderie and for providing continual laughter and spiritual uplift in the lab. Thank you Dr. Bonnie Leung, Dr. Ebrahim Najafi, Dr. Glyn Cooper, Dr. Adam Leontowich, Karen Lam, Katie Harding, Dr. Viatcheslav Berejnov, Victoria Ju, Dr. Vincent Lee, Zhisheng Qin, Xiaohui Zhu.

I want to thank my family and friends. My parents, Balbir and Sukhminder have unconditionally supported me throughout my undergraduate and graduate studies. Whether it be monetary, driving me to the airport, coming to visit me or simply asking me how I am doing they have always been there for me. For that reason and many others, I thank them. Dave, Spencer, Rob, Erik, and Volodymyr I would like to thank you for being such great roommates.

Lastly, thank you Jennifer J. Hobbs.

Table of Contents

<i>Descriptive Note</i>	<i>iii</i>
<i>Abstract</i>	<i>iv</i>
<i>Acknowledgments</i>	<i>v</i>
<i>Table of Contents</i>	<i>vii</i>
<i>List of Acronyms and Symbols</i>	<i>x</i>
Chapter 1 Introduction	11
1.1 Magnetotactic Bacteria	2
1.1.1 <i>Magnetoaerotaxis, the diversity of magnetosomes and MTBs</i>	4
1.1.2 <i>Characteristics of Magnetosomes and Magnetosome Chains</i>	8
1.1.3 <i>Mechanisms of Magnetosome Formation</i>	13
1.1.4 <i>Magnetism of MTB</i>	18
1.2 Magnetism of Magnetite	19
1.3 X-ray Magnetic Circular Dichroism	21
1.3.1 <i>Near Edge X-ray Absorption Fine Structure Spectroscopy</i>	22
1.3.2 <i>Spin Selective X-ray Absorption: XMCD</i>	23
1.3.3 <i>Theory of XMCD</i>	24
1.3.4 <i>XMCD of Magnetite and Biogenic Magnetite at the Fe L_{2,3} edge</i>	27
1.4 The Scanning Transmission X-ray Microscope and Beamlines	31
1.5 Goals of this Thesis	36

Chapter 2	Experimental	39
2.1	Magnetotactic Bacteria Samples.....	40
2.1.1	<i>Preparation of Magnetotactic Bacteria Sample</i>	40
2.1.2	<i>Characteristics of Magnetotactic Bacteria used in these studies.</i> ..	42
2.3	Transmission Electron Microscopy of MTB	44
2.2.1	<i>Sample preparation of MV-1 thin sections</i>	44
2.2.2	<i>Transmission Electron Microscopy of MTB</i>	45
2.3	Sample Mounting	45
2.3.1	<i>Cut-back and Wedge Plates</i>	47
2.3.2	<i>Tomo-rotator Stub</i>	49
2.4	Measurements and Analysis of MTB	50
2.4.1	<i>STXM Measurements of MTB</i>	52
2.4.2	<i>Fe 2p - XMCD measurements of magnetosomes</i>	54
2.5	Data Analysis Using aXis2000	54
2.5.1	<i>Edge Chemical and XMCD Maps</i>	54
2.5.2	<i>Fe 2p and XMCD Spectra of Magnetite</i>	56
2.5.3	<i>Stack Analysis of XMCD Stacks</i>	57
Chapter 3	Quantifying the Magnetic Moment of a Single Magnetosome Chain	61
Chapter 4	Anomalous Magnetic Orientation in Single Cell Magnetosome Sub-chains.....	72
4.1	Magnetic Orientation Reversal of MV-1 Cells.....	74

4.2 Proposed Mechanisms of Orientation Reversal	83
Chapter 5 Summary and Future Work	88
5.1 Summary of Thesis	89
5.2 Future Work	91
5.2.1 <i>Tomo-rotator Stub</i>	92
5.2.2 <i>Mechanisms of Magnetosome Formation – Genetic Mutants</i>	95
References	96

List of Acronyms and Symbols

Å	Angstrom
ALS	Advanced Light Source
AMB-1	<i>Magnetospirillum magneticum</i>
B	Magnetic Field
CLS	Canadian Light Source
δ_{rN}	Width of the Most Outer Zone (Nth) of a Zone Plate
Δr	Diffraction Limited Spatial Resolution
D	Zone Plate Diameter
EPU	Elliptically Polarizing Undulator
f	Focal Length
G	Gauss
H	Magnetic Field Strength
I_0	Incident Photon Intensity
K	Kelvin (unit of temperature)
LCP	Left Circularly Polarized Light
MAI	Magnetosome Genome Island
MC-1	<i>Magnetococcus Marinum</i>
MM	Magnetosome Membrane
MS-1	<i>Magnetospirillum magnetotacticum</i>
MSR-1	<i>Magnetospirillum gryphiswaldense</i>
MTB	Magnetotactic Bacteria
MV-1	<i>Candidatus magnetovibrio blakemorei</i>
μm	Micrometre, 1×10^{-6} metre
NEXAFS	Near Edge X-ray Absorption Fine Structure
nm	Nanometre, 1×10^{-9} metre
OATZ	Oxic-Anoxic Transition Zone
PCA	Principal Components Analysis
RCP	Right Circularly Polarized Light
STXM	Scanning Transmission X-ray Microscopy
SVD	Singular Value Decomposition
TEM	Transmission Electron Microscopy
TEY	Total Electron Yield
XMCD	X-ray Magnetic Circular Dichroism
XAS	X-ray Absorption Spectroscopy
ZP	Zone Plate

Chapter 1

Introduction

This chapter introduces the history of magnetotactic bacteria and their importance in the field of microbiology as an example of prokaryotic biomineralization of magnetosomes. The current studies of magnetotactic bacteria and the underlying questions surrounding the formation and organization of magnetosomes are discussed. Magnetite and its magnetic properties are introduced in section 1.2. Section 1.3 focuses on the magnetically sensitive technique known as X-ray Magnetic Circular Dichroism, its underlying theory and its use to probe the magnetism of magnetite. The basic operation of the Scanning Transmission X-ray Microscope as a probe for magnetism in magnetosome chains is introduced. Finally, the scope of the thesis is summarized.

1.1 Magnetotactic Bacteria

Magnetotactic bacteria (MTB) represent a diverse multiphylogenetic population of bacteria that are linked by the ability to form organelles termed magnetosomes. Magnetosomes consist of magnetite (Fe_3O_4) or greigite (Fe_3S_4) particles that are enclosed by a lipid membrane [HBG&91] and are actively synthesized by MTB to form a chain. Magnetosome chains are utilized by MTB in order to navigate to their preferred chemical environments in stratified media; this magnetically sensitive navigation is known as magnetotaxis or magnetoaerotaxis [B95, FB94]. MTB are found in both marine and fresh-water environments [B63a, B63b, B1975, FB80, FBW79], typically where there is a vertical chemical redox environment. Thus magnetotaxis is advantageous with respect to competitive species as MTB are able to reduce the difficulty in searching for the right environmental conditions by navigating along the Earth's magnetic field lines [FB94].

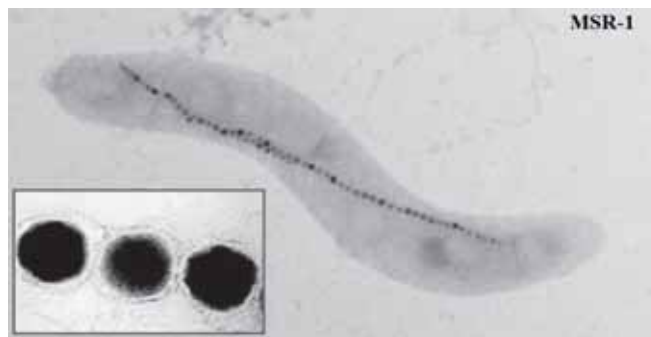


Figure 1-1 – TEM image of Magnetotactic Bacteria strain *Magnetospirillum magnetotacticum*, MSR-1. Inset shows close up of magnetosome organelle. (Adapted from [JS09])

MTB were first discovered in 1963 by Bellini [B&63a, b] who identified a population of magnetically sensitive bacteria by noting that MTB respond to an applied magnetic field and, in the absence of a field, persistently swim north. However, it was not until the independent discovery of MTB in 1975 by Blakemore [B1975] that the existence of MTB became widely known. Blakemore, like Bellini, saw that MTB swim toward magnetic north. Even as a drop on the microscope slide is rotated MTB swim pervasively towards North. This behaviour was later attributed to chains of magnetite crystals that are actively biomineralized by MTB. Blakemore noted that there were several morphotypes of magnetotactic bacteria with different cell shapes as well as different sizes ranging from 1-3 μm . Each had its own linear chain of dense crystal particles [B75]. Using Mössbauer Spectroscopy, it was confirmed that the crystals were magnetite which is ferrimagnetic, allowing Blakemore to conclude that magnetosomes are indeed responsible for magnetotaxis [FBW79].

The MTB microbiology community has since moved on to the understanding of processes related to biomineralization of magnetosome chains and similar functions. Genetic studies represent much of the current active research regarding magnetosome biomineralization. In particular, studies have focused around a tightly associated set of genes termed the magnetosome gene island (MAI) [UKS&05] which are believed to be responsible for different aspects of magnetosome chain organization and formation.

1.1.1 – Magnetoaerotaxis, the diversity of magnetosomes and MTBs

MTB use the local geomagnetic field as a navigational aide in positioning themselves in an optimum chemical environment for growth. Stratified chemical environments produce a vertical chemical gradient where the oxygen concentration diminishes farther down from the air-water interface. In conjunction, more reductive species such as sulfides increase in concentration as the distance from the air-water interface increases [SSF&04]. The vertical distribution of the redox environment challenges microbes to find and stay within their optimal environment. MTB in general are microaerophilic or anaerobic; accordingly, they are typically found in the sedimentary region where oxic and anoxic environments merge, or just below the Oxic-Anoxic Transition Zone (OATZ) [DRS92]. This allows for the uptake of a small but necessary amount of oxygen while remaining in a largely anoxic environment. Magnetotaxis aids MTB by using the inclined geomagnetic field lines as a navigational axis. Typically bacteria use a chemo-sensitive random-walk approach to find an optimum chemical environment, but this requires navigation within a volume [BF04]. By passively aligning with the inclined geomagnetic field lines MTB reduce a three-dimensional search problem to a one-dimensional search problem [BF04], thereby probing the vertical chemical gradient axis more efficiently. Magnetoaerotactic behaviour (redox sensitive navigational response with the aid of magnetism) provides MTB with a distinct advantage over other aerotactic bacteria by allowing them to find their preferred environment significantly faster than similar strains of

non-magnetic mutant bacteria in an oxygen gradient [SSP&06]. In doing so, it is presumed that MTB are the first to reach chemically optimal zones where replication and growth may occur.

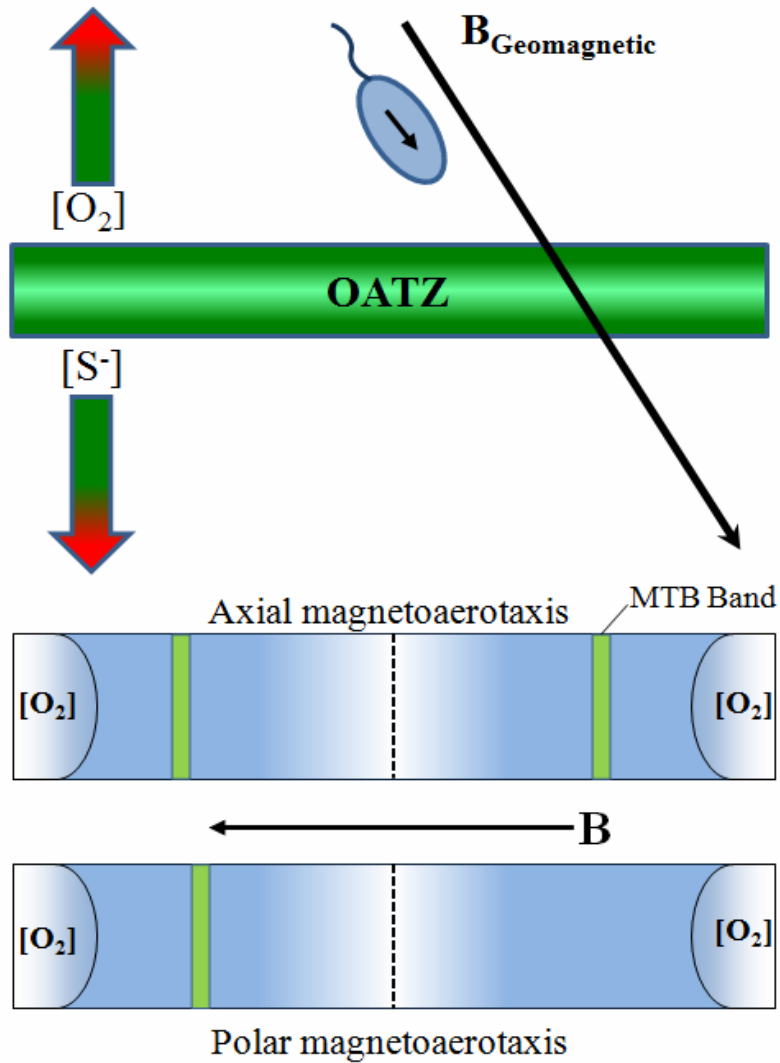


Figure 1-2 – a. Principle of magnetoaerotaxis showing MTB aligning along the Earth's geomagnetic field to find the Oxic-Anoxic Transition Zone b. Showing axial and polar magnetotaxic band formation in an open-ended capillary. (Adapted from [LFB11])

MTB passively align along geomagnetic field lines; however, the motility of cells is generated by flagellar motion [BF04]. This leads to several modes of magnetoaerotactic motility. Axial magnetotactic behaviour uses the geomagnetic field line as an axis along which motion occurs in both directions. Axial MTB in an open ended capillary are found to produce two aerotactic bands even in the presence of a unidirectional magnetic field [BFK80]. The two bands represent the preferred redox environment which occurs in two bands due to the presence of an air-water interface at each end of the tube. MTB with a polar magnetotaxis pervasively swim toward one pole. Converse to axial MTB, polar MTB will form one band in an open ended capillary which is placed in a magnetic field [SB06], despite the presence of two bands of redox optimal environments. Anoxic environments typically are directed away from surface water where oxygen is cycled at the air-water interface. Thus in the northern hemisphere it is beneficial for polar MTB to be “north seeking” and conversely in the southern hemisphere, “south seekers” are preferred. At the equator where the geomagnetic field lines have no vertical component, both north and south seeking MTB have been found [FBT&81] which further indicates that the magnetosensitive response is used as an aid to aerotactic or chemotactic responses. Despite the obvious disadvantages to the opposing behaviour in each hemisphere, south seeking MTB have been found in the northern hemisphere [SBE06]. These results suggest that, although the model for magnetoaerotaxis is a logical one, it may not fully describe the functionality and purpose of magnetosome chains.

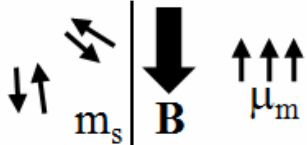
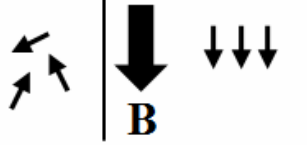

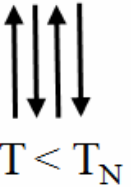
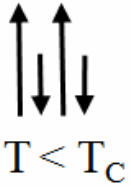
To utilize a magnetoaerotactic strategy, MTB have developed a sophisticated mechanism of highly controlled biomineralization of magnetic vesicles termed magnetosomes. Magnetosomes are invaginations of the inner cell membrane which enclose single domain crystals of magnetite [BGF94]. Magnetosomes are generally ordered into discrete linear chains. This arrangement amplifies the net magnetic vector thus allowing the cell to adopt a single magnetic orientation that can be used for magnetotactic response. Current studies of MTB are focused on the specific proteins and mechanisms of the formation of magnetosome chains [KLN&06, SGF&06, AWM03]. Here, we present detailed information on the magnetic characteristics of magnetosomes and magnetosome chains. The mechanisms of magnetosome formation are discussed in section 1.1.3.

Magnetosome formation is a highly ordered and controlled process. It is thought that MTB have the ability to control many aspects of magnetosomes including size distribution, shape, composition and phase [FSA&11]. Although magnetosome formation is a highly controlled and reproducible process, different MTB have a wide variation in the physical attributes of their magnetosomes. Thus, although the process and outcome for one strain of MTB is highly reproducible, there is a very diverse range of magnetosome structures in different MTB species.

1.1.2 – Characteristics of Magnetosomes and Magnetosome Chains

All magnetosomes to date have been found to be either, magnetite, an iron oxide, Fe_3O_4 or greigite, its sulphide counterpart, Fe_3S_4 . Magnetosomes have a small size distribution of approximately 35 to 120 nm [BF04] which lies in the range where single magnetic domains are stable [BB75]. Smaller, premature magnetosomes

Table 1-1 – The nature of magnetic ordering in materials in the presence and absence of an external magnetic field. Examples of real materials with each property are included.

Magnetic Ordering	Characteristics	Illustration	Examples
Diamagnetic	Electron pairs with no long range ordering in the absence of magnetic field. Weakly oppose presence of an external field.		Water, organic material, silver, Gold
Paramagnetic	Unpaired electrons with no ordering in the absence of magnetic field. Magnetic moment induced by external magnetic field is weak.		Aluminum, Copper, Platinum
Ferromagnetic	Strong ordering of magnetic moments over long range below Curie temperature (T_C). Strong parallel alignment with an external magnetic field. May remain magnetized after field is removed.		Iron, Nickel, Gadolinium
Antiferromagnetic	Strong ordering of magnetic moments over long range below a Neel temperature (T_N). Alignment ordering is such that spins order in opposite directions giving the bulk a zero net magnetization.		Terbium, Iron-Manganese Alloy, Hematite
Ferrimagnetic	Antiferromagnetic-like ordering that has an unequal magnitude of opposing moments, thus giving the bulk a net magnetization below a transition temperature.		Magnetite, RbNiF_3 , GdCo_5

can be present in the cell and are superparamagnetic. Table 1-1 shows the types of magnetic ordering possible for materials. Magnetite is ferrimagnetic, meaning that it has a net magnetic moment. However if a magnetite crystal is smaller than the single domain limit, the thermal energy is larger than the magnetic anisotropy energy and the magnetism of the material is time averaged to zero as it fluctuates along the magnetic easy axis. In the single domain limit, the anisotropic energy is larger than the thermal energy and the magnetic moments align coherently such that there is a net magnetic moment of the material. However, if the material becomes large enough, domain wall formation and multi-domain formation occurs to minimize the internal energy of the material. When this occurs, each domain is coherently aligned, but in the absence of an external field, each domain is oriented in different directions leading to a smaller or zero bulk magnetic moment.

Each magnetosome is aligned along a fibrous protein filament [KLN&06] such that a chain of magnetosomes is formed end-on. This end-on orientation of the magnetosomes allows the cell to adopt a single orientation and thus acts as the navigational compass for magnetoaerotactic motility by orienting the cell in the geomagnetic field. The end-on orientation maximizes the cell magnetic moment which is the sum of the magnetic moments of the individual magnetosomes [B82]. Furthermore, since the magnetism of each magnetosome is single domain, it is volume maximized. Biochemical control over the size of magnetosomes is necessary so that smaller superparamagnetic particles or larger multiple domain

particles are not created. If superparamagnetic particles dominated the chain, MTB would not be able to adopt a single fixed orientation due to thermal fluctuations in the net magnetic moment of the cell. Conversely, larger, multi-domain particles would diminish or nullify any magnetic moment as the domains within each magnetosome would adopt multiple magnetic orientations.

Magnetosomes from different strains of MTB adopt many different shapes. Figure 1-3 shows some of the crystal habits that are known to be present in MTB. There are many final shapes that are consistent with the F_{d-3m} symmetry of magnetite.

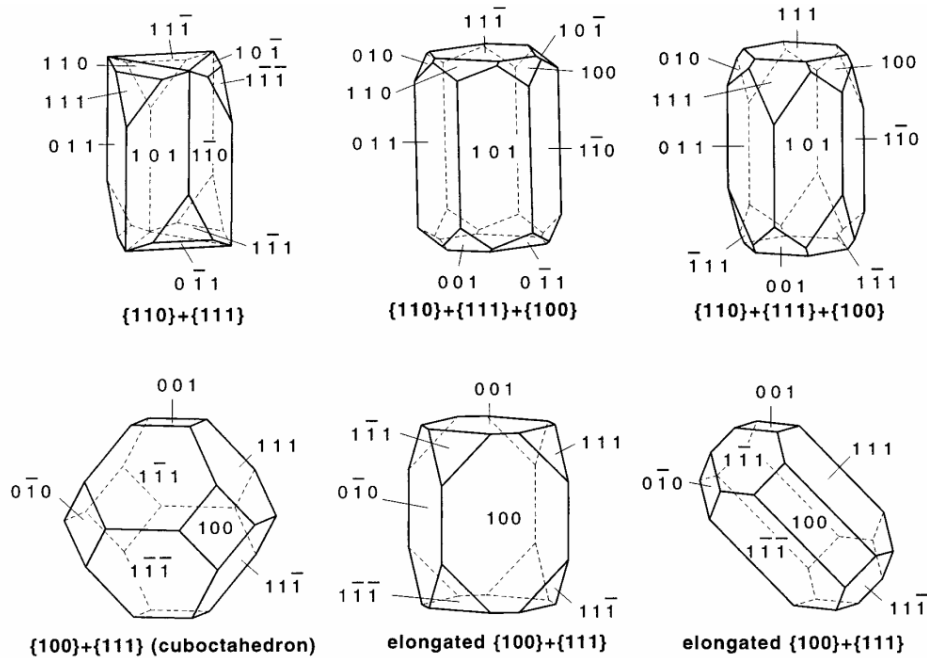


Figure 1-3 – Combinations of faces (cube {100}, octahedron {111} and dodecahedron {110}) that can be made from the F_{d-3m} symmetry of magnetite. (adapted from [DPH&98])

These are combinations of the cube [1 0 0], octahedron [1 1 1] and dodecahedron [1 1 0] faces that lead to the diversity of shapes present [DPH&98].

Most of the crystal habits for magnetosome magnetite appear to be elongated along one face, leading to an anisotropic crystal shape. Interestingly, the cells typically align the long axis of the crystals along the magnetosome chain. Shape anisotropy is an example of magnetic anisotropy which may allow for an easy axis of magnetization [DMF&98], thereby ensuring an alignment of the magnetic moment along the chain, or long axis. Although the mechanism of shape anisotropy biosynthesis is not fully understood, it is thought that anisotropic ion

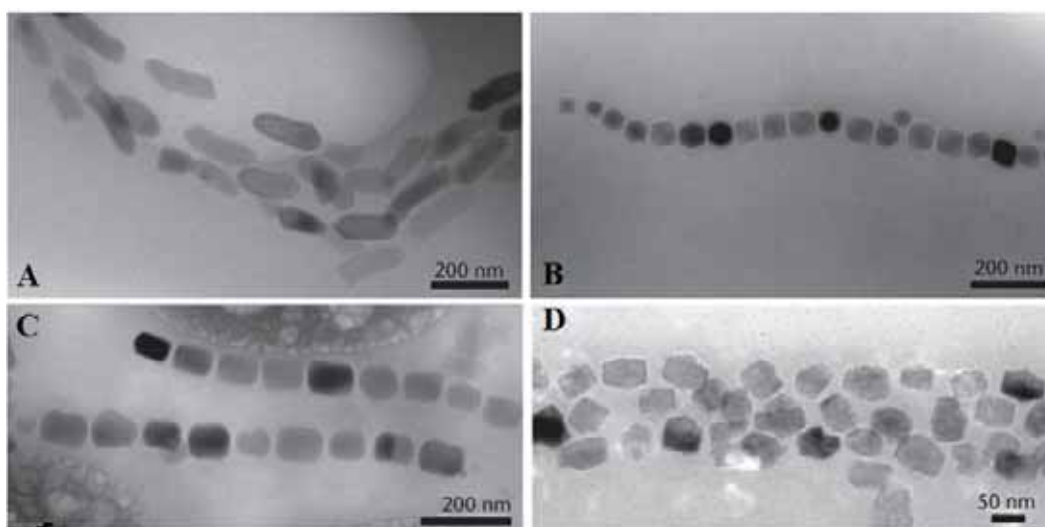


Figure 1-4 – TEM micrographs of different magnetosome shapes from MTB strains. Shapes include a) bullet or tooth-shaped magnetite b) cuboctahedral magnetite c) elongated prismatic magnetite d) disordered-structure greigite crystals. (Adapted from [LFB11])

flux into the membrane invagination during crystal growth allows for the elongated habits observed [MF89]. One extreme case of crystal shape anisotropy is the tooth or bullet-shaped magnetosomes present in some MTB [TBS&94]. These shapes are seen in figure 1-4 along with other examples of magnetosome crystals.

Magnetosomes also exhibit a high chemical and structural purity. This is due to the fact that magnetosomes are created within a membrane invagination in which the magnetosome formation conditions are dictated by tightly associated and highly selective proteins. Synchrotron x-ray diffraction of magnetosomes, biogenic magnetite and synthetic magnetite showed that the lattice parameters of magnetosomes are different from that of synthetic magnetite [FSA&11]. This is attributed to magnetosomes being structurally and chemically pure compared to the oxidized abiogenic magnetite. Furthermore, biogenically produced magnetite after isolation from the cell environment showed similar lattice parameters as the abiogenic magnetite. This implies that MTB have a high degree of control on the chemical conditions within the magnetosome membrane in order to maintain strict pH and eH conditions [FSA&11]. Stoichiometric purity of magnetosomes is a beneficial characteristic as the magnetic moment of magnetite is maximized at stoichiometry [FSA&11].

Candidatus Magnetovibrio Blakemorei, MV-1 bacteria is the central MTB that was studied in this thesis. MV-1 is one of two cultured marine species of magnetotactic bacteria that belong to the Alphaproteobacteria phylum along with

Magnetococcus marinus MC-1. MV-1 was first isolated by Bazylinski et al. [BFG&88]. Cells are typically small, from 1-5 μm by 0.2-0.5 μm and possess single flagella [SMB&90]. Thus MV-1 are polar magnetotactic bacteria. They synthesize single chains of magnetite magnetosomes with an average size of 53 by 35 nm as determined by TEM studies [SMB&90]. Magnetosomes of MV-1 are elongated pseudohexahedral prismatic crystals. The strain is one of two representative marine Alphaproteobacteria that use the magnetoaerotactic response suggesting that a horizontal gene transfer of the MAI gene island [JKS&09] occurred previously from other magnetotactic freshwater Alphaproteobacteria.

1.1.3 – Mechanisms of Magnetosome Formation

The discovery and elucidation of the magnetosome gene island (MAI) [UKS&05] has allowed for functional analysis of genes implicated in magnetosome formation. By understanding the function of the individual genes in the MAI a clearer understanding of the function of magnetosome chains may be discovered. The MAI represents a highly conserved section of the MTB genome that has the specific functionality associated with magnetosome membrane formation, ion transport, seeding, shape, size and crystallinity control. *Mam*, *Mts* and *Mms* genes have been identified for several of these functions. However, one of the challenges with the functional analysis of magnetosome genes is that approximately half of the MAI-encoded proteins do not have homologs of known

function in other organisms [K07]. Furthermore, studies have shown that the organization and overall structure of the MAI is not completely consistent between MTB strains, suggesting multiple lineage and prolific horizontal gene transfer among bacteria. This is also likely the origin of the diversity in magnetosome characteristics and in MTB species. Nevertheless, functional analysis and gene deletion mutant studies have begun to shed light on the complex biochemical processes involved in magnetosome biosynthesis. Some of these findings are summarized below.

Magnetosome membranes (MM) are known to be formed prior to crystal synthesis. MM are invaginations of the cytoplasmic or inner membrane. The accumulation of iron is >4% by dry weight [FBM&07] and thus strict control over the iron uptake into the cell is necessary in order to avoid harm to the cell from excessive concentrations of intracellular iron [JS09]. Both ferrous and ferric iron are believed to be taken in by certain cation diffusion facilitators, such as *MamB* and *MamM* which allow for a supersaturation of iron within the MM [FBM&07]. Compartmentalization into the membrane is necessary in order to control the physicochemical characteristics such as pH, eH and supersaturation levels in order to form magnetite and not other unwanted iron oxides [FS08]. Komeili *et al* showed that magnetosome membranes are present in a cell prior to the formation of magnetite within the invaginations [KVB&04]. Deletion of the *mamA* gene in the MTB strain, *Magnetospirillum magneticum* AMB-1 showed no difference in the size, shape or rate of formation of individual magnetite crystals [KVB&04].

However, the deletion strains of *mamA* produced only about half of the magnetosomes on average despite the presence of the same amount of magnetosome membranes when compared to the wild type strains of AMB-1 [K07]. However, many wild type MTB exhibit short magnetosome chains depending on environmental conditions; thus, the function of *mamA* is not fully understood. The function of homologous proteins in other organisms point to the possibility that the *mamA* protein does not have a specific enzymatic function but is used to signal events along the magnetosome formation pathway as similar proteins are known to promote protein-protein interactions [BL99].

Arakaki *et al* identified a set of proteins Mms5, Mms6, Mms7 and Mms13 in AMB-1 as being tightly associated to the magnetite crystals within the magnetosome membrane [AWM03]. *In vitro* synthesis of magnetite in the presence of Mms6 protein showed that it can control the size of the magnetite crystals produced to yield similar crystals to those seen in MTB [AWM03]. Functional analysis of the Mms6 protein shows that it contains regions similar to those implicated in the biomineralization of calcium minerals [K07].

MamJ and MamK proteins have been extensively studied in MTB strain MSR-1. Deletion of the MamJ gene resulted in magnetosome formation but not organization of the magnetosomes into a chain [SGF&06]. Instead, the magnetosomes aggregated into a cluster [SGF&06] which is the expected lowest energy organization of loose magnetite nanoparticles. Electron cryo-tomographic reconstructions of the MamJ deletion mutant show that the cytoskeletal filaments

that adjoin magnetosome particles were still intact [SGF&06]. MamJ is implicated in the interaction of magnetosomes with the cytoskeletal filament which allows the magnetosomes to adopt the necessary linear orientation [K07].

The cytoskeletal filaments are thought to be composed of MamK protein. MamK is an actin-like protein with many homologs which are implicated in cell shape and cell polarity [G05]. MamK overexpressed in *E. coli* showed that it has an inherent predisposition to form into filaments [PSB&06]. Green-fluorescent protein tagging of MamK showed that the filaments are localized around magnetosomes in a linear shape. Electron cryo-tomographic studies showed the presence of cytoskeletal filaments around the magnetosome chain [KLN&06]. These bundled filaments seem to allow magnetosomes to adopt a linear orientation, furthermore the filaments were of similar sizes to the MamK homologs found in other bacteria thus implicating MamK as a structural and organizational mediator of magnetosome chains [K07]. MamK mutant strains were shown to have all the same features of magnetosomes as the wild type strain. However, magnetosome chains were not formed, they were dispersed within the cell and did not appear to have filaments close to the magnetosomes [KLN&06]. Komeili *et al* [K07] have proposed a model by which MamJ takes the role of mediating interactions between the cytoskeletal filaments, composed of MamK, and the magnetosomes. However, because of the large difference in the magnetosome organization of the deleted MamJ and MamK strains there is a possibility that the two do not have an interaction and that there is a different

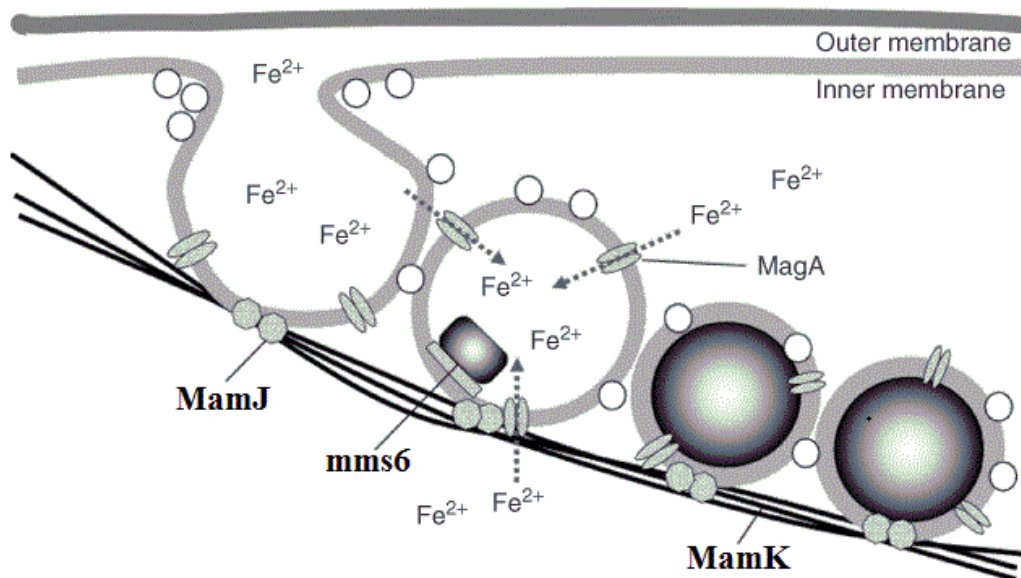


Figure 1-5 – Schematic of the formation of magnetosomes which are tethered to the MamK filament by MamJ proteins. The *mms6* protein helps seed magnetite formation. (Adapted from [GRS&12])

mode of action for the two proteins [K07]. One such proposition put forth by Komeili is that MamK may mediate membrane synthesis within the chain such that in the absence of MamK lipids may interfere with the chain growth and be inserted between magnetosome chains therefore creating gaps within chains [K07].

From these studies a general idea of magnetosome formation, structure and organization from a biochemical standpoint has begun to appear. Figure 1-5 shows a working model given the known information about gene function in relation to magnetosome formation. However, much of the work is preliminary, and there remain many questions about the function of the genes mentioned above

as well as other MAI genes that have not been studied. Much of these genetic studies have come within the last ten years, and there is now a great push towards understanding the function of each gene implicated in magnetosome formation. In doing so genetic studies have been complimented by analytical techniques such as transmission electron microscopy (TEM) [KLN&06] and Scanning Transmission X-ray Microscopy (STXM) [LHO&10, KLB&12] to aide in understanding the outcomes of such studies.

1.1.4 - Magnetism of MTB

Several magnetically sensitive techniques have been used to explore the magnetism of MTB cells. Total magnetic moments of ensembles of MTB cells have been measured using techniques such as remanence measurements [PDM&95] and magnetic force anisotropy [PSM&95]. Furthermore, electron holography has been used to measure the magnetic moment at the individual cell level [DMF&95]. Remanence measurements on *Magnetospirillum gryphiswaldense* MSR-1 showed that there is a bulk coercive force of 303 Oe and that the hysteresis curve is square shaped, indicating that cells contain single-domain particles [PDM&95]. The coercive force is similar to the expected model of a chain of spheres. However, this study was unable to observe the chain length of the cells so that chain length and coercive force could not be correlated. Dunin-Borkowski *et al.* used electron holography to map the magnetic flux around magnetosome chains [DMF&98]. Electron holography is a TEM based technique that can map phase shifts resulting from electric and magnetic field

interactions with the probing electrons. When compared to a clear passing beam, the subtle deflections of the beam can be related to the magnetic and electric fields of the sample thereby giving qualitative results to the fields. *Magnetospirillum magnetotacticum*, MS-1 and MV-1 strains were examined using electron holography. A total coercive field of an MV-1 chain was measured to be 300 to 450 Oe [FB80]. Furthermore, the magnetic moment of the MV-1 chain was $7 \times 10^{-16} \text{ A m}^2$ which is the same per unit length as that for MS-1 suggesting that the magnetic moment is saturated and that each magnetosome is single domain [FB80].

1.2 – Magnetism of Magnetite

Magnetite (Fe_3O_4), also known as lodestone, was the first known magnetic material. The properties of magnetite are summarized in several reviews [DZJ&99, C54, MM00]. Magnetite has the IUPAC name ferrous ferric oxide, denoting the presence of mixed valence iron. Magnetite has a ferrimagnetic ordering with a Curie temperature of 858 K with a reverse spinel structure. Iron found in magnetite has a mixed valence character with Fe(II) and Fe(III) ions present in two different sites. Fe(III) ions have a $3d^5$ electron occupancy, and are found in both octahedral and tetrahedral environments. Fe(II) is $3d^6$ and thus has preference for Jahn-Teller distorted octahedral sites. The overall structure of magnetite can be written as $\text{Fe}^{3+}_{(\text{Td})}\text{Fe}^{3+}_{(\text{Oh})}\text{Fe}^{2+}_{(\text{Oh})}$. At room temperature the space group of magnetite is F_{d-3m} , however, a switch to monoclinic symmetry is

observed at 122 K. Additionally, at 122 K, there is a charge ordering known as the Verwey transition below which Fe(III) and Fe(II) ions gain a discrete and regular ordering and display insulating behaviour in certain crystallographic directions. Above the Verwey temperature the thermal energy is large enough to destroy this ordering and the electric conductivity is restored in all crystallographic directions. There are several exchange pathways that lead to the ferrimagnetic behaviour observed. Octahedral sites are situated adjacent to each other with central iron atoms at an approximate 180° angle, which leads to a direct exchange of the extra electron in the octahedral – d^6d^5 system allowing for long range ferromagnetic ordering of the octahedral sites. Conversely a superexchange pathway through oxygen ligands between the octahedral and tetrahedral sites leads to a

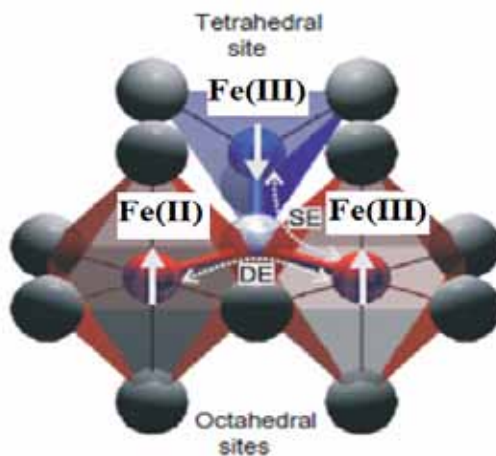


Figure 1-6 – Schematic showing the superexchange (SE) and direct exchange (DE) pathways between the tetrahedral and octahedral sites of magnetite. (Adapted from [SS06])

antiferromagnetic ordering. Overall the magnetic moment of magnetite is $4 \mu_B$.

Fe(III) has a magnetic moment of $5 \mu_B$. However the tetrahedral and octahedral sites cancel out because of the opposite ordering leaving the magnetic moment of Fe (II), which is $4 \mu_B$.

Despite the ancient knowledge of magnetite, its electronic and magnetic structure is highly complex and still not completely understood. Many groups have studied the nature of the Verwey transition and its implications to spectroscopy and magnetism with conflicting results. Furthermore, calculations of the electronic structure and associated spectroscopies of magnetite are generally in poor agreement with experiment.

1.3 – X-ray Magnetic Circular Dichroism

X-ray Magnetic Circular Dichroism (XMCD) is a magnetically sensitive spectroscopy that is a subset of x-ray absorption spectroscopy (XAS). Excitation by circularly polarized x-rays allows for spin selective transitions of an electron from a non-zero angular momentum core level into empty or partially filled orbitals at and above the Fermi energy. Synchrotron based Scanning Transmission X-ray Microscopy (STXM) provides the additional ability to measure X-ray Absorption Spectroscopy (XAS) and XMCD from individual magnetosomes in a single cell [LHO&10, KLB&12]. Thus STXM-XMCD represents an excellent probe of the magnetic properties of magnetosome chains which can give insights into its mechanisms of formation and function. By overlaying the magnetically

sensitive XMCD technique with chemically sensitive NEXAFS spectromicroscopy, for example at the C1s N1s and O1s edges, STXM-XMCD provides unique information about this fascinating example of biomineralization.

1.3.1 – Near Edge X-ray Absorption Fine Structure Spectroscopy

NEXAFS spectroscopy probes the electronic structure of molecules or materials by excitation of core electrons into empty valence orbitals [S92]. NEXAFS is typically considered to be a purely spectroscopic tool. However STXM has allowed for NEXAFS spectroscopy to be measured at a spatial resolution of 30 nm or less (the best lateral spatial resolution achieved in a STXM measurement is 10 nm [CFT&12]). NEXAFS is used to determine the electronic structure of known structures and to carry out chemical speciation of materials [FDN95]. A molecule absorbs an x-ray photon [H00] and excites a core electron into an unoccupied valence state (formally, a bound state) or into a continuum state which is above the Fermi energy (E_f) [S92]. The transition probability is governed by Fermi's "Golden Rule" [S92, RA00, SRA&95] where the dipole approximation has been applied [S92, SRA&95],

$$P_{if} = \frac{2\pi}{\hbar} |\langle f | \mathbf{e} \cdot \mathbf{r} | i \rangle|^2 \quad (1-1)$$

the photoabsorption cross-section, σ is the probability of absorption normalized by the photon flux and is given by [S92],

$$\sigma = \frac{4\pi^2 e^2}{m^2 c \omega} |\langle f | \mathbf{e} \cdot \mathbf{r} | i \rangle|^2 \rho_F(E) \quad (1-2)$$

where $\rho_F(E)$ represents the final density of states [S92]. Unlike an isolated atom, where there are no neighbours, photoelectrons in the valence shell of molecular materials feel the effects of bonding and neighbouring atomic potentials and are thus highly sensitive to the local environment of the core excited atom. The spectral features can be understood in terms of scattering of the photoelectric wave with its surrounding [RA00]. This is reflected in the cross-section, which is highly dependent on the interaction and position of surrounding atoms. When the kinetic energy of the photoelectron is small, the scattering is more prominent and the likelihood of multiple-scattering events is far more likely, whereas if the photoelectron has a large kinetic energy then only weak scattering occurs [RA00, SRA&95]. This multiple scattering regime is the NEXAFS region. It is highly sensitive to local potentials which allow chemical speciation and oxidation state determination.

1.3.2 Spin Selective X-ray Absorption: XMCD

Absorption of circularly polarized x-rays can cause spin selective transitions to occur and thus can be used to probe both the electronic and magnetic structure of a material. Production of circularly polarized light is possible with both bend magnet and Elliptically Polarizing Undulator (EPU) synchrotron sources. EPUs offer increased flux and highly pure polarized light (can be circular, horizontal or elliptical). Undulators allow for an increase in flux by emitting radiation within a narrow energy bandwidth [BDH&01]. Furthermore, EPUs can produce circular,

linear or mixed polarization by guiding the synchrotron electrons into specific trajectories. STXMs on EPU based beamlines have the added capability of being able to form images by focusing circularly polarized x-ray beam to 30 nm or smaller [CFT&12] depending on the optics [JWF&00]. Thus in principle STXM-XMCD can probe nanoscopic magnetism.

1.3.2 Theory of XMCD

The absorption cross section of an x-ray absorption process is given by equation (1-2) [S92]. The electron position operator, \mathbf{r} is the vector sum of the three Cartesian coordinates [SS06],

$$\mathbf{r} = x\mathbf{e}_x + y\mathbf{e}_y + z\mathbf{e}_z \quad (1-3)$$

where \mathbf{e}_x , \mathbf{e}_y , \mathbf{e}_z are unit vectors describing the three-dimensional Cartesian plane. Circularly polarized x-rays propagate in the z direction (wave vector, \mathbf{k} aligned), such that the unit electric field polarization is described by [SS06],

$$\mathbf{e}_z^\pm = \mp \frac{1}{\sqrt{2}}(\mathbf{e}_x \pm i\mathbf{e}_y) \quad (1-4)$$

where the electric field is propagating either in a right-handed or left-handed fashion in the x-y plane. The unit angular momentum is given as $\pm\hbar$ respectively and point along the z-axis [SS06].

The wavefunctions of the target are composed of radial, R ; spin, m_s and angular, l , m_l terms and can be separated giving the dipole operator for a z-propagating circularly polarized light such that the total transition matrix element is given by [SS06],

$$\langle f | P_z^\pm | i \rangle = \delta(m'_s, m_s) \langle R_{n', l \pm 1}(r) | \mathbf{r} | R_{n, l} \rangle \sum_{m_l', m_l} A \langle l \pm 1, m_l' | C_{\pm 1}^{(1)} | l, m_l \rangle \quad (1-5)$$

Where spin conservation is given by the Kronecker delta. The non-zero angular momentum terms for circular polarized light are given by the selection rules $\Delta l = \pm 1$ and $\Delta m_l = \pm 1$ for a photon with angular momentum of $\pm \hbar$ respectively [SS06].

However equation (1-5) only couples the circularly polarized photon with the orbital angular momentum, and thus the addition of spin-orbit coupling, which is strong in 3d metals, is necessary for coupling of the angular momentum of circularly polarized light with the spin moments associated with the material.

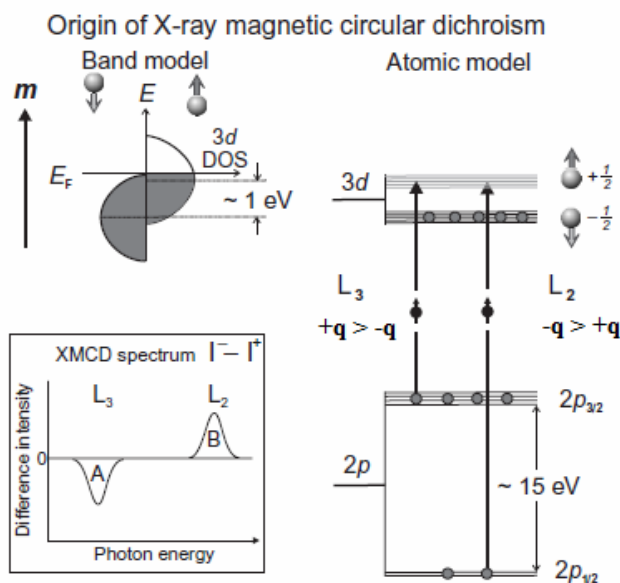


Figure 1-7 – The two-step model of the XMCD effect where photoelectrons from spin-orbit split core states are excited into the exchange split 3d orbitals. (Adapted from [SS06])

A simple two-step model of the XMCD effect is described by figure 1-7.

First, x-ray absorption of the photon with angular momentum $\pm\hbar$ imparts its angular momentum on the photoelectron excited from the 2p spin-orbit level [SS06]. The angular momentum is conserved during the photoabsorption process and is coupled to the spin given the spin-orbit coupled 2p state. This allows for preferential absorption of the $+\hbar$ photon from the $2p_{3/2}$ (L+S) orbitals and $-\hbar$ from the $2p_{1/2}$ (L-S) orbitals. The normalized XMCD signal is defined as [SS06, FDG&05],

$$XMCD = \Delta I = \frac{I^{\uparrow\downarrow} - I^{\uparrow\uparrow}}{I^{\uparrow\downarrow} + I^{\uparrow\uparrow}} \quad (1-6)$$

where the parallel and antiparallel arrows represent the relative orientation of the target's magnetic moment and the spin-orbit angular momentum of the photon.

The XMCD signal is the difference between the anti-parallel and parallel co-alignments. Since the photoabsorption process is a probe of the empty orbitals of a particular spin due to the asymmetric filling of the spin orbitals in the ground state, the XMCD signal is related to the magnitude of the ground state magnetization given that XAS is density of state dependent (see equation (1-2)). Furthermore, the ground state magnetization can be quantitatively determined by extending charge sum rules to spin-dependent photoabsorption by a net magnetized sample [SS06]. These rules have been derived (by others) and are summarized in equation (1-7) [SS06].

$$\begin{aligned}\langle L_z \rangle &= \frac{I(L_3) + I(L_2)}{L_{32}} 2N_h \\ \langle SE_z \rangle &= \frac{XMCD(L_3) - 2XMCD(L_2)}{L_{32}} \frac{3}{2} N_h\end{aligned}\quad (1-7)$$

Where L_z and SE_z are the angular orbital moment and the effective spin moment of the system respectively. $I(L_3)$ and $I(L_2)$ are the integrated intensities over the L_3 and L_2 edges.

1.3.3 – XMCD of Magnetite and Biogenic Magnetite at the Fe $L_{2,3}$ edge

XAS and XMCD of the $L_{2,3}$ edges of d-metals are powerful probes of their local electronic and magnetic structure. Firstly, the $2p \rightarrow 3d$ transition has long core-hole lifetimes thus the electronic multiplet structure is sharp and allows for highly

detailed analysis. Secondly, the L_2 and L_3 edges are well separated such that there is no overlap. Lastly, the $2p \rightarrow 3d$ transition allows core photoelectrons to probe the electronic and magnetic structure of the d-band which is the majority spin imbalanced band [VT91]. By probing this band using the XMCD effect, a large amount of information can be obtained about the electronic and magnetic ordering of the system.

The XMCD of synthetic [GGL&06, CSA&08, PBG&08, GLG&07, KSD&97] and biogenic [CSA&08, CGP&06, CPL&07, CPP&08, CTV&09, SWH&07, SWT&08, TCC&09] magnetite has been measured many times (see table 1.2 in [LHO10] for summary and discussion of XMCD studies of biogenic magnetite). Goering *et al* [GGL&06] performed XMCD measurements with total electron yield (TEY) detection on a magnetite thin film at the BESSY II synchrotron with an applied field of 10 kOe with the goal to accurately and quantitatively apply the sum rules analysis to the XMCD spectrum. Goering *et al.* [GGL&06] found that the XMCD spectrum of magnetite consists of a characteristic down-up-down pattern at the Fe L_3 edge and a different pattern at the L_2 edge. This general shape is consistent with other previously obtained results [GLG&07, CSA&08] which may have been questioned due to surface oxidation effects that are amplified in TEY measurements since it is a surface sensitive technique. In the Goering study [GGL&06], the crystal was cleaved in vacuum to expose a face that was not in contact with air so the surface oxidation effect was minimized. Furthermore, other effects leading to non-quantitative results were carefully monitored. Although

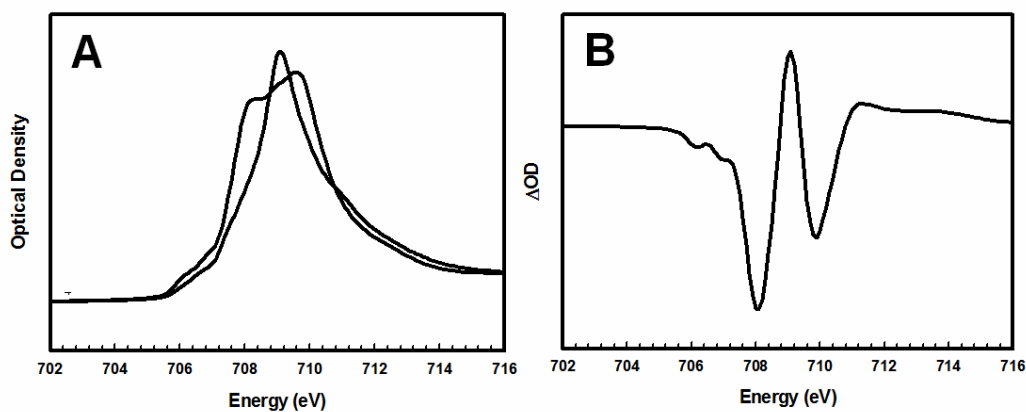


Figure 1-8 - a) Fe L₃ polarized spectra of magnetite. The antiparallel and parallel labels correspond to the vector alignment of the magnetic moment and the imparted photon moment. b) The XMCD spectrum obtained by taking the difference of the antiparallel and parallel Fe L₃ edge spectra. The Fe L₃ XMCD spectrum shows a down-up-down behaviour. Spectra provided by E. Goering ([GGL&06]).

qualitatively the XMCD looked similar to that of previous results, the sum rules analysis shows that the orbital and effective spin magnetic moments previously established were not accurate. The new moments agree well with several calculations. The average orbital moment was found to be $-0.001 \mu_B$ whereas the effective spin moment was found to be $3.9 \mu_B$ which is consistent with calculation results [GGL&06] and in agreement with the theory regarding 3d magnetism which states that magnetic ordering in 3d orbitals is near zero because of the dynamic nature of the 3d orbitals involved. However, because of the low photoelectron path length, TEY measurements may still be affected by surface oxidation from residual oxygen in the vacuum system. These and other negative effects can be better overcome in part by performing measurements in

transmission mode. Transmission mode allows for the electronic structure of the bulk to be more accurately reflected in the final spectrum even if there is some surface oxidation.

The XMCD of biogenic, particularly bacterial, magnetite has been measured by several groups. In particular, the work of Carvallo *et al.* showed that the XMCD spectra of biogenic and abiogenic magnetite nanoparticles differ slightly [CSA&08]. This difference has been attributed to the site occupancy of magnetite which appears more oxidized (Fe(III) rich) in the abiogenic samples [CSA&08]. There is evidence of this in MTB using synchrotron x-ray diffraction techniques which showed that abiogenic magnetite is much more susceptible to surface oxidation [FSA&11].

In order to understand Fe $L_{2,3}$ XAS and XMCD spectra, many groups have turned to calculations of the electronic structure and modelling of the spectra. The reported occupancy differences stated are based on ligand field multiplet calculations on magnetite [PVH&02] which showed a direct correlation of the three main L_3 XMCD peaks (down-up-down) and the three cation site occupancies. The multiplet calculations showed that the first (down) peak corresponds to the Fe(II)_{Oh} site, the second (up) peak to the Fe(III)_{Td} site, and the third (down) peak to the Fe(III)_{Oh} site [PVH&02]. In general the less oxidized species will have a shallower core-hole because of the larger shielding effects from valence electrons and thus appear at lower energy in the XAS spectrum. The Fe(III)_{Td} site is known to antiferromagnetically couple to the octahedral sites so

the XMCD spectrum should reflect that ordering [SS06]. However, multiplet broadening has been known to mix both L_3 and L_2 states and can play a role in the sum rules analysis [GGL&06]. The $L_3 - L_2$ separation is ~ 9 eV whereas the XMCD peaks from different sites are separated by only a few eV. A simple correlation between crystal site and specific features in the L_3 edge XMCD is most likely an oversimplification. Furthermore, multiplet calculation software packages utilize an atomic picture to calculate the multiplet structure. The assumption that the Fe $L_{2,3}$ edge is dominated by atomic multiplet structure is one possible interpretation of the XMCD spectrum of magnetite. However, several groups have used non-multiplet, full *ab initio* electronic structure calculations and have reproduced both the Fe $L_{2,3}$ XAS and XMCD spectra of magnetite [MSC&04, AHY03]. Furthermore, these results are, in some regards, more rigorous due to the full calculation of the electronic structure and reproducibility of several key properties of magnetite, for example the metal-insulator transitions and half-metallic behaviour. XMCD calculations have been successfully recreated using several calculation methods; however, the spectra still not completely understood.

1.4 – The Scanning Transmission X-ray Microscope and Beamlines

Scanning Transmission X-ray Microscopy (STXM) is a synchrotron based x-ray spectromicroscopy technique that combines x-ray absorption spectroscopy (XAS)

and scanning microscopy principles to yield a technique that can perform XAS thus giving chemically and magnetically sensitive information at a high spatial resolution. STXM optics is suited to the soft x-ray regime and thus is primarily used to analyze biological and polymer materials [AH08]. However, with the use of Elliptically Polarizing Undulator (EPU) based STXMs one may perform XMCD studies on magnetically sensitive transition metal L edges. Synchrotron radiation is produced by the EPU by causing acceleration to relativistic, spatially semi-coherent electron bunches. EPUs are four quadrant arrays of permanent magnets. By shifting the relative positions of the girders, EPUs guide electrons into various trajectories which determine the polarization of the synchrotron radiation. One may create circularly polarized photons by sending the incoming electron bunch into a helical motion, which then allows for a temporal rotation of the emitted electromagnetic wave. Since the electron travel at near relativistic speeds, the emitted radiation is highly collimated giving it high spatial coherence.

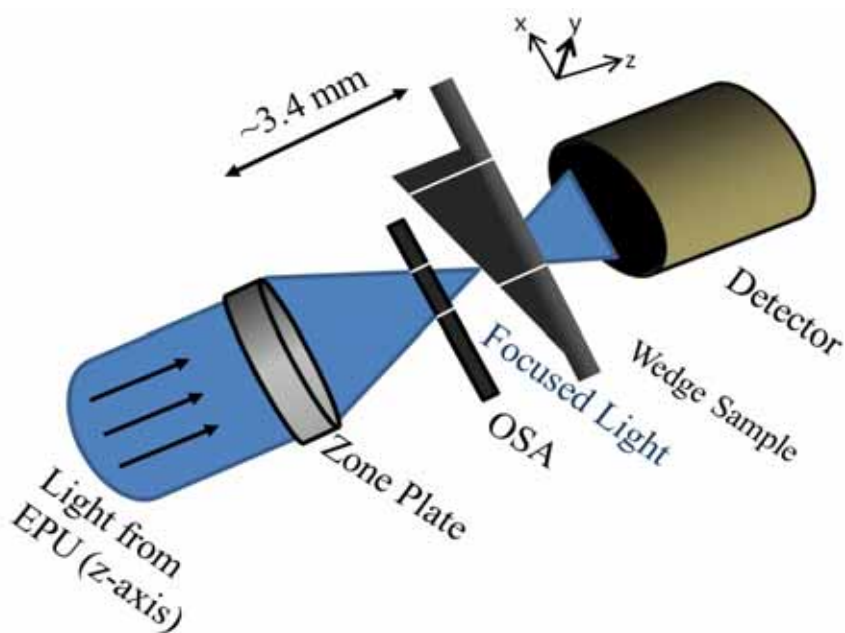


Figure 1-9 – STXM optical system setup with distances for the Fe $L_{2,3}$ edge. The distance from the Zone Plate to the Sample is 3.4 mm. The z-axis is the x-ray propagation axis, while the sample is scanned in the x-y plane.

The light is monochromated by a plane grating monochromator and passed into the STXM. The STXM uses a Fresnel Zone Plate (ZP) (circular diffraction grating) to focus the light to a point. Fresnel ZPs consist of finely positioned concentric zones with alternating opaque and transparent sections. Zones farther from the central stop have a smaller width such that the diffraction of light gives a finely focused cone of light. Only first-order diffracted light is allowed to pass through; an Order Sorting Aperture (OSA) is positioned to block zero-order and higher order diffracted light from passing onto the sample. The sample is placed at the focal spot of the diffracted first-order x-rays and scanned using a piezo stage. Figure 1-10 shows the STXM mechanical set-up. The sample is scanned in

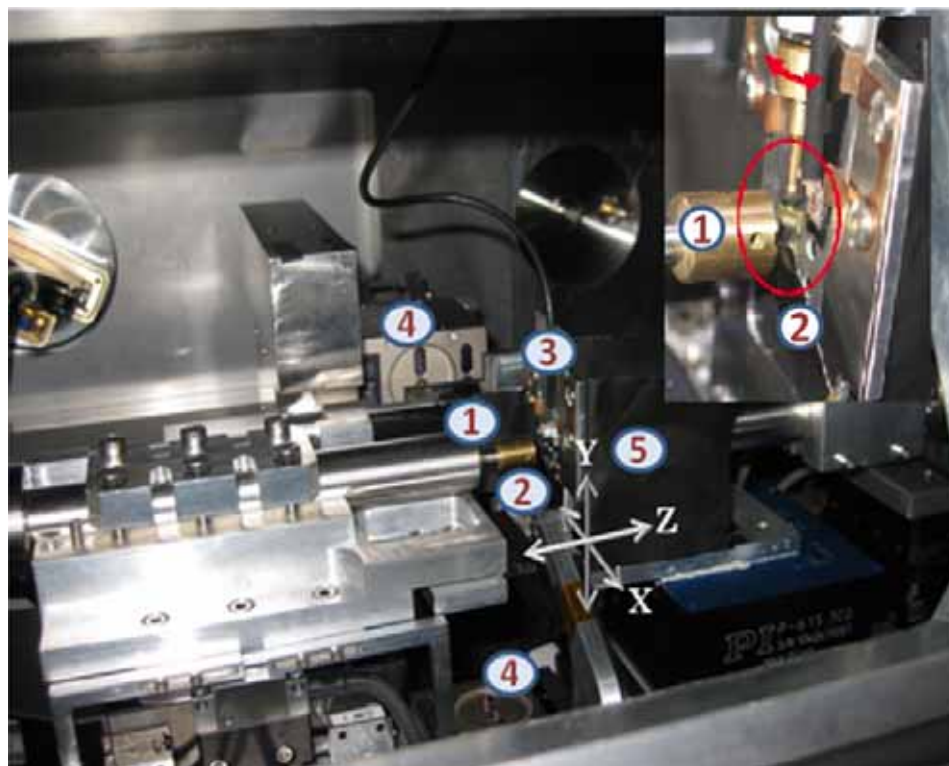


Figure 1-10 - The Scanning Transmission X-ray Microscope Beamline at the Canadian Light Source shows the basic components of the microscope: 1. the zone plate, 2. Order Sorting Aperture, 3. sample stage, 4. laser interferometer system and 5. the detector. Inset shows a close-up of 1 and 2 with an XMCD tomo-rotator sample to show the constraint of the setup.

the x-y plane, the x-ray propagates in the z-axis which is also the axis along which the sample and zone plate are moved to obtain optimal focus. Some of the x-rays are absorbed by the sample, the transmitted soft x-rays are converted to visible light by a very thin phosphor. The visible photons are detected by a photomultiplier tube detector operating in single event detection mode maximum count rate of 20 MHz.

When operated in the diffraction limit the STXM resolution is determined by the width of the outermost zone of the zone plate. The relationship is given by equation (1-8)

$$\Delta r = 1.22 \cdot \delta_{rN} \quad (1-8)$$

where Δr is the spatial resolution and δ_{rN} is the width of the outermost zone of the zone plate [A07]. For a typical 25 nm outer zone ZP the size of the focal spot is 31 nm. The focal length (f) is described by equation (1-9)

$$f = D \cdot \frac{\delta_{rN}}{\lambda} \quad (1-9)$$

in which D is the diameter of the outermost zone and λ is the wavelength of the incoming light [A07]. As the photon energy is changed, the focal length changes and the ZP is moved to keep the sample in focus.

The focal length at the Fe $L_{2,3}$ edge (710 eV) is 3.4 mm (ZP-sample separation). This introduces large constraints on STXM experiments, in particular XMCD experiments where the sample is projected along the z-axis. For a 30° wedge sample typically used for a MTB XMCD experiment, the wedge extends out ~2.5 mm [L10] which makes putting the sample into focus a challenge as the sample can very easily bump into the OSA. Care is needed in the experimental design and execution.

1.5 – Goals of this thesis

This thesis was started at the conclusion of Karen Lam's work on MTB using STXM-XMCD [L10] where she showed that the STXM was capable of obtaining the XMCD spectrum of individual magnetosomes. Using Karen's achievements as a launch point for this thesis, some goals were identified:

- To improve the quality of the STXM-XMCD data
 - By increasing the statistics in the XMCD
 - By reducing noise in the imaging
 - To quantitatively determine the magnetism of individual magnetosome chains.

- To use STXM-XMCD as an analytical technique to help understand biomineralization of magnetite by magnetotactic bacteria
 - By designing experiments to allow for measuring the magnetism of magnetosomes in a single cell for multiple cells.
 - By comparing results for genetically modified cells to those for wild type cells to understand the implication on magnetosome formation and their magnetism.

The above were the central goals and results of this thesis and are discussed in chapters 3 and 4 respectively. Other goals that were also identified at the start of

the project are listed below. These represent incomplete and ongoing projects.

They are discussed in chapter 5.

- To chemically and magnetically differentiate magnetite and greigite production in a single magnetosome chain of BW-1
 - Perform STXM-XMCD measurements on BW-1
 - Possibly link to biochemistry of the cell

- To obtain independent measurements of the XAS/XMCD of magnetite and greigite
 - Synthesize magnetite and greigite thin-films
 - Use *in situ* magnetization of sample to perform STXM-XMCD measurements.

- To acquire a better understanding of the XAS and XMCD of magnetite and greigite through electronic structure and band structure calculations.

Chapter 2

Experimental

This chapter describes the techniques and methods used for culturing and preparing magnetotactic bacteria samples, sample mounting, performing STXM measurement and STXM data analysis. Furthermore the STXM methodology is summarized.

2.1 – Magnetotactic Bacteria Samples

2.1.1 – Preparation of Magnetotactic Bacteria Sample

All samples were supplied by collaborators, primarily Professor Dennis Bazylinski and his post-doctoral fellow, Christopher Lefèvre from University of Las Vegas, Nevada. Some samples were provided Professor Ulysses Lins (Universidade Federal do Rio de Janeiro) and Professor Arash Komeili and his post-doctoral fellow Ertan Ozymak (University of California, Berkeley). MV-1 bacteria samples, provided by Dennis Bazylinski *were* cultured using methods previously described [DB99]. Other strains were cultured or obtained from the environment. Both cultured and environmental samples may be concentrated using magnetic separation techniques such as the “race-track” method [WTP87].

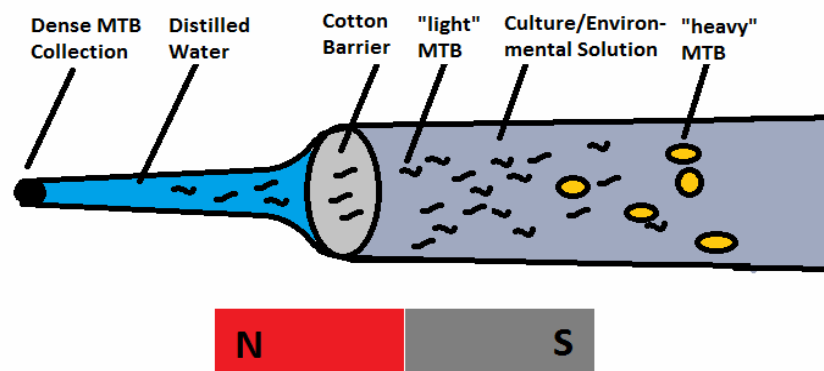


Figure 2-1 – A schematic of the race-track separation method.

As outlined in figure 2-1, the “race-track” method involves separation and concentration of magnetically sensitive bacteria by using a long pipette as a track and simple bar magnets along the long axis such that bacteria move towards a closed end of the pipette. Distilled water is placed within the tip and filled to meet a cotton ball placed at the bottle-neck. The cotton ball acts as a natural barrier for free flow of material into the stem. The pipette stem is then filled with culture medium or environmental solution. Once placed in a magnetic field, one may direct the MTB to the distilled water solution thereby separating it from the culture solution which contains salts and other material which can later result in poor samples. Environmental samples have the added difficulty that other, unwanted organisms may be present and have the ability to move past the filter. Furthermore environmental samples may actually contain other species of magnetically sensitive bacteria other than those of interest in the concentrated sample. However, with care, it is possible to separate multiple magnetically sensitive bacteria by their magnetization-to-mass ratio which creates latency in the arrival time of different MTB. Once a sufficient amount of cells are present at the end of the pipette tip, the tip is broken off and the concentrated solution is transferred either to a cover slip for “hanging-drop” visual analysis or onto a TEM grid for TEM and/or STXM measurements. One may further increase the cell density by centrifuging a culture solution before sample deposition. In this study, typical centrifugation rates were kept to <4000 rpm with centrifugation times kept to under 5 minutes to avoid cell lysis. Once a visible pellet collects at the bottom

of the centrifuge tube, the supernatant is discarded and the pellet may be resolubilized in distilled, deionized water and then deposited onto a TEM grid or window.

Grid samples are prepared by placing a drop directly on the grid which is typically copper with a thin formvar coating, or silicon nitride windows. The drop is allowed to stand for 5-10 minutes as the suspended material settles onto the grid. Further settling of MTB may be induced by placing the grid on a magnet with the appropriate magnetic orientation; however it is difficult to maintain the induced cell orientation due to the capillary action of the wicking procedure used to dry the cell. The water drop is wicked away with pre-cut filter strips and the grid is allowed to stand and air dry. If the sample being prepared is air-sensitive, as is the case for greigite producing MTB, the sample should be prepared and stored in an inert environment (Ar or N₂ gas is typically used) until mounting in the TEM or STXM in order to reduce exposure to air. Depending on the composition of the sample, a drop of deionized water may be placed on the dried sample grid and wicked away as described above in order to remove any excess salts that may be present in the culture or environmental solution. In many cases, grids or windows are washed after to remove excess salts.

2.1.2 – Characteristics of Magnetotactic Bacteria used in these studies

Table 2-1 summarizes the MTB for which STXM measurements have been performed during this thesis. Not all MTB for which measurements were performed are discussed in this thesis.

Strain	Shape	Size	Magnetosomes	Source	Provider	Studies
<i>Candidatus Magnetovibrio Blakemorei</i> , MV-1	Vibrio	1-3mm	Magnetite, 40-90nm, single chain	Culture, UNLV	DAB	Biochemical studies, first studies on the XMCD of individual magnetosomes, Anomalous magnetic orientation of magnetosome sub-chains
Magnetotactic Multicellular Prokaryote, MMP	Multi-cellular	5-10mm	Greigite, 25-50nm, multi-chained	Rio de Janeiro	UL	Coherent magnetism of multiple chains, XMCD of greigite
<i>Desulfamplus magnetomorris</i> , BW-1	Rod	5-8mm	Greigite, 25-50nm, multi-chained.	Death Valley	DAB	XMCD of greigite, comparative analysis of magnetite, greigite and bi-phase producing BW-1
BW-1			Magnetite, 30-75nm, multi-chained	Utah	DAB	XMCD of magnetite, comparative analysis of magnetite, greigite and bi-phase producing BW-1
BW-1			Magnetite and Greigite, 25-75nm, multi-chained	Culture, UNLV	DAB	Distinguishing greigite and magnetite magnetosomes, comparative analysis with single phase producing BW-1
<i>Magnetosprillum Magneticum</i> , AMB-1	Spirilla	1-4mm	Magnetite, 40-90nm, single chain	Culture, UC Berkeley	AK	Comparison of magnetism with respect to mutant
<i>Magnetosprillum Magneticum</i> , AMB-1 DK Mutant	Spirilla	1-4mm	Magnetite, 40-90nm, single chain	Culture, UC Berkeley	AK	Comparison of magnetism with respect to wild type

2.2 – Transmission Electron Microscopy of MTB

2.2.1 – Sample preparation of MV-1 thin sections

Thin sections were prepared by Marcia Reid at the Electron Microscopy facility in the Faculty of Health Sciences at McMaster University using the following procedure. The bacterial culture sample was centrifuged at low speeds (<4000 rpm) to form a pellet and the growth medium pipetted off. The pellet was fixed for 2 hours in 2% glutaraldehyde in 0.1M sodium cacodylate buffer pH 7.4. The sample was rinsed 2X in buffer solution, then post-fixed in 1% osmium tetroxide in 0.1M sodium cacodylate buffer for 1 hour. The sample was dehydrated through a graded ethanol series (50%, 70%, 70%, 95%, 95%, 100%, 100%) and then further dehydrated in two changes of propylene oxide (PO). Infiltration with Spurr's resin was done in a series (2:1 PO:Spurr's, 1:1 PO:Spurr's, 1:2 PO:Spurr's, 100% Spurr's, 100% Spurr's, 100% Spurr's) with rotation of the sample between solution changes. This step displaces much of the organic matter with fixative allowing for ease of thin-sectioning while preserving the shape of the cellular structures. The pelleted sample was transferred to embedding moulds which were then filled with fresh 100% Spurr's resin and polymerized overnight in a 60C oven. Thin sections were cut on a Leica UCT Ultramicrotome and picked up from a water surface. In some cases TEM grids post-stained with uranyl acetate and Reynold's lead citrate stains to better visualize the magnetosome membrane.

2.2.2 – *Transmission Electron Microscopy (TEM) of MTB*

TEM was used as a complimentary tool to STXM-XMCD. Due to the physical constraints of the STXM-XMCD experiment (see section 1.4) and the small size of cells (~1-5 μm cell length depending on the species) and magnetosomes (25-120 nm) TEM proves a useful tool for high-resolution imaging. TEM was also useful for navigation such that samples areas rich in MTB and even cells with certain characteristics may be located and viewed more quickly using STXM. MTB samples were viewed using a JEOL 1200EX TEMSCAN at the Faculty of Health Sciences, McMaster University.

2.3 – **Sample mounting**

The samples were mounted on standard flat plates (see fig 2.3a) for C 1s edge measurements where the focal lengths are small so that rotated samples cannot be viewed. Double-sided tape was cut into strips using a scalpel and two strips of tape were put down on the edges near the sample hole of choice at opposite sides of the hole in order to keep the grid stable. The grid was carefully placed on the sample such that the grid square orientation was pointing directly in the x and y axes of the STXM to aid in navigation and to allow maximum access to the area between the grid boundaries with minimum scan areas. When grids are oriented diagonally, it is often necessary to include areas of grid box in the image scan which is time efficient given that STXM is a serial scan technique.

STXM-XMCD experiments require a rotation of the sample about the y-axis, such that the sample protrudes into the z-axis. Rotations were largely limited to 30° out-of-plane although they were occasionally as high as 45° . This allows for the horizontally oriented magnetic moments of the horizontally oriented magnetosome chains to project onto the XMCD sensitive z-axis. At a tilt angle of 30° there is a 50% projection of the magnetization onto the z-axis (figure 2-2).

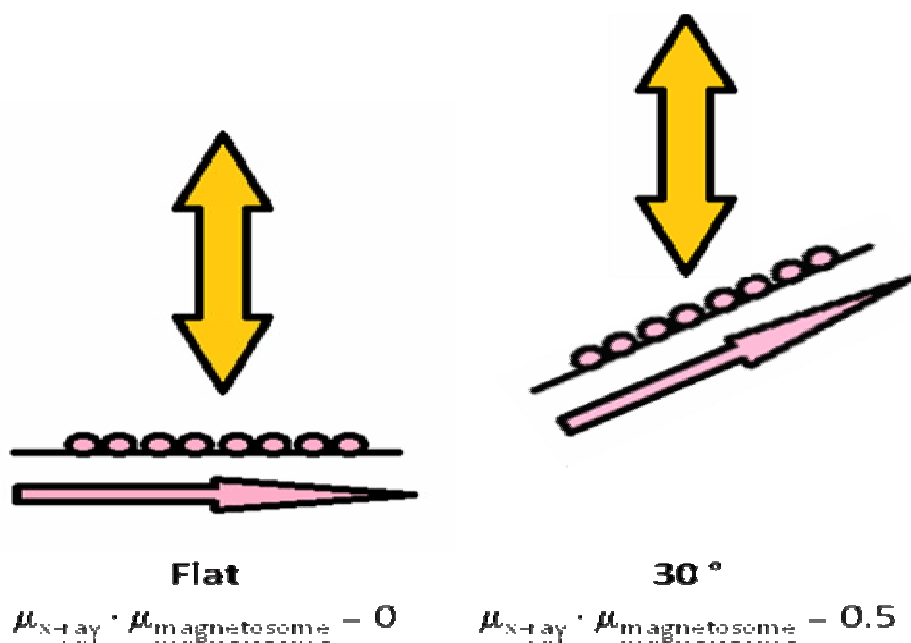


Figure 2-2 - XMCD experimental setup showing the need for 30° sample tilt which allows for a projection of horizontally oriented magnetic moments into the x-ray moment axis which allows for the XMCD effect to appear in polarization experiments.

Sample rotation has been achieved by several sample mounting variations. The three XMCD sample mounts use in this work are the cut-back plate, wedge plate and the tomo-rotator stub plate.

2.3.1 – Cut-back and Wedge Plates

A fixed sample rotation was achieved by using a cut-back plate (Fig. 2-3b). A cut-back plate cuts away the standard STXM sample plate (Fig 2-3a) from all but column and uses one hole (typically one of the bottom row of sample holes is used to accommodate all STXMs and their sampling restrictions). A strip of the sample plate containing the hole may then be projected forward and rotated or a slit is cut into the top part of the wedge such that one may tilt the sample forward from the sample plate plane. The second method allows for the sample to be projected from the sample plane giving a better estimation of the zone plate-OSA-sample-detector geometry and thus avoid collision with the OSA or ZP. Also useful is that the tilt may be changed to different angles either to increase the XMCD sensitivity or to accommodate the spatial restrictions of the sample environment in the STXM. However the exact tilt angle in the cut-back method is difficult to measure and it is difficult to keep the tilt about the x-axis to zero such that there is only a projection of the y-axis onto z-axis. This may lead to quantitatively inaccurate results of the magnitude of XMCD as well as interference between the sample and the OSA or the detector.

The wedge plate (shown in fig 2.3c) is a special sample holder that holds a fixed

30° incline by an aluminium wedge glued to a standard plate. The wedge tilts the sample by 30° and allows for the projection onto the XMCD sensitive z-axis. The wedge protrudes ~2.5mm in the z-direction. In a typical experiment with a 25-nm

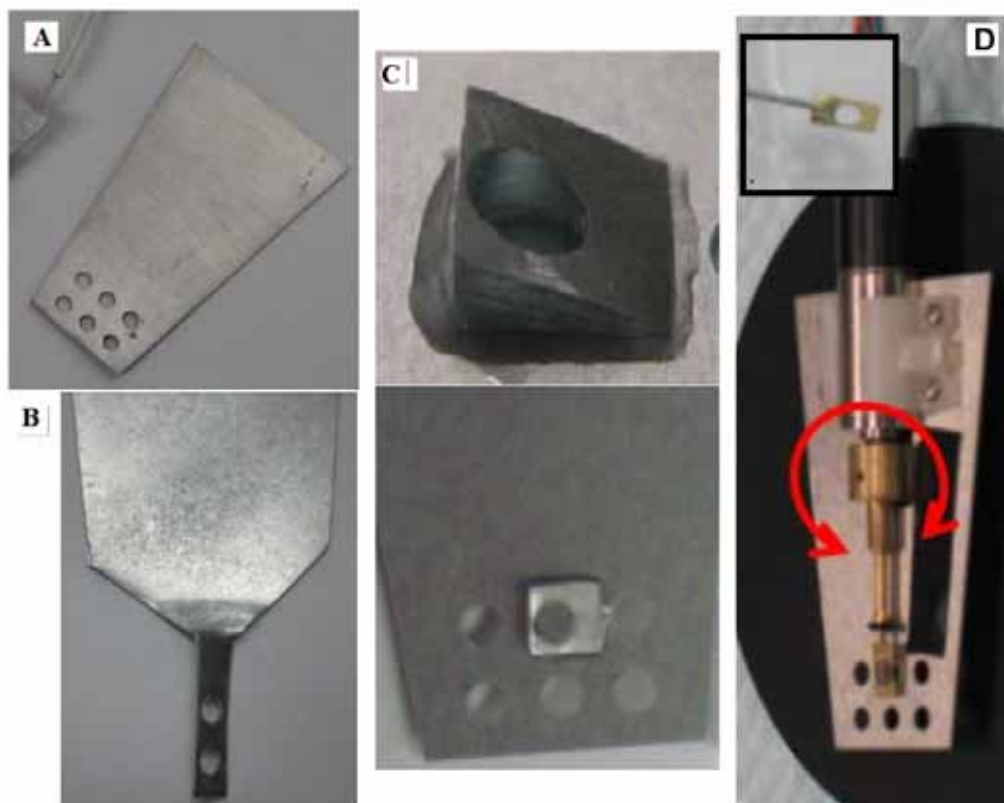


Figure 2-3 – a) Shows the standard flat sample plate holder. Typically the bottom row of holes are used to accommodate the restrictions of all STXMs b) Twisted plate. c) A wedge plate. The wedge-plate allows for a projection of magnetism in the x-axis into the magnetically sensitive z-axis. The wedge is an aluminium block glued to a standard sample plate d) The tomo-rotator and pin (inset) are used for *in situ* rotation of the sample, typically a grid strip is mounted on to the pin and is then inserted into a split collet attached to the motor. The sample rotation is then controlled on-screen by the STXM computer.

zone plate the focal distance at the Fe $L_{2,3}$ edge is large enough that the whole sample grid is navigable. However, where possible, imaging is typically performed on the most extended portions of the wedge so as to reduce the chances of touching the OSA during sample scanning.

2.3.2 – Tomo-rotator Stub

The tomography rotator stub (Fig 2.3d) is a motorized rotator that has the capability to rotate *in situ*. It allows full 360° rotation in either the clockwise or counter-clockwise direction. The rotator plate is a special plate where the rotation motor has been mounted into a cut-away in a regular sample plate. A 1 mm pin with a flattened section is used to mount either a whole grid or a single ladder (strip) of a grid sample onto the stub using either nail polish or epoxy as an adhesive. The stub is then held by a split collet and o-ring ‘keeper’ onto the shaft of the motor. The added benefit of *in situ* rotation is that it allows for measurement and location of an ideal MTB in the flat sample geometry where larger areas can be viewed because in principle the whole sample can be within the focal plane. In contrast with fixed, rotated samples, one must re-focus the sample every $\sim 15 \mu\text{m}$ when displacing horizontally. Furthermore the tomo-rotator has the ability to move quickly from biochemical measurements at the S 2p, Ca 2p, C 1s, N 1s, and O 1s edges where, the focal length is small and rotated samples may not be viewed, to the magnetically sensitive Fe 2p edge where a rotation of the sample is necessary in order to detect the XMCD signal. Use of the tomo-rotator allows for less time of sample mounting and unmounting, decreases

the risk of damaging the sample through handling, and allows for more comprehensive studies of MTB.

2.4 – Measurements and Analysis of MTB

Scanning Transmission X-ray Microscopes [AH08] at the Canadian Light Source (CLS) 10 ID-1 Spectromicroscopy beamline and the Advanced Light Source (ALS) 11.0.2 STXM Molecular Environmental Science beamline were used to

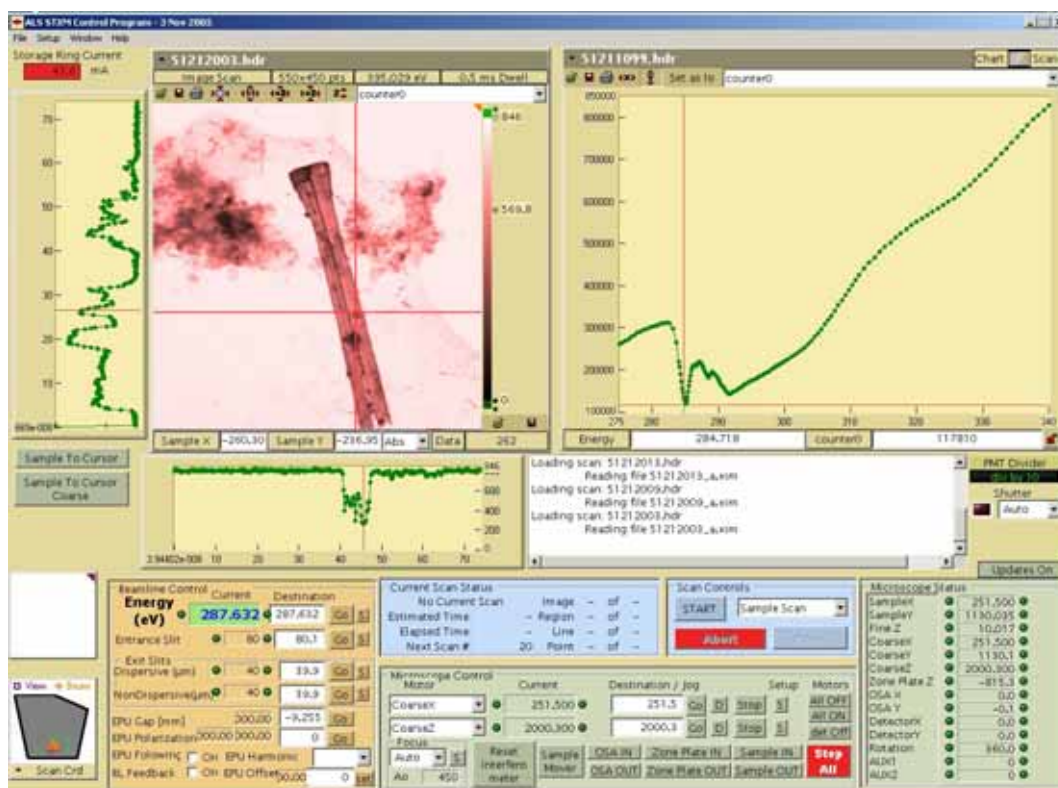


Figure 2-4 – The STXM_control front end GUI. The GUI controls the sample, ZP, OSA, detector positions as well as the beamline polarization, energy and optics. Furthermore it is used to calibrate the STXM for optimal use (through focusing and alignment of STXM optics) as well as for setting up experimental measurements.

make measurements of the MTB samples. These microscopes have many common features that make sample preparation largely the same. STXM uses several modes of data collection, including the “stack mode” which generates stacks of images as the region of interest is scanned serially with successive energies through an x-ray absorption edge of interest. A single image at a single energy may be performed in “imaging mode”.

Imaging and Stack modes may be measured using “line at a time” or “point by point” scanning of the sample. In general, “point by point” scans afford better performance due to the higher stability and reproducibility of the stage positioning. The drawback to “point by point” scanning is the longer data acquisition time required relative to the analogous “line at a time” mode. More information is available in the STXM user manual [ST03] which details the STXM_control software and data collection modes.

A Stack is written as a series of simple binary image for each energy and is analyzed using aXis2000 software (section 2.5). A stack contains 3-dimensions of data, two spatial dimensions and an energy dimension. This results in a spectrum at each pixel which allows for x-ray spectroscopic analysis of heterogeneous samples. For example, in an MTB sample, one can measure the Fe $L_{2,3}$ edge spectrum of each individual magnetosome. As shown in this thesis, this allows for differentiation of subtle effects (i.e. oxidation/reduction and the magnetic properties) which are reflected in the spectroscopy.

2.4.1 – STXM Measurements of MTB

The relevant XAS edges of MTB include the Fe L_{2,3} edge (~ 695-745 eV), the oxygen edge (O 1s ~ 510-560 eV) both of which are sensitive to the properties of magnetosomes. The Ca 2p (~340-360 eV), C 1s (~270-320 eV), N 1s (~395-420 eV) and S 2p (~185-210 eV) and the O 1s edge probe the biochemical components of the cell (see Chapter 3, figure 8-9). The S 2p edge is also important for samples containing greigite magnetosomes.

Due to the small size of magnetosomes, which are typically in the 40-75 nm range and the limited spatial resolution of the STXM used (~30 nm) it is a challenge to measure the Fe 2p spectra of individual magnetosomes with high statistical quality. Acquisition parameters that control the quality include the flux, the beam stability, dwell times, pixel sizes and the scan mode chosen. Typical dwell times of 5-12 ms per pixel are used. Furthermore, image oversampling is used to increase the imaging quality. Typical pixel sizes used for imaging magnetosomes is 8-15 nm. Image quality is also increased by using “point by point” mode which has higher positional accuracy. However, an increase in the quality of the images is coupled with an increase in data collection time. A stack with 10 nm pixel size, 8 ms dwell in “point by point” mode may take from 4-8 hours depending on the image size and whether XMCD is being performed. XMCD increases the time by ~120% because of (1) recording of images at two polarizations (2) wait times introduced in order to change the polarization at each energy. Therefore the image size is typically restricted to “only the magnetosomes” with any accompanied

“dead space” used for determining the I_0 and to account for sample drift during the experiment.

The quasi-concurrent polarization data collection scheme for XMCD stack measurements is necessary in order to accurately account for carbon buildup during the experiment [KLB&12]. Carbon buildup occurs during the experiment due to irradiation of the sample which also causes irradiation of the organic matter present in the STXM tank. Radiation decomposed organic material is deposited onto the irradiated sample area and affects the optical density measurements even at the Fe $L_{2,3}$ edge, 400 eV above the C1s edge. By selecting an I_0 region which has experienced similar carbon buildup it is possible to normalize for it. However, if XMCD polarization stacks are taken successively, first one polarization and then the next, the I_0 measurements can be skewed by non-identical carbon buildup profiles which will adversely affect the data analysis.

C 1s edge spectromicroscopy of MTB has no need for polarization dependent magnetic measurements (however other dichroic responses may be present in organic material, i.e. linear dichroism). STXM can map the biochemical macromolecules in a sample including proteins, carbohydrates and lipids. Stacks at the C 1s edge (as well as other biologically relevant edges) may allow mapping of the cell membrane, extracellular polymeric substances or biofilm (EPS) and the cytoplasm of MTB. Furthermore, polyhydrobutyrate (PHB) or lipid granules may be separated if present within the cell, as in BW-1 and some cells of MV-1. Dwell

times are typically 1 ms and pixel sizes range from 20-75 nm for C1s stack measurements. The data collection time is typically 30-60 minutes.

2.4.2 – Fe 2p - XMCD measurements of magnetosomes

XMCD measurements were performed using samples mounted with one of the three methods described in sections 2.3.1-2. XMCD measurements require that the magnetic moment of the sample is horizontally oriented or has a portion of the moment in the x-axis so that it is projected onto the XMCD sensitive z-axis [L10]. XMCD measurements of magnetite require both left and right circularly polarized light and can be performed at the Fe L_{2,3} edge. Typically only Fe L₃ edge (700-720 eV) measurements were performed in order to shorten acquisition time.

2.5 – Data Analysis using aXis2000

aXis 2000 is a spectromicroscopy analysis software built in the IDL language. The program was developed by Chris Jacobsen, Carl Zimba, Peter Hitchcock, Adam Hitchcock and others and is currently maintained by Adam Hitchcock. It is free for non-commercial use and it is available by download from <http://unicorn.mcmaster.ca/aXis2000.html>.

2.5.1 – Edge Chemical and XMCD Maps

Chemical maps are created using an on/off data acquisition scheme where one image is taken at the energy of interest and second image off the energy of

interest. For example, at the Fe L₃ edge, 709.4 eV corresponds to the maximum Fe L₃ absorption by of magnetite while at 700 eV below the onset of the Fe L₃ edge, the signal arises from non-iron components that have residual S2p, C1s, N1s or O1s absorption. The difference between on-resonance and pre-edge images subtracts the pre-edge signal yielding an image of the iron components.

Furthermore one may quantitatively determine the amount of a given component present if a normalized reference spectrum is available. However with the presence of multiple chemical components it is better to use more sophisticated signal processing such as fitting by Singular Value Decomposition (SVD) or by Principal Components Analysis (PCA) or related Multi-Variate Statistical Analyses (MSA) [KLB&12, LJG&05]. Chemical maps can be performed with a multi-energy scheme to add further chemical and speciation information.

For XMCD mapping, the goal is to extract the magnetic information contained in the XMCD spectrum in a more time-efficient way than a full XMCD stack.

Instead of an on/off peak energy scheme, a left/right polarization scheme at a single energy is used. Since the optical density of non-magnetic material is the same for both polarizations, a difference map automatically cancels out the non-magnetic components. Furthermore, the magnetic components will be reflected in the difference of left circular and right circular polarization images. The intensity of the XMCD map is proportional to the magnitude of the magnetic moment, which may be quantified if the magnetic material and its normalized reference XMCD spectra are known. Furthermore, the sign of the XMCD signal in an

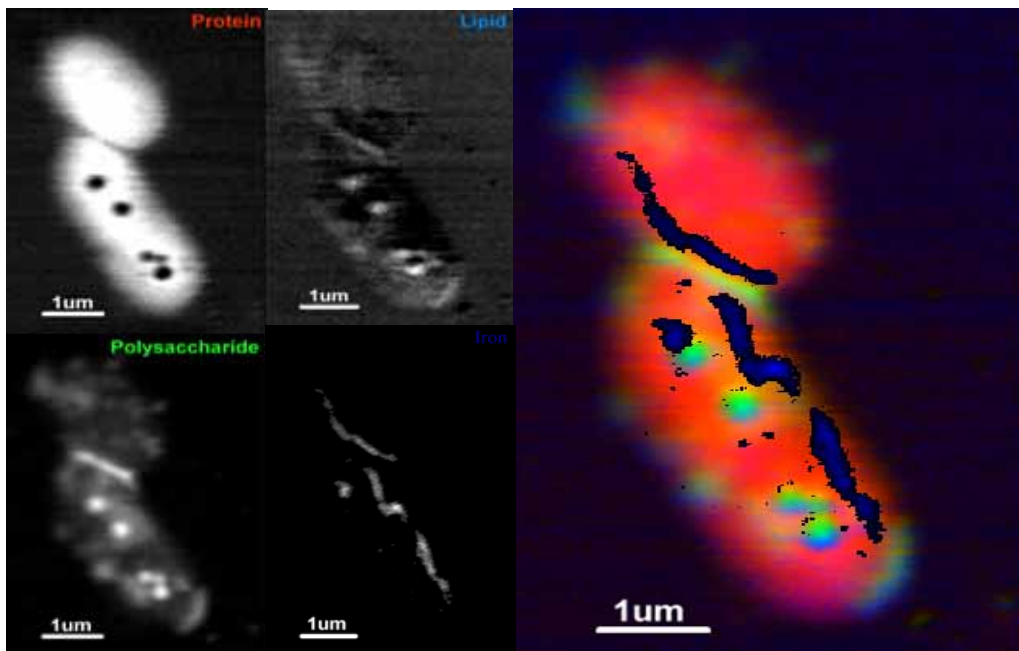


Figure 2-5 - Individual and composite component maps of two BW-1 MTB cells. Each map shows the macrobiomolecular components and magnetosomes and their segregation within the cell. The composite image is falsely coloured to enhance visualization.

XMCD map gives the projected direction of the magnetic moment. In a linearly magnetized system such as magnetosome chains, the moment can be inferred to be along the axis of the length of the chain and the XMCD map gives real space information. However, in cases where the true orientation of the magnetization is unknown, only the projected moment is known.

2.5.2 – Fe 2p and XMCD Spectra of Magnetite

A reference spectrum of magnetite at the Fe 2p edge was provided by Goering [GGL&06]. The non-magnetically sensitive spectrum is the average of the spectra for each polarization. The polarization spectra are separated into “parallel” and “anti-parallel” channels. The parallel spectra represent the spin absorption channel

where the spins of the photon angular momentum and the spin magnetic moment is aligned and the anti-parallel spectra represents when the two moments are anti-aligned. These two spectra can be collected either by using statically magnetized magnetite and changing the circular polarization or by changing the magnetization and keeping the x-ray circular polarization constant. In the case of MTB samples where we want to probe the remnant magnetization, the changing polarization method is used.

The Fe L_2 XMCD spectrum of magnetite has useful additional information as it is not a simple inversion of the Fe L_3 spectrum. However, the smaller overall resonance intensity at the L_2 edge as well as a smaller XMCD intensity requires higher quality data collection. For this reason, many of our studies were performed at the Fe L_3 edge exclusively. Issues still occur with respect to spectral normalization. Typically one may fit the pre-edge and the post-edge to atomic absorption profiles. However, with iron oxides, due to large amount of mixing of states, the fitting procedure can be quantitatively inaccurate. Furthermore, since this study has largely looked at the Fe L_3 edge which is very close in energy to the Fe L_2 edge it is difficult to determine the proper far-continuum intensity and thus the sample thickness. Also it may be inaccurate to fit the post-edge identically for the parallel and anti-parallel Fe L_3 spectra of magnetite due to the presence of spin-dependent transitions in between the Fe L_2 and L_3 edges.

2.5.3 – Stack Analysis of XMCD Stacks

All analysis was performed using the axis 2000 program. Before the actual

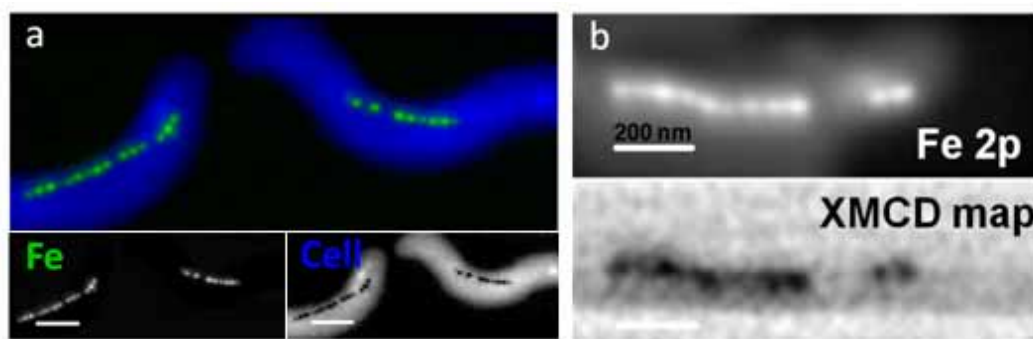


Figure 2-6 - a) Chemical map showing the cell and the magnetosomes of a MV-1 MTB cell using Fe 2p stack map data collection b) XMCD map of MV-1 MTB magnetosomes showing their orientation and intensity.

analysis may be performed the stack must be deglitched, aligned and converted into optical density. Deglitching is typically performed on some images that may have been corrupted because of a fault in the STXM_control software, instability in the storage ring, beamline or have experienced one or multiple zero points due to beam trips or data collection faults. Automated deglitching of zero points is available in the aXis2000 package. For other issues, images are typically deleted if they will pose problems to the analysis and are not necessary, for example if they occur in the featureless pre-edge region. For XMCD stacks it is important to ensure that the image at the same energy for each polarization is deleted such that the stack dimensions remain the same.

An alignment procedure is typically necessary before analysis of the data as there is both instrumental and sample drift that has caused movement in a stack. Since data collection of XMCD stacks occurs quasi-concurrently, such that images are collected for each polarization at each energy before the energy is stepped, the

alignment shifts are typically the same for each polarization stack, so one may apply the alignment data determined for one polarization to the other.

Alternatively, one may append the two polarization stacks together and apply a single alignment to the appended stack. This ensures that the alignment is consistent and the stack dimensions remain the same. It is also typically necessary to apply multiple alignment iterations until there is a convergence in the alignment, such that the variance in pixel shifts is less than 0.1 pixels. It is important to ensure that the alignment procedure has stabilized the position of the magnetosomes through the image sequence. Magnetosome contrast is sufficient at the onset of the edge. However at the pre-edge, iron-rich components do not appreciably absorb the x-rays, and as such, the fiducial markers may change as the energy is scanned. Thus it is sometimes beneficial to use a constant image or region that encloses the magnetosomes to allow for better alignment.

Once a stack is aligned, the transmission images are converted to optical density by selecting an appropriate I_0 region. Choice of an I_0 region has to be taken into account in the initial measurement scan set-up. An appropriate choice of I_0 is typically a region off the cell where there is only the polymer support membrane of the grid or the TEM window present. However if there is no such area available, an area of the cell is the next best choice for I_0 . If the cell is selected as the I_0 region the cellular structure cannot be analyzed for cell density and other pre-edge effects because it has been used as the I_0 . Conversion from transmission mode to optical density is performed by a simple Beer's Law relations $OD = \ln$

(I/I_0). It is important to use the same I_0 region for both polarization measurements in order to ensure that the intensity profiles of each polarization are similarly normalized and thus the resultant XMCD profile is accurate. Furthermore, it is important that the I_0 region is of good statistical precision and free of large glitches which can be achieved by using a large I_0 sampling area as well as the pre-analysis deglitching procedures.

Once both polarization stacks are aligned and converted to optical density stacks, the Fe L edge spectra may be collected from each individual magnetosome by sampling those pixels. One final check to ensure alignment is to average the images at energies corresponding to the on-edge features for each polarization and make an RGB map. This allows one to quickly visualize the overlap of the two polarizations and whether it is suitable (i.e. <0.5 pixel shift). If not the alignment procedure must be modified or iterated. Stacks may be used to generate stack maps at the three key energies where XMCD is the largest (see Chapter 3, figure 7b-d).

Chapter 3

Quantifying the Magnetic Moment of a Single Magnetosome Chain

This paper reports improvements made for STXM-XMCD data collection thereby gaining more accurate and reproducible results. An example of the use of the STXM-XMCD as a quantitative magnetic technique is shown. Analysis of the experimental results obtained with both polarization data collection methods was performed using aXis2000.

Cultures were grown and placed on grids by Prof. Ulysses Lins, Prof. Dennis Bazylinski and co-workers. Karen Lam made the STXM-XMCD measurements at the Canadian Light Source. The author made biochemical STXM measurements at the Advanced Light Source. The data was analyzed by the author of this thesis. The paper was drafted by the author and edited and revised by Prof. Adam P. Hitchcock and Prof. Dennis A. Bazylinski. This paper has been published: 10.1016/j.chemgeo.2012.01.005.



Research paper

Examining the chemistry and magnetism of magnetotactic bacterium *Candidatus Magnetovibrio blakemorei* strain MV-1 using scanning transmission X-ray microscopy

Samanbir S. Kalirai ^a, Karen P. Lam ^a, Dennis A. Bazylinski ^b, Ulysses Lins ^c, Adam P. Hitchcock ^{a,*}

^a Department of Chemistry and Chemical Biology, McMaster University, Hamilton, ON, L8S 4M1 Canada

^b School of Life Sciences, University of Nevada at Las Vegas, Las Vegas, NV, 89154-4004, USA

^c Departamento de Microbiologia Geral, Instituto de Microbiologia Professor Pizulo de Góes, Universidade Federal do Rio de Janeiro, 21941-590, Rio de Janeiro, RJ, Brazil

ARTICLE INFO

Article history:

Received 17 October 2011

Received in revised form 11 January 2012

Accepted 12 January 2012

Available online 21 January 2012

Editor: J. Fein

Keywords:

magnetotactic bacteria

magnetosomes

STXM

XMCD

NEXAFS

Fe 2p

ABSTRACT

Scanning transmission X-ray microscopy (STXM) measurements at the C K, O K and Fe L_{2,3} edges were used to study the magnetotactic bacterium *Candidatus Magnetovibrio blakemorei* strain MV-1 on an individual cell basis. Improved data acquisition methodologies resulting in higher quality results are presented. Visualization of magnetosomes from their O K-edge signal is demonstrated. The Fe L_{2,3} X-ray magnetic circular dichroism (XMCD) signal was used to characterize the magnetic properties of several MV-1 cells on an individual magnetosome basis. The absolute magnetic moment from two cells was evaluated and found to be 0.93(6) of that of saturated abiotic magnetite, or 3.6(2) μB. Previously observed excess Fe (II) was not found in this study, suggesting the prior observation (Lam et al., Chem. Geol. 270 (2010) 110) may have been a radiation damage artifact.

© 2012 Elsevier B.V. All rights reserved.

1. Introduction

Synchrotron-based soft X-ray STXM (Ade and Hitchcock, 2008; Howells et al., 2007) uses near edge X-ray absorption fine structure (NEXAFS) as the contrast mechanism to provide elemental and chemically sensitive imaging at ~25 nm spatial resolution. NEXAFS spectra (Stöhr, 1991) probe the electronic, magnetic and geometric structure of materials by exciting core electrons into empty valence shells. Analysis of image sequences recorded with STXM yield quantitative maps of inorganic and organic materials with elemental specificity and chemical speciation. Since the C, N, O, K-edge and Fe, S, Ca L-edge core levels are well separated, studies at multiple edges provide the ability to determine spectra and quantitative spatial distributions of major biochemical components (protein, lipids, polysaccharides, etc.) in addition to the magnetite magnetosomes, which are the focus of this study. In this regard, STXM has significant advantages relative to basic

microscopic techniques due to its ability to discriminate spectrally, and to provide spectra subjectable to detailed analysis. Further, it offers many advantages over spatially unresolved spectroscopies in the case of environmental and biogeochemical samples, which are usually highly anisotropic. STXMs at beamlines based on elliptically polarizing undulators (EPU) use the capability to vary the orientation of circularly and linearly polarized light to measure and map both linear (Najafi et al., 2008) and magnetic dichroism (Coker et al., in press; Lam et al., 2010). This allows STXM to be used not only as a spatially resolved chemical analysis tool but also as one that discriminates charge and magnetic anisotropies.

X-ray magnetic circular dichroism (XMCD) (Stöhr, 1999; Stöhr and Siegmann, 2006) is a branch of X-ray absorption spectroscopy that provides information about the magnetic structure of materials. The XMCD signal is defined as the difference in edge-jump normalized absorption spectra recorded with parallel and anti-parallel alignment of the photon spin and total magnetic moment vectors (OD_{||}–OD_⊥) (Stöhr and Siegmann, 2006). Detailed XMCD sum rule-based analysis of XMCD signals can be used to determine the total magnetic moment, as well as the individual contributions from spin versus orbital magnetic moments (Stöhr, 1999; Stöhr and Siegmann, 2006). However, sum rule analyses require very high statistical quality and

* Corresponding author. Tel.: +1 905 525 9140.
E-mail address: aph@mcmaster.ca (A.P. Hitchcock).

extended data ranges (Goering et al., 2006b). They have been applied to the complex XMCD signals of magnetite (Goering et al., 2006a, 2006b, 2007; Huang et al., 2004; Kuiper et al., 1997; Pellegrin et al., 1999; Pérez et al., 2009) and other transition-metal oxides (Goering et al., 2002). It is noteworthy that in many situations (e.g. Fe₂O₃ versus Fe₃O₄, Pérez et al., 2009), the Fe L-edge X-ray absorption spectra can be rather similar, yet have quite distinct XMCD. There are also size dependent changes in XMCD of nanoparticles (Pellegrin et al., 1999).

XMCD of abiotic and biologically produced magnetite has been reported by several groups (Carvallo et al., 2008; Goering et al., 2006a, 2007). Staniland et al. (2007) used XMCD to investigate the kinetics of in-vivo formation of magnetite magnetosomes in *Magnetospirillum gryphiswaldense* strain MSR-1. Coupling of STXM to XMCD is a logical and desirable approach for studying the magnetic properties of biogenic (and abiogenic) magnetite in cases such as magnetotactic bacteria, where spatial resolution is required to investigate the magnetic properties of individual cells and individual magnetosomes. Recently, we reported the first such measurements (Lam et al., 2010). In this work, we report a significant improvement in our experimental results, and show for the first time measurements of complementary core edges. In addition we have quantitatively evaluated the total magnetic moment for several cells of the *Candidatus Magnetovibrio blakemorei* (MV-1) magnetotactic bacterial cells.

There are three types of Fe sites in the magnetite crystal structure – a tetrahedral site with Fe (III)-d⁵ oxidation state and octahedral sites occupied by Fe (II)-d⁶ and Fe (III)-d⁵. The Fe L₃ (2p_{3/2}) XMCD spectrum of magnetite (Goering et al., 2006a, 2007; Kuiper et al., 1997; Pellegrin et al., 1999) shows three characteristic peaks which have been correlated based on atomic multiplet calculations to the three distinct sites: a negative peak at 708.1 eV arising mostly from the d⁶ O_h (Fe (II)) site; the positive peak at 709.1 eV associated with the d⁵ T_d (Fe (III)) site; and the negative peak at 709.9 eV arising mostly from the d⁵ O_h (Fe (III)) (Kuiper et al., 1997; Patrick et al., 2002). The site-specific character of the XMCD spectrum of magnetite has been used to determine site occupancies, which allow for differentiation between biological and abiotic (mineral) magnetite (Carvallo et al., 2008; Coker et al., 2007). Other computational results (Antonov et al., 2003; Leonov et al., 2004, 2006) indicate that the correlation between the XMCD spectral features and the projected site specific contributions is more convoluted than that proposed by Patrick et al. (2002). Nolle et al. (2009) have shown that experimental XMCD spectra of complex mixed oxide systems can be deconvoluted to generate species- and site-specific signals and evaluate relative amounts of magnetic and non-magnetic contributions.

Magnetotactic bacteria (MTB) are gram-negative, microaerophilic/anaerobic bacteria found in both freshwater and marine aquatic environments (Bellini, 1963a,b; Bellini, 2009; Blakemore, 1975; Frankel and Blakemore, 1980; Frankel et al., 1979). Blakemore (1975) showed that MTB use a phenomenon known as magnetotaxis in which the MTB use the Earth's magnetic field to orient in order to more efficiently locate and maintain position in anaerobic or micro-aerobic regions of the sediment (known as the oxic-anoxic transition zone) where the chemical/redox environment is optimal for their metabolism (Bazylinski, 1995; Frankel and Bazylinski, 1994). The magnetotaxis effect is possible due to the mineralization of membrane-bounded, intracellular magnetic nanoparticles, referred to as magnetosomes. Depending on the species, magnetosome crystals are composed of ferrimagnetic magnetite (Fe₃O₄) or greigite (Fe₃S₄) (Heywood et al., 1991) and typically range in size from 35 to 120 nm (Bazylinski and Frankel, 2004). Each crystal is surrounded by a phospholipid bilayer membrane which is 3–4 nm thick (Gorby et al., 1988). Magnetosome crystals are typically in the size range of single magnetic domains, thereby maximizing the magnetic moment of each particle (Frankel and Blakemore, 1980) by avoiding the thermal instability of the superparamagnetic regime (Dunlop, 1973) or reduction in magnetic strength due to domain formation.

Differences in the physical properties of magnetosomal and abiotic magnetite and greigite indicate that biomineralization of magnetosome minerals by MTB is a highly controlled biological process. For example, elongation of magnetosome crystals along the (111) axis and their high chemical purity provide a major distinction between biologically- and abiotically-synthesized magnetite single crystals which has potential relevance to exobiology (Carvallo et al., 2008; Jimenez-Lopez et al., 2010; Thomas-Keprta et al., 2000). Physiological evidence also supports a strongly controlled biomineralization of magnetosome minerals. For example, Korneili et al. (2004) have shown the presence of magnetosome vesicles prior to magnetosome formation. The formation of co-aligned magnetosome chains further suggests biological control of their synthesis.

Because of their narrow size distribution, high chemical purity and magnetic response, magnetosome magnetite has garnered much interest for potential applications in medicine, environmental science and technology. Both magnetotactic bacteria and magnetosomes have been proposed for use in nanorobotic devices for mobilized and targeted drug delivery since they are readily located and manipulated using external or internal magnetic fields (Albrecht et al., 2005; Ceyhan et al., 2006; Martel et al., 2009). Studies of the mechanisms of formation of magnetosomes are motivated by the desire to have an in depth understanding of this fascinating example of biomineralization as well as the potential for enhancing biotechnological and environmental applications.

The magnetic properties of magnetosomes have been characterized with several techniques including magnetic force microscopy (Albrecht et al., 2005), low-temperature SQUID magnetometry (Moskowitz et al., 1993), ferromagnetic resonance (Charilou et al., 2011; Fischer et al., 2008; Weiss et al., 2004) and coercivity deconvolution (Egli, 2004). Electron holography measurements in transmission electron microscopes (TEM) have been used to visualize the magnetic properties of magnetosomes (Dunin-Borkowski et al., 1998; McCartney et al., 2001; Simpson et al., 2005). Fe L_{2,3} X-ray magnetic circular dichroism (XMCD) has been used without spatial resolution to study magnetosome extracts (Coker et al., 2007, 2009; Staniland et al., 2007, 2008) and biologically-generated, extracellular magnetic iron oxide deposits (Coker et al., 2006, 2007, 2008, 2009). The first XMCD study of individual magnetosomes within a single MTB cell using synchrotron-based scanning transmission X-ray microscopy (STXM) was reported by our group (Lam et al., 2010). This approach was recently used by Coker et al. (in press) to study extracellular magnetite generated by *Shewanella oneidensis* strain MR-1. Here we report further STXM investigations of *Candidatus Magnetovibrio blakemorei* strain MV-1, using both biologically-sensitive (C 1s, O 1s) and magnetically-sensitive (Fe 2p) edges.

2. Experimental

2.1. Preparation of magnetotactic bacterial cells

Cells of *Candidatus Magnetovibrio blakemorei* were grown in liquid culture as previously described by Dean and Bazylinski (1999). 5–10 μl of a concentrated liquid culture was placed onto a 200-mesh glow-discharged copper grid coated with polyvinyl formal (formvar). The droplet was left standing for several minutes before the liquid was wicked away with filter paper. The grids were left to dry in air.

2.2. STXM-XMCD measurements

Details of the Canadian Light Source (CLS) 10BID-1 soft X-ray spectroscopy beamline (Kaznatcheev et al., 2007), the STXM (Kilcoyne et al., 2003), and the measurement procedures (Ade and Hitchcock, 2008; Lam et al., 2010) have been presented elsewhere. Briefly, monochromatic X-rays are focused by a zone-plate (a circular

diffraction grating) to a small spot (31 nm, based on the Rayleigh criterion, and assuming fully coherent illumination). The sample is mounted on a piezo stage and its position relative to the focussed X-ray spot is controlled at the 2–3 nm level by laser interferometry. The sample is raster scanned while detecting the transmitted flux to form an image. Signals through sample regions (I) are normalized to signals from off-sample regions (I_0) to derive the optical density, $OD = -\ln(I/I_0)$. Acquisition of a sequence of images at energies through an X-ray absorption edge provides spatially resolved NEXAFS spectra.

It is possible in general to measure XMCD either by varying an applied magnetic field, or by comparing the signals recorded with left and right circular polarized X-rays. Since our goal is to interrogate the intrinsic magnetic properties of the magnetotactic bacteria with minimal modifications to their natural state, we have used alternation of the photon polarization. In order to do so it is essential to correctly position the sample relative to the X-ray beam, since XMCD signals only arise from that part of the magnetization for which the sample magnetism is coaxial with the X-ray propagation axis (Stöhr and Siegmann, 2006). The magnetism of a chain of magnetosomes is generally along the long axis of the cell, and thus in the plane of the grid or Si_3N_4 window supporting the cells. In order to generate a non-zero projection of the magnetization vector onto the X-ray propagation axis, the sample is mounted at a 30° angle. For this purpose a sample holder with a wedge was used to create a fixed 30° tilt along the horizontal axis between the surface normal and incoming X-rays. Alternatively, the sample is mounted on a tomography holder (Johansson et al., 2007), which allows arbitrary polar rotation. For XMCD studies, a 30° rotation angle is used. In either of these rotated geometries, horizontal or near-horizontally-oriented magnetosome chains give the largest XMCD signal; vertically oriented chains have zero XMCD. For a perfectly horizontal magnetosome chain, 50% of the magnetization vector is projected on the X-ray propagation axis. Deviation from horizontal further attenuates the XMCD signal by the cosine of the deviation angle.

Improvements to the Elliptically Polarizing Undulator (EPU) at the CLS soft X-ray spectromicroscopy beamline and the STXM_control software have resulted in more reliable data collection relative to our earlier work (Lam et al., 2010). The rate at which the EPU can be switched from left circularly polarized (LCP) to right circularly polarized (RCP) light, while having the electron beam orbit stabilized, was significantly improved such that switching between right and left circular polarization can now be done in ~ 8 s. This allows for alternating RCP/LCP measurements at each photon energy (concurrent mode, method B) which significantly improves reliability over the original procedure used by Lam et al. (2010) in which complete image sequences were measured with one circular polarization, before changing to the opposite polarization (successive mode, method A). In method A each image sequence took ~ 5 h to collect, a period over which there is significant drift in the instrumental response, which resulted in data which required extensive and careful correction. In the improved procedure the circular polarization is alternated at each photon energy (RCP/LCP) (concurrent mode, method B). This results in substantially more precise data, which greatly reduces the effort needed to extract the XMCD. For example, the image alignment parameters for the RCP and LCP polarization subsets are the same since the images for the two polarizations at each photon energy take only a few minutes to collect. A further significant improvement was made by using the point-by-point rather than the line-at-a-time acquisition mode, which required improvements to the STXM_control software. The point-by-point mode significantly improves spatial precision and thus the quality of the individual images and the precision of the spectra extracted from small regions such as individual magnetosomes. The effects of both improvements on data quality are documented below.

2.3. XMCD data analysis

In this work, X-ray absorption spectra are plotted on the as-recorded optical density scales. As the optical density of individual magnetosomes is very weak, there is no absorption saturation, however, the low OD makes the experiment quite challenging. In order to evaluate the total magnetic moment, we have compared quantitatively the strength of the MV-1 XMCD signal to that of abiotic magnetite, since the latter possesses a saturated magnetic moment and has been carefully measured in a strong magnetic field (Goering et al., 2006a). To perform the quantitative comparison, the Fe L_3 spectra of MV-1 recorded with left (LCP) and right (RCP) polarized light are first carefully background-subtracted using identical background functions (typically linear, which is valid over the short energy span of the L_3 signal), before the intensities of the Fe L_3 component are scaled (again using the same factor for both LCP and RCP) to make a best match to the L_3 spectrum of abiotic magnetite (Goering et al., 2006a) outside of the L_3 peak (between 702–705 eV, and 714–718 eV) prior to subtraction. In this way, the ratio of the integrated XMCD signal (705–715 eV) from an MV-1 sample to that for abiotic magnetite provides a quantitative measure of the magnitude of the XMCD and thus the total magnetic moment for that MV-1 sample. In this work we chose to measure only the L_3 component since our L_3 measurements at present have higher statistical accuracy compared to those at the L_2 component. Also, analysis of the L_2 XMCD requires correction for overlap with the magnetically-sensitive L_3 extended fine structure signal (Goering et al., 2006a, 2006b). This requires very long range spectra, which are prohibitively time consuming when making spectroscopic measurements using the image sequence approach. Since only L_3 data has been measured, it is not possible to make a sum rule analysis but the total moment was evaluated by quantitative comparison to the XMCD of abiotic magnetite.

3. Results

3.1. Documenting improved performance

Fig. 1a indicates how the polarization changes with time in the successive (Method A), versus the concurrent (Method B) modes. The benefits of changing to the concurrent mode are documented in Figs. 1–3. An example of the improved STXM-XMCD quality is presented in Fig. 1, which compares the Fe L_3 NEXAFS and XMCD spectra of a magnetosome chain within one MV-1 cell, recorded with method A (July 2009, Fig. 1b) and with method B (September 2009, Fig. 1c). Fig. 1d is a comparison of the fractional noise level in the two measurements, obtained by subtracting an appropriately scaled version of the Fe L_3 XMCD of synthetic magnetite reported by Goering et al. (2007) from the measured XMCD of the magnetosome chain. Clearly the noise level is much larger in the method A measurements (refer to blue line in Fig. 1d) even though the dimensions of the chains and the experimental conditions were similar for the two measurements. The lengths of the magnetosome chains in Figs. 1b (8 magnetosomes) and 1c (9 magnetosomes) are $0.54 \mu\text{m}$ and $0.63 \mu\text{m}$, respectively. The pixel dwell times for the two data sets were 5 and 6 ms, respectively. The exit slits were 8 or $10 \mu\text{m}$, with the value chosen so that the detected signal of the incident beam off the magnetosome chain was below 20 MHz in order to ensure a linear detector response. The noticeable improvement in spectral quality and reproducibility with method B (alternating polarization at each photon energy) can be attributed to the fact that the incident beam intensity at CLS is more stable over shorter than longer periods. In addition to plotting the spectra for each polarization, Figs. 1b and 1c also plot the XMCD spectra obtained by subtracting the anti-parallel (red) spectrum from the parallel spectrum (green). The XMCD spectra of the magnetosome chains are compared to that of the XMCD spectrum of mineral magnetite (Goering et al., 2007), multiplied by a factor of

0.5 to account for the projection of the in-plane magnetization of the magnetosome chain onto the X-ray propagation direction (a 30° tilt angle was used).

In Fig. 1b, the spectra were measured successively for each polarization (method A); thus beam fluctuations and intensity normalized stacks are affected by drifts in the storage ring and beamline conditions. This yields poorer statistics and a poorer match of the pre-

edge absorption profiles of the parallel and anti-parallel spectra. However, when the spectra are recorded concurrently by alternating the polarization at each successive energy (method B), the result is less dependent on the long-term stability of the storage ring and beamline. For samples with relatively long exposures times, as is the case in STXM-XMCD measurements, irradiation causes a build-up of carbon on the sample due to cracking of surface-adsorbed hydrocarbons. Although this was a major concern for measurements using method A, the effect is negligible for measurements using method B since the slow build-up of carbon is tracked in the off-cell portion which is the source of the I_0 signal used for conversion from transmission to optical density. This can be seen by comparing Fig. 2 (method A, successive polarization measurements) and Fig. 3 (method B, concurrent polarization measurements). These figures contrast the difference in the average of all images acquired with (i) left circular polarization (Figs. 2a, 3a) and (ii) right circular polarization (Figs. 2b, 3b), as well as the difference in the LCP and RCP signals in the (iii) pre-edge (704–706 eV, Figs. 2c, 3c) and (iv) iron L_3 (708–711 eV, Figs. 2d, 3d) regions. With the successive measurement mode (method A), the OD range is 0.08 for the pre-edge difference image and 0.09 for the Fe L_3 difference image. This is a significant portion of the total OD in the Fe L_3 peak (0.2–0.3). Spectral distortions are more pronounced in the cellular biomolecular region (used for the I_0) than the magnetosome region, as biological material is more susceptible to radiation damage (Toner et al., 2005). The pre-edge difference image for method A (Fig. 2c) shows a radiation-damage-related OD difference pattern that is systematic and consistent with the structure. In contrast, for method B, the pre-edge difference image (Fig. 3c) is uniform and un-structured, and the total OD range is only 0.02. By switching to concurrent polarization measurements (method B), the decreased data collection time has improved the overall statistical quality while lowering radiation-damage-induced artifacts. The close correlation between the biogenic XMCD and the scaled reference spectrum of magnetite (Goering et al., 2007) (Fig. 1c) exemplifies the increased reliability of concurrent polarization measurement mode.

Fig. 4 documents the improvements that result from acquiring images in the point-by-point mode rather than line-at-a-time mode. In both method A and method B. The absolute OD differences between line-at-a-time and point-by-point mode show that the point-by-point mode is superior (as indicated by less jitter at the edges of the magnetosomes), largely due to the higher spatial precision provided by the point-by-point mode. The absolute OD differences (Fig. 4c and d) are lower and there is a smoother variation in the signal when point-by-point mode is used in conjunction with method B.

3.2. Fe L_3 XMCD studies of cells of strain MV-1

Fig. 5a shows a STXM image at 709.8 eV of an array of strain MV-1 cells. The curved-rod shape of the cells is characteristic of the MV-1 marine vibrioid species. Fig. 5b shows a false color image of the upper right area of Fig. 5a in which the iron signal (the difference of

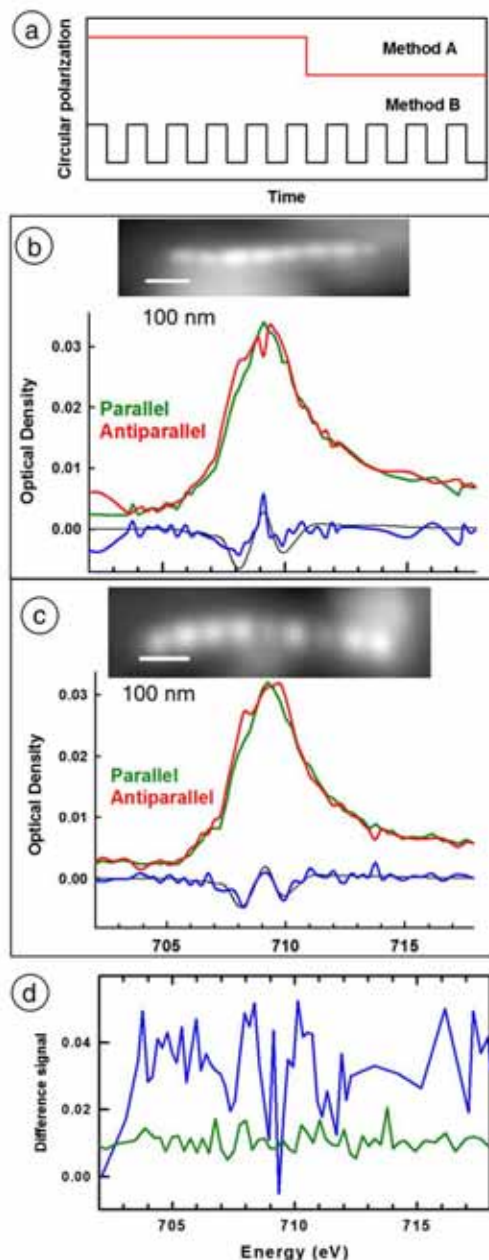


Fig. 1. (a) Schematic of two methods used to measure X-ray magnetic circular dichroism (XMCD). In method A (upper time plot) the left and right circular polarization data are acquired successively, with only a single switch of the circular polarization. In method B (lower time plot) – the left and right circular polarization data is obtained quasi concurrently by switching polarization at each photon energy. (b) Image, Fe 2p spectra and XMCD from a single magnetite magnetosome chain of a cell of *Candidatus Magnetovibrio blakemorei* strain MV-1 recorded with method A (successive mode). (c) Image, Fe 2p spectra and XMCD from a single MV-1 magnetosome chain recorded with method B (concurrent mode). In each case, the derived XMCD signal is plotted in comparison to that from mineral magnetite (black), (Goering et al., 2007) which has been scaled by 0.5. (d) Comparison of the noise in the data from the two measurements, derived in each case by subtracting the XMCD spectrum of mineral magnetite from that of the MV-1 magnetosome chain (blue: difference signal of method A; green: difference signal of method B).

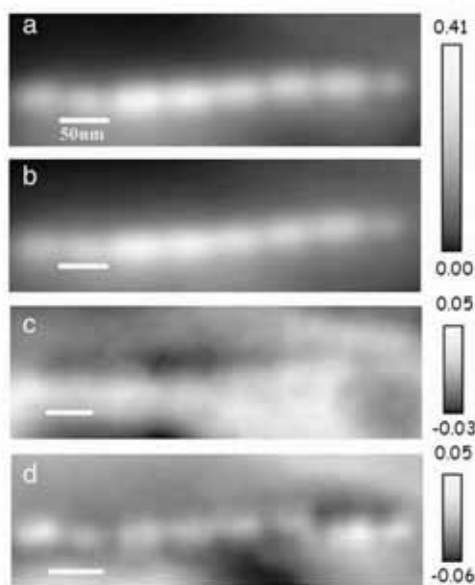


Fig. 2. Average of all images of an Fe L_3 XMCD image sequence measured with method A (successive mode) (a) Average of all images of the LCP stack; (b) Average of all images of the RCP stack; (c) The (LCP-RCP) difference in the pre-edge region (704–706 eV); (d) The (LCP-RCP) difference over the Fe L_3 peak (708–711 eV). Gray scales indicate the range of optical density (OD) or difference in optical density (ΔOD).

$OD_{709.8}-OD_{704}$ images) is in red and the pre-Fe 2p signal at 704 eV (which is dominated by the cells and other non-Fe material), is in blue. The peak of the Fe L_3 signal occurs at 709.8 eV. However the OD at that energy also has contributions from the underlying

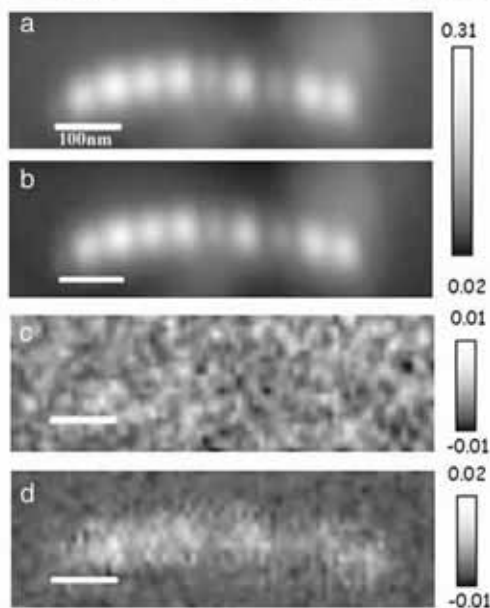


Fig. 3. Average of all images of a Fe L_3 XMCD image sequence measured with method B (concurrent mode). (a) The LCP stack; (b) Average of all images of the RCP stack; (c) The (LCP-RCP) difference in the pre-edge region (704–706 eV); (d) The (LCP-RCP) difference over the Fe L_3 peak (708–711 eV). Gray scales indicate the OD or ΔOD range.

absorption by the magnetite oxygen and non-Fe containing species. The latter signal is removed by subtracting the pre-Fe absorption image at 704 eV; thus, the $(OD_{709.8}-OD_{704})$ difference shows only the iron components. The single-domain magnetic iron particles in the chains synthesized by MTBs are found to have their magnetic vector pointing in the same direction in most cases. Assuming that the magnetic field (predominantly that of the earth) was present at the droplet when the sample was deposited and was uniform over the few tens of microns field of view of Fig. 5a, then one would expect the magnetic vector of each chain and thus, the cells, to be oriented along the magnetic field lines present at the droplet. However, Fig. 5a (and other lower magnification images sampling many more cells) shows that the cells of MV-1 are essentially randomly oriented. In contrast to the preferential orientation that probably occurs much of the time in their natural environment, MTB deposited on these TEM grids were not strongly oriented along the Earth's geomagnetic field. This is most likely due to turbulence in the droplet caused by the rapid capillary action that occurred when the excess fluid was wicked away. As the fluid is removed, the magnetic alignment of the cells is disturbed and the cells are unable to restore their natural ordering with the external magnetic field before they lose mobility due to the absence of liquid medium.

Fig. 6 presents results from a STXM-XMCD study of two overlapping MV-1 cells. An Fe L_3 image sequence was recorded using the concurrent XMCD polarization measurement mode. Fig. 6a displays the average of all images between 708.6 eV and 710 eV in the LCP mode which corresponds to the full Fe L_3 peak. The NEXAFS and XMCD spectra of the three colored regions (two individual magnetosomes and an overlap of two others) are presented in Fig. 6b–d. In each spectral plot the red curve is that recorded with RCP while the green curve is that recorded with LCP. For the green magnetosome (Fig. 6b), the LCP mode is the parallel spectrum while the RCP mode is the anti-parallel spectrum. The opposite is true for the red magnetosome (Fig. 6c) since the LCP mode has the anti-parallel and the RCP mode has the parallel spectral shape. Thus, the magnetic orientations of the two chains are opposite to one another. This is shown by the shapes of the RCP-LCP difference spectra (Fig. 6b, c) which are inverted relative to each other. The RCP-LCP difference spectrum of the horizontally-oriented MTB (red, Fig. 6c) shows the characteristic XMCD of magnetite while that of the more vertically-oriented MTB (green, Fig. 6c) shows the inverse of the magnetite reference spectrum. This example nicely illustrates that STXM-XMCD is sensitive to both the magnitude and orientation of the magnetic vector of individual magnetosomes. This is further exemplified by the signal extracted from the intersection of the two chains (Fig. 6d), where the XMCD signal disappears due to the additive nature and opposite orientation of the XMCD from the two magnetosomes in this region.

Fig. 7a compares the corrected average XMCD spectrum from both chains (inset of Fig. 7a indicates the regions of the specific magnetosomes from each chain that were selected for measurements), in comparison to the XMCD spectrum of mineral magnetite. Selecting just the central part of the best aligned magnetosomes gives the best possible representation of the magnetic signal since the signal from the edges of the magnetosomes is relatively reduced due to the finite spatial resolution of STXM and the wings of the response function (Leontowich et al., 2011). The Fe L_3 component for each chain was isolated and matched to the edge-jump normalized data reported by Goering et al. (2007), as described in experimental Section 2.3. The tilted chain (red in Fig. 7a) has a reduced magnetic moment (only the projection on the horizontal axis is sensed) and its orientation is opposite to that of the horizontal chain (green in Fig. 7a). Prior to averaging with the XMCD of the two chains, the XMCD from the tilted chain was inverted and then rescaled by a factor of -1.30 to account for the 40° in-plane tilt from horizontal. As shown in Fig. 7a, the match on an absolute scale of the corrected, averaged XMCD from these two chains to the XMCD of abiotic

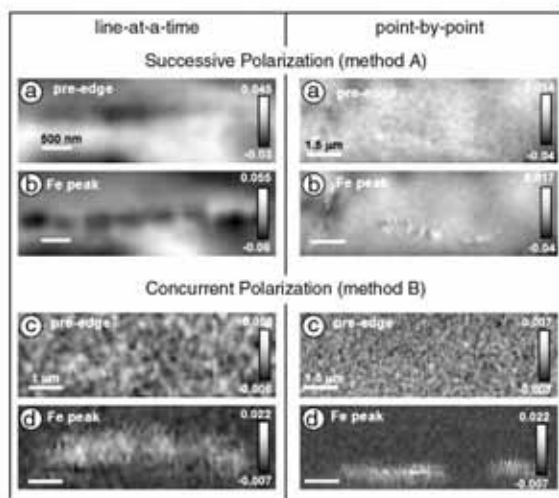


Fig. 4. Comparison of Fe L_3 XMCD data recorded using (left) line-at-a-time mode; and (right) point-by-point scanning for successive (upper block of 4 images) and concurrent (lower block of 4 images) modes. Within each block, the upper figures (labeled a or c) are the differences averaged over a region of pre-edge energies (704.5 to 706.5 eV) for opposite circular polarization (LCP–RCP), while the lower images (labeled b or d) are the differences integrated over the Fe L_3 peak energies (707.5 to 711.5 eV) for opposite circular polarization (LCP–RCP). The concurrent mode shows less statistical variation as well as less absolute variation in the optical density between the two polarization images. Gray scales indicate the ΔOD range.

magnetite is excellent. Integration of the absolute value of that XMCD from the MV-1 magnetosome magnetite compared to that from abiotic magnetite gives a ratio of 0.93(6) for the magnetic signal of MV-1 magnetosomes relative to that of magnetite. Since the magnetic moment of magnetite is 3.9 μ_B (Goering et al., 2006a, 2006b, 2007), our result for this set of two MV-1 chains is an average moment of 3.6(2) μ_B .

An approach to look for possible anomalies in the magnetosome XMCD signal, perhaps associated with partial site occupancy (Coker et al., 2007), is to create “XMCD images” from each peak of the L_3 signal, which are more or less specific to each of the 3 crystal sites. Fig. 7b–d are images of the XMCD signal averaged over each of the three characteristic peaks of the XMCD. Except for the cross-over point where the overlap of opposite oriented signals nearly cancels the XMCD signal (see Fig. 6d), there is a clear signal in each channel, with approximately similar signal levels, taking into account the very small amount of magnetic material contributing to the signal. In each channel, the sense of the XMCD signal is opposite between the two magnetosomal chains and is inverted for Fig. 7c relative to Fig. 7b and 7d, which is consistent with the extracted XMCD spectra.

3.3. Biochemical mapping of cells of strain MV-1

C 1s and O 1s image sequences were measured from several cells of strain MV-1 in order to map the biochemical components of the cells. Fig. 8a presents the reference spectra for protein (albumin, green), polysaccharide (modeled as glucose, red) and $CaCO_3$ (blue) reported by Lawrence et al. (2003), which were used to generate component maps from a C 1s image sequence using singular value decomposition (SVD) (Ade and Hitchcock, 2008). SVD is a matrix decomposition method used to rapidly find the optimum solution to a set of linear equations which are highly over-determined. The output of the SVD analysis is a set of maps for

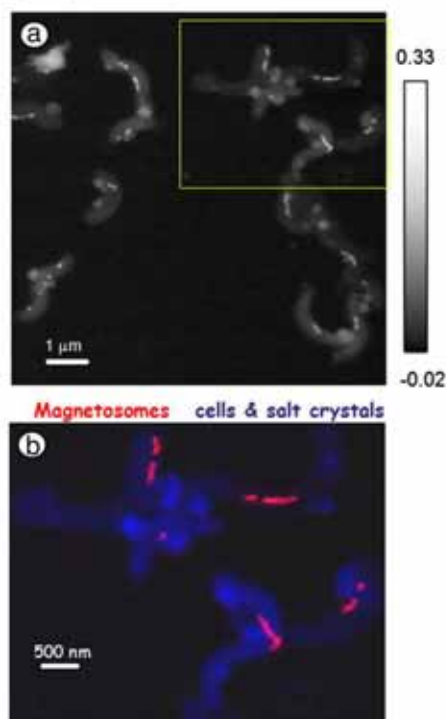


Fig. 5. (a) STXM OD image at 709.8 eV of a number of cells of strain MV-1; (b) a false color image of the upper right area in Fig. 6a, where the iron signal (from $OD_{709.8} - OD_{704}$) is in red and the pre-Fe 2p signal at 704 eV is in blue.

each component for which a reference spectrum is provided. Fig. 8b is a false-color image of the spatial distributions of protein (red), polysaccharide (green) and $CaCO_3$ (blue). A principal component analysis (PCA) and a subsequent cluster analysis (Lerotic et al., 2005; Jacobsen, 2011) were also performed. This multivariate statistical analysis technique first transforms the data into a set of ranked, orthogonalized variables (or principal components) and then seeks clustering in the principal component variable space which identifies spectrally unique components. PCA combined with cluster and target analysis provides unsupervised mapping of spectrally distinct regions as well as extraction of their spectra. PCA/cluster analysis of the C 1s image sequence identified three spatial regions that have distinct absorption spectra (Fig. 8c) which were identified by this approach as the interior cellular structure (green), the extracellular polymeric substance (EPS) (red) and a mineral region (blue). The spectra of the cellular region and the EPS are similar, with the largest difference being a higher optical density inside the cell which gives clear definition to the MV-1 cells. Also, in the EPS region there is an increase, relative to the characteristic protein spectral features at 285.15 eV and 288.20 eV, in the height of the polysaccharide NEXAFS peak at 289.35 eV. The differentiation of the cell and EPS was further confirmed by the SVD analysis (Fig. 8b). The spectrum of the third region (mineral, blue) has less well defined C 1s spectral structure and a much larger non-carbon signal. This is consistent with its attribution to a mineral material, as is also supported by the close match in location to the region of high $CaCO_3^{2-}$ concentration found by the SVD analysis (Fig. 8b). The peaks at 297 and 300 eV in the cellular (green) and EPS (red) spectra (Fig. 8c) are from potassium ions.

20

S.S. Kalirai et al. / Chemical Geology 300–301 (2012) 14–23

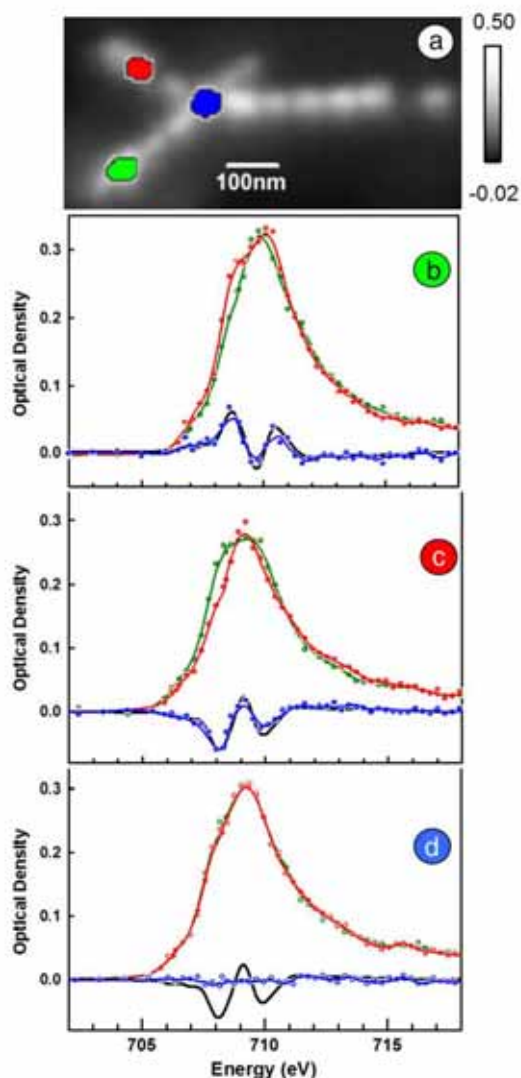


Fig. 6. (a) Average of images in the Fe L_{α} peak (708.6–710 eV) of the magnetosome chains of two overlapping MV-1 cells. (b) to (d) present the Fe L_{α} LCP/RCP spectra of the three colored areas shown in (a), along with their difference spectra (RCP-LCP). In each case, the red spectrum is that recorded with RCP while the green spectrum is that recorded with LCP; (b) data for the green magnetosome; (c) data for the red magnetosome; (d) data for the blue magnetosome. Black lines in Fig. 6(b)–(d) are scaled XMCD spectra of reference magnetite (Goering et al. 2007).

The O 1s analysis is more complex, because the O 1s edge has contributions from both the magnetosome and organic components of bacteria. Fig. 9a shows the average of all images from 524.0 to 560.8 eV. In addition to the MV-1 cells, salt crystals and magnetosome chains are clearly visible. The spectra of these regions are shown in Fig. 9b along with O 1s reference spectra of magnetite and protein. The O 1s spectrum of the magnetosomes (red curve in Fig. 9b) was generated by subtracting the O 1s spectrum of the adjacent cellular material from the spectrum extracted at the location of the

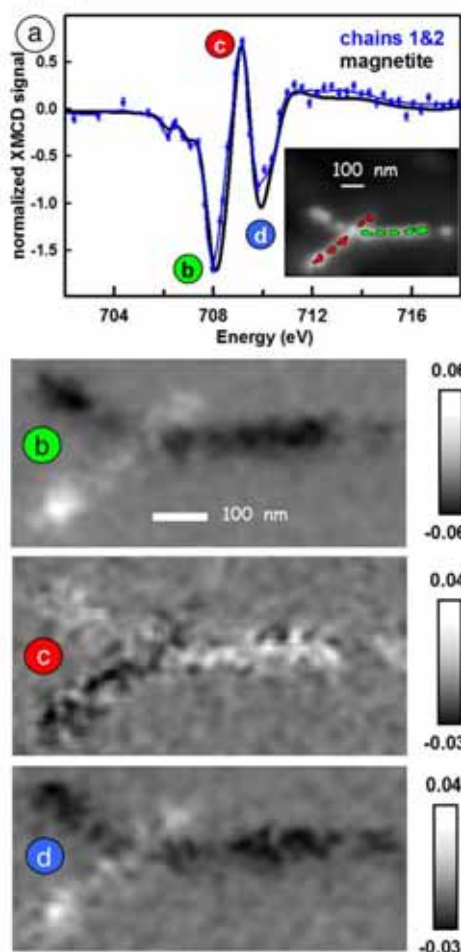


Fig. 7. (a) Corrected average XMCD spectra of the two chains (data points: blue dots with error bars; blue line, smoothed guide to the eye; inset image with red and green markers indicates the areas from which spectral data was extracted) compared to that of mineral magnetite (black, Goering et al. 2007). The RCP and LCP spectra of each chain were background subtracted and the intensity scaled to match the edge-normalized data of Goering et al. (2007). See text for description of how the two opposing polarity signals were scaled and averaged. The XMCD data of mineral magnetite was reduced by 50% to account for the 30° azimuthal tilt angle of the MV-1 sample. (b) Image of the XMCD signal that is a composite of images from 707.8–708.5 eV corresponding to the first, negative peak in the XMCD spectrum shown in 7a; (c) Image of the XMCD signal that is a composite of images from 709 to 709.3 eV corresponding to the second, positive peak in the XMCD spectrum shown in 7a; (d) Image of the XMCD signal that is a composite of images from 709.9 to 710.5 eV corresponding to the third, negative peak in the XMCD spectrum shown in 7a.

magnetosomes. The amount of cellular signal subtracted is such that there is almost equal O 1s contribution from the organic material and magnetite. After this processing, there is a good match between the O 1s spectra of the magnetosomes and magnetite (red and black curves in Fig. 9b). The cellular component (green in Fig. 9b) shows a close match to that of reference albumin at the main O 1s \rightarrow $\pi^*_{C=O}$ peak (532.1 eV). However, the σ^*_{C-O} signal in the continuum region (536–546 eV) is much larger in the cellular spectrum than in the spectrum of pure protein, due to the presence of many other

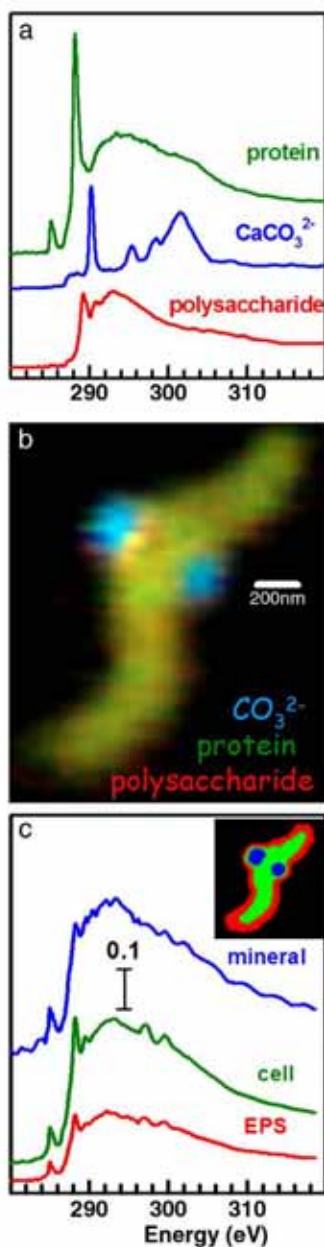


Fig. 8. (a) C 1s reference spectra of protein (human serum albumin, green), CaCO_3 (calcite, blue) and polysaccharide (represented as glucose, red) (Lawrence et al., 2003). (b) Color-coded composite of the 3 component maps derived by fitting the reference spectra of Fig. 8a to a C 1s image sequence from an MV-1 magnetotactic bacterial cell (same color-coding as in Fig. 8a). (c) The spectra of the spatial regions indicated in the inset RGB composite, which were identified by a combination of principle component and cluster analysis. The peaks at 297 eV and 300 eV arise from K^+ . See text for further details.

oxygen containing species, such as lipids and polysaccharides, within the body of the MTB cell. Lipids and polysaccharides have little or no signal around 532 eV but much larger signal than protein in the 536–544 eV region due to their aliphatic character which leads to strong O

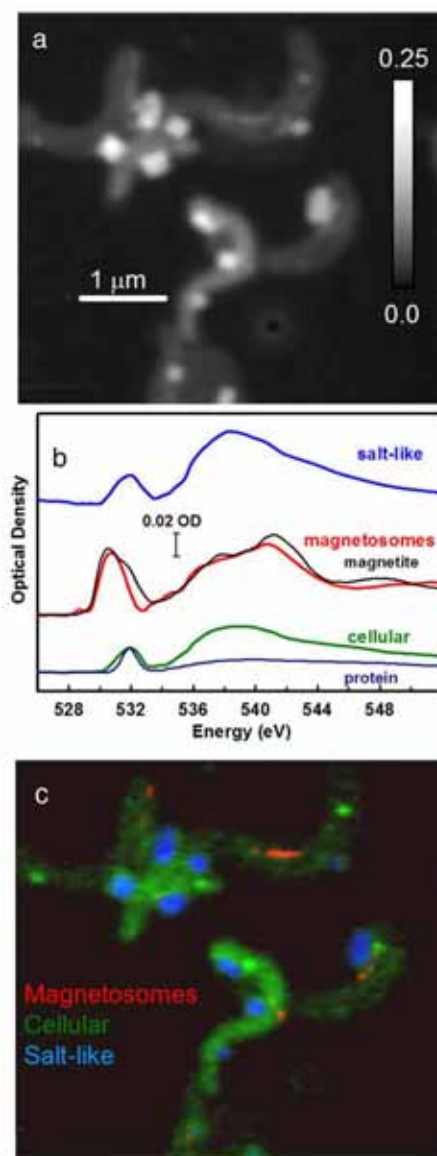


Fig. 9. (a) Average of all images of an O 1s stack (524.0–560.8 eV). (b) Spectra extracted from the cellular regions, the magnetosome chain, and the salt crystals. The displayed spectrum of the magnetosome chain has had the signal from the surrounding cellular material subtracted. The O 1s spectra of magnetite (black) and protein (dark blue) are plotted for comparison. (c) Color-coded composite of magnetosome (red), cellular (green) and salt-like (blue) component maps derived by fitting the reference spectra of Fig. 9b to the O 1s image sequence (see text for further details).

$1s \rightarrow \sigma^*_{\text{C-O}}$ transitions. Detection of the magnetite magnetosomes at the O 1s edge is more difficult than at the Fe 2p edge because the magnetite-specific O 1s feature is relatively weak. However, it is possible to map the magnetosomes because magnetite has a low-lying O $1s \rightarrow (O 2p - Fe 3 d)$ peak at 530.2 eV, which is at a lower energy than the lowest energy biological signal, the O $1s \rightarrow \pi^*_{\text{C=O}}$ peak of protein at 532.1 eV. The O 1s NEXAFS spectra of protein, pure mineral magnetite and the mineral inclusions were used to fit the O 1s stack and thus

visualize magnetosomes from their O 1s signal, Fig. 9c is a color-coded composite of the magnetosome (red), cellular (green) and salt (blue) components determined by an SVD analysis of the O 1s image sequence.

4. Discussion

The use of concurrent polarization mode (method B) (Figs. 1–3) and point-by-point image acquisition (Fig. 4) for STXM-XMCD has resulted in significantly improved results relative to our previously reported spatial resolved XMCD measurements (Lam et al., 2010). The current study demonstrates improvement of XMCD spectra obtained from individual magnetosomes as well as from full chains. Lam et al. (2010) suggested that there was a difference between the Fe (II)/Fe (III) ratio of the MV-1 MTB magnetite and that of abiotic mineral magnetite. However, this more accurate study finds a much smaller difference between the XMCD of magnetosome magnetite and that of abiotic magnetite. The previously observed higher relative amount of Fe (II) may have been an artifact of radiation damage, which reduces Fe (III) to Fe (II), as reported by Toner et al. (2005) and Yano et al. (2005). The improved efficiency of the polarization-switching mode has significantly reduced the impact of radiation damage on STXM-XMCD measurements. Radiation damage in STXM has two effects: contamination of the sample surface (mainly with build-up of carbonaceous material) and photoreduction. By changing our measurement method, the optical density distortions due to radiation-induced carbon build-up are minimized and the total dose used is reduced so there is less photoreduction of the magnetite.

The quantitative XMCD signal averaged over the two chains of magnetite magnetosomes (Fig. 7a) is in nearly quantitative agreement with the XMCD of mineral magnetite (Goering et al., 2007). There still appears to be a slightly higher Fe (II)/Fe (III) ratio in the biological magnetite relative to mineral magnetite, but the effect is much less pronounced than reported by Lam et al. (2010). In addition, although a weak effect, the Fe (II) XMCD peak appears to be shifted to slightly lower energy relative to its counterpart in the XMCD spectrum of mineral magnetite (Goering et al., 2007) and there are other minor differences in the region of the XMCD signal from the Fe (III) O_h site (see Fig. 7a). We have shown it is possible to visualize magnetosomes at the O 1s edge (see Fig. 9) despite the much larger O 1s signal from biological material. This is the first time that magnetosome chains have been mapped using O 1s spectromicroscopy.

This study is a good example of how NEXAFS and XMCD signals recorded at high spatial resolution in STXM provide a highly sensitive probe of both the biochemistry and the magnetization. The ability to measure both the magnitude and the direction of the magnetization has great potential to provide additional insight into magnetosome biomineralization mechanisms. XMCD, along with NEXAFS, may yield important information regarding the fate of magnetosomes during cell division, such as elucidating how magnetosome chains split and grow within daughter cells. Previous studies have relied on TEM to investigate the distribution of magnetosomes during cell division (Staniland et al., 2010). We are striving to use gentler sample preparation methods to allow for passive alignment of bacteria – for example, introduction of X-ray transparent Si₃N₄ windows into culture, as outlined by Lawrence et al. (2003). STXM-XMCD studies of such samples may yield further information on the biochemical or environmental mechanisms that lead to “south-seeking” behavior (in the northern hemisphere), which is observed in a minority of cells in all cultures of polar magnetotactic bacteria, including MV-1. Note that a south-seeking cell adjacent to a north seeking cell is one possible explanation of the opposite polarity of moments found in the set of MV-1 cells presented in Figs. 6, and 7. Another aspect of magnetotactic bacteria that could be studied effectively with STXM-XMCD is the nature and effect of gaps between chains of magnetosomes exhibited within a single cell by some magnetotactic species grown in culture. Examples of these gaps are clearly visible in Figs. 5

and 6a. Bazylinski et al. (1995) commented on the presence of these gaps in cells of strain MV-1 and suggested that, since all the elongated crystals were aligned along their long axes within the cell, the different parts of the magnetosome chain would also be magnetized in the same direction. Since electron holographic studies map field lines rather than explicitly measure the magnetization of individual magnetosomes it might be difficult to verify that point with electron holography. Thus, the ability of STXM-XMCD to study the orientation and magnitude of the magnetism of each magnetosome within a cell could add significantly to other methods being used to investigate this fascinating biomineralization system.

Acknowledgments

This work was supported by NSERC (Canada) (Hitchcock) and by the U.S. National Science Foundation grant EAR-0920718 (Bazylinski). We thank Dr. Eberhard Goering (MPH-Metallforschung, Stuttgart) for supplying the Fe L_{2,3} and XMCD reference spectra of magnetite. We thank two anonymous referees for useful suggestions for improvements to the initial manuscript. The XMCD studies were carried out at the STXM on beamline 10B1 at the Canadian Light Source (CLS), which is supported by the Canada Foundation for Innovation (CFI), NSERC, Canadian Institutes of Health Research (CIHR), National Research Council (NRC) and the University of Saskatchewan. We thank Drs. Jian Wang and Chithra Karunakaran for their expert support at the CLS. The C 1s and O 1s data was measured at the STXM on beamline 11.0.2 at the Advanced Light Source (ALS), which is supported by the Director, Office of Energy Research, Office of Basic Energy Sciences, Materials Sciences Division of the U.S. Department of Energy, under Contract no. DE-AC02-05CH11231. We thank Dr. Tolek Tyliczszak for his expert support of the ALS instrumentation.

References

- Ade, H., Hitchcock, A.P., 2008. NEXAFS microscopy and resonant scattering: composition and orientation probed in real and reciprocal space. *Polymer* 49, 643–675.
- Albrecht, M., Janke, V., Sievers, S., Siegner, U., Schüller, D., Heyen, U., 2005. Scanning force microscopy study of biogenic nanoparticles for medical applications. *Journal of Magnetism and Magnetic Materials* 290–291, 269–271.
- Antonov, V.N., Harmon, B.N., Yaresko, A.N., 2003. Electronic structure and x-ray magnetic circular dichroism in Fe₂O₃ and Mn-, Co- or Ni-substituted Fe₂O₃. *Physical Review B* 67, 024417.
- Bazylinski, D.A., 1995. Structure and function of the bacterial magnetosome. *ASM News* 61, 337–343.
- Bazylinski, D.A., Frankel, R.B., 2004. Magnetosome formation in prokaryotes. *Nature Reviews Microbiology* 2, 217–230.
- Bazylinski, D.A., Frankel, R.B., Heywood, B.R., Mann, S., King, J.W., Donaghy, P.L., Hanson, A.K., 1995. Controlled biomineralization of magnetite (Fe₃O₄) and greigite (Fe₇S₈) in a magnetotactic bacterium. *Applied and Environmental Microbiology* 61, 3232–3239.
- Bellini, S., 1963a. Su di un particolare comportamento di batteri d'acqua dolce (On a unique behavior of freshwater bacteria). Institute of Microbiology, University of Pavia, Italy, internal report.
- Bellini, S., 1963b. Ulteriori studi sui “batteri magnetosensibili” (Further studies on magnetotactic bacteria). Institute of Microbiology, University of Pavia, Italy, internal report.
- Bellini, S., 2009. Further studies on “magnetosensitive bacteria”. *Chinese Journal of Oceanology and Limnology* 27, 6–12.
- Blakemore, R.P., 1975. Magnetotactic bacteria. *Science* 190, 377–379.
- Carvalho, C., Sainciaviti, P., Arrio, M., Menguy, N., Wang, Y., Ora-Nguema, G., Brice-Proleta, S., 2008. Biogenic vs. abiogenic magnetite nanoparticles: a XMCD study. *American Mineralogist* 93, 880–885.
- Ceyhan, B., Alhorn, P., Lang, C., Schüller, D., Niemeyer, C.M., 2006. Semisynthetic biogenic magnetosome nanoparticles for the detection of proteins and nucleic acids. *Small* 2, 1251–1255.
- Charilou, M., Winkhofer, M., Gehring, A.U., 2011. Simulation of ferromagnetic resonance spectra of linear chains of magnetite nanocrystals. *Journal of Applied Physics* 109, 093903.
- Coker, V.S., Patrick, R.A.D., van der Laan, G., Lloyd, J.R., 2006. Formation of Magnetic Minerals by Non-Magnetotactic Prokaryotes in Magnetoreception and Magnetotaxis in Bacteria. *Microbiol Monograph*, 3. Springer, Heidelberg, pp. 275–301.
- Coker, V.S., Pearce, C.I., Lang, C., van der Laan, G., Patrick, R.A.D., Telling, N.D., Schüller, D., Arenholz, E., Lloyd, J.R., 2007. Cation site occupancy of biogenic magnetite compared to polygenic ferrite spinels determined by X-ray magnetic circular dichroism. *European Journal of Mineralogy* 19, 707–716.
- Coker, V.S., Pearce, C.I., Patrick, R.A.D., van der Laan, G., Charnock, J.M., Telling, N.D., Arenholz, E., Lloyd, J.R., 2008. Probing the site occupancies of Co-, Ni-, and Mn-

- substituted biogenic magnetite using XAS and XMCD. *American Mineralogist* 93, 1119–1132.
- Coker, V.S., Telling, N.D., van der Laan, G., Patrick, R.A.D., Pearce, C.I., Arenholz, E., Tuna, F., Winpenny, R.E.P., Lloyd, J.R., 2009. Harnessing the extracellular bacterial production of nanoscale cobalt ferrite with exploitable magnetic properties. *ACS Nano* 3, 1922–1925.
- Coker, V.S., Byrne, J.M., Telling, N.D., van der Laan, G., Lloyd, J.R., Hitchcock, A.P., Wang, J., Patrick, R.A.D., in press. The application of STXM-XMCD to characterise the bio-gene interface during the dissimilatory reduction of Fe(III)-oxyhydroxide. *Geobiology*.
- Dean, A.J., Bazylinski, D.A., 1999. Genome analysis of several magnetotactic bacterial strains using pulsed-field gel electrophoresis. *Current Microbiology* 39, 219–225.
- Dunin-Borkowski, R.E., McCartney, M.R., Frankel, R.B., Bazylinski, D.A., Pósfai, M., Buseck, P.R., 1998. Magnetic microstructure of magnetotactic bacteria by electron holography. *Science* 282, 1868–1870.
- Dunlop, D.J., 1973. Superparamagnetic and single-domain threshold sizes in magnetite. *Journal of Geophysical Research Solid Earth* 78, 1780–1793.
- Eggl, K., 2004. Characterization of individual rock magnetic components by analysis of remanence curves. 1. Unmixing natural sediments. *Studia Geophysica et Geodaetica* 48, 391–446.
- Fischer, H., Mastrogioacomo, G., Lüfßer, J.F., Warthmann, R.J., Weidler, P.G., Gehring, A.U., 2008. Ferromagnetic resonance and magnetic characteristics of intact magnetosome chains in *Magnetospirillum gryphiswaldense*. *Earth and Planetary Science Letters* 270, 200–208.
- Frankel, R.B., Bazylinski, D.A., 1994. Magnetotaxis and magnetic particles in bacteria. *Hyperfine Interactions* 90, 135–142.
- Frankel, R.B., Blakemore, R.P., 1980. Navigational compass in magnetic bacteria. *Journal of Magnetism and Magnetic Materials* 15–18, 1562–1564.
- Frankel, R.B., Blakemore, R.P., Wolfe, R.S., 1979. Magnetite in freshwater magnetic bacteria. *Science* 203, 1355–1357.
- Goering, E., Justen, M., Geissler, J., Rüdiger, U., Rabe, M., Ueberodt, G.G., Schütz, G., 2002. Magnetic anisotropy of textured CrO₂ thin films investigated by X-ray magnetic circular dichroism. *Applied Physics A: Materials Science & Processing* 75, 747–753.
- Goering, E., Gold, S., Laikoti, M., Schütz, G., 2006a. Vanishing Fe 3d orbital moments in single-crystalline magnetite. *Europhysics Letters* 73, 97–103.
- Goering, E., Laikoti, M., Gold, S., 2006b. Comment on "Spin and Orbital Magnetic Moments of Fe₃O₄". *Physical Review Letters* 96, 039701.
- Goering, E.J., Laikoti, M., Gold, S., Scheutz, G., 2007. Absorption spectroscopy and XMCD at the Verwey transition of Fe₃O₄. *Journal of Magnetism and Magnetic Materials* 310, e249–e251.
- Gorby, Y.A., Beveridge, T.J., Blakemore, R.P., 1988. Characterization of the bacterial magnetosome membrane. *Journal of Bacteriology* 170, 834–841.
- Heywood, B.R., Bazylinski, D.A., Garratt-Reed, A.J., Mann, S., Frankel, R.B., 1991. Controlled biosynthesis of greigite (Fe₃S₄) in magnetotactic bacteria. *Naturwissenschaften* 77, 536–538.
- Howells, M., Jacobsen, C., Warwick, T., 2007. In: Hawkes, P.W., Spence, J.C.H. (Eds.), *Principles And Applications of Zone Plate X-Ray Microscopes in Science of Microscopy*. Springer, NY.
- Huang, D.J., Chang, C.F., Jeng, H.-T., Guo, G.Y., Lin, H.-J., Wu, W.B., Ku, H.C., Fujisori, A., Takahashi, Y., Chen, C.T., 2004. Spin and orbital magnetic moments of Fe₃O₄. *Physical Review Letters* 93 (077204), 1–4.
- Jacobsen, C.J.J., 2011. PCA_GUI and other useful IDL routines for analysis of soft X-ray microscopy data is available at <http://xrm.phys.northwestern.edu> (last accessed, 24-Feb-2011).
- Jimenez-Lopez, C., Romanek, C.S., Bazylinski, D.A., 2010. Magnetite as a prokaryotic biomarker: a review. *Journal of Geophysical Research Biogeosciences* 115, G00G03.
- Johansson, G.A., Tyliczak, T., Mitchell, G.E., Keefe, M., Hitchcock, A.P., 2007. Three dimensional chemical mapping by scanning transmission X-ray spectromicroscopy. *Journal of Synchrotron Radiation* 14, 395–402.
- Kaznatcheev, K.V., Karanakaran, C., Lanke, U.D., Urganah, S.G., Obst, M., Hitchcock, A.P., 2007. Soft X-ray spectromicroscopy beamline at the CLS: commissioning results. *Nuclear Instruments and Methods in Physics Research Section A* 582, 96–99.
- Kilcoyne, A.L.D., Tyliczak, T., Steele, W.F., Fakra, S., Hitchcock, P., Franck, K., Anderson, E., Harteneck, B., Richter, E.G., Mitchell, G.E., Hitchcock, A.P., Yang, L., Warwick, T., Ade, H., 2003. Interferometrically controlled scanning transmission microscopes at the advanced light source. *Journal of Synchrotron Radiation* 10, 125–136.
- Komeili, A., Hojatollah, V., Beveridge, T.J., Newmann, D.K., 2004. Magnetosome vesicles are present before magnetite formation, and MamA is required for their activation. *Proceedings of the National Academy of Sciences of the United States of America* 101, 3839–3844.
- Kuiper, P., Searle, B.G., Dada, L.-C., Wolf, R.M., van der Zaag, P.J., 1997. Fe L_{2,3} linear and circular dichroism of Fe₃O₄. *Journal of Electron Spectroscopy and Related Phenomena* 86, 107–113.
- Lam, K.P., Hitchcock, A.P., Obst, M., Lawrence, J.R., Swerhone, G.D.W., Leppard, G.G., Tyliczak, T., Karanakaran, C., Wang, J., Kaznatcheev, K., Bazylinski, D.A., Lins, U., 2010. X-ray magnetic circular dichroism of individual magnetosomes by Scanning Transmission X-ray Microscopy. *Chemical Geology* 270, 110–116.
- Lawrence, J.R., Swerhone, G.D.W., Leppard, G.G., Araki, T., Zhang, X., West, M.M., Hitchcock, A.P., 2003. Scanning transmission X-ray, laser scanning, and transmission electron microscopy mapping of the exopolymeric matrix of microbial biofilms. *Applied and Environmental Microbiology* 69, 5543–5554.
- Leonov, L., Yaresko, A.N., Antonov, V.N., Korotin, M.A., Anisimov, V.I., 2004. Charge and orbital order in Fe₃O₄. *Physical Review Letters* 93, 146404.
- Leonov, L., Yaresko, A.N., Antonov, V.N., Anisimov, V.I., 2006. Electronic structure of charge-ordered Fe₃O₄ from calculated optical, magneto-optical Kerr effect, and O K-edge x-ray absorption spectra. *Physical Review B* 74, 165117.
- Leontowich, A.F.G., Tyliczak, T., Hitchcock, A.P., 2011. Measurement of the point spread function of a soft X-ray microscope by single pixel exposure of photoresists. In: Jaha, I. (Ed.), *Damage to VUV, EUV, and X-ray Optics: Proc. SPIE*, 8077, pp. 0–8.
- Lerotic, M., Jacobsen, C., Gillow, J.B., Francis, A.J., Wirick, S., Vogt, S., Maser, J., 2005. Cluster analysis in soft X-ray spectromicroscopy: finding the patterns in complex specimens. *Journal of Electron Spectroscopy and Related Phenomena* 144–147, 1137–1143.
- Martel, S., Mohammadi, M., Felloul, O., Lu, Z., Pouponneau, P., 2009. Flagellated magnetotactic bacteria as controlled MRI-trackable propulsion and steering systems for medical nanorobots operating in the human microvasculature. *International Journal of Robotics Research* 28, 571–582.
- McCartney, M.R., Lins, U., Farina, M., Buseck, P.R., Frankel, R.B., 2001. Magnetic microstructure of bacterial magnetite by electron holography. *European Journal of Mineralogy* 13, 685–689.
- Moskowitz, B.M., Frankel, R.B., Bazylinski, D.A., 1993. Rock magnetic criteria for the detection of biogenic magnetite. *Earth and Planetary Science Letters* 120, 283–300.
- Najafi, E., Hernández Cruz, D., Obst, M., Hitchcock, A.P., Douhand, B., Pireaux, J.-J., Felten, A., 2008. Polarization dependence of the C 1s X-ray absorption spectra of individual multi-walled carbon nanotubes. *Small* 4, 2279–2285.
- Nolle, D., Goering, E., Tietze, T., Schütz, G., Figueroa, A., Manna, I., 2009. Structural and magnetic deconvolution of FeP/FeOx nanoparticles using x-ray magnetic circular dichroism. *New Journal of Physics* 11, 033034.
- Patrick, R.A.D., van der Laan, G., Henderson, C.M.B., Kuiper, P., Dudrik, E., Vaughan, D.J., 2002. Cation site occupancy in spinel ferrites studied by X-ray magnetic circular dichroism: developing a method for mineralogists. *European Journal of Mineralogy* 14, 1095–1102.
- Pellegrin, E., Hagelstein, M., Doyle, S., Moser, H.O., Fuchs, J., Vollaith, D., Schuppler, S., James, M.A., Saxena, S.S., Niessen, L., Rogojana, O., Sawatzky, G.A., Ferrero, C., Borowski, M., Tjereberg, O., Brookes, N.B., 1999. Characterization of nanocrystalline g-Fe₃O₄ with synchrotron radiation techniques. *Physica Status Solidi B* 215, 797.
- Pérez, N., Bartolomé, F., García, L.M., Bartolomé, J., Morales, M.P., Serna, C.J., Labarta, A., Batlle, X., 2009. Nanostructural origin of the spin and orbital contribution to the magnetic moment in Fe₃-xO₄ magnetite nanoparticles. *Applied Physics Letters* 94 (093108), 1–3.
- Simpson, E.T., Kasama, T., Pósfai, M., Buseck, P.R., Harrison, R.J., Dunin-Borkowski, R.E., 2005. Magnetic induction mapping of magnetite chains in magnetotactic bacteria at room temperature and close to the Verwey transition using electron holography. *Journal of Physics Conference Series* 17, 108–121.
- Staniland, S., Ward, B., Harrison, A., van der Laan, G., Telling, N., 2007. Rapid magnetosome formation shown by real-time x-ray magnetic circular dichroism. *Proceedings of the National Academy of Sciences of the United States of America* 104, 19524–19528.
- Staniland, S., Williams, W., Telling, N., van der Laan, G., Harrison, A., Ward, B., 2008. Controlled cobalt doping of magnetosomes in vivo. *Nature Nanotechnology* 3, 158–162.
- Staniland, S.S., Moisesescu, C., Benning, L.G., 2010. Cell division in magnetotactic bacteria splits magnetosome chain in half. *Journal of Basic Microbiology* 50, 392–396.
- Söhr, J., 1991. NEXAFS spectroscopy. *Springer Tracts in Surface Science*, 25. Springer, Berlin.
- Söhr, J., 1999. Exploring the microscopic origin of magnetic anisotropies with X-ray Magnetic Circular Dichroism (XMCD) spectroscopy. *Journal of Magnetism and Magnetic Materials* 200, 470–497.
- Söhr, J., Siegmund, H.C., 2006. *Magnetism: From Fundamentals to Nanoscale Dynamics*. Springer Series in Solid-State Sciences. Springer, Berlin.
- Thomas-Kepra, K.L., Bazylinski, D.A., Kirschvink, J.L., Clemett, S.J., McKay, D.S., Wentworth, S.J., Vali, H., Gibson Jr., E.K., Romanek, C.S., 2000. Elongated prismatic magnetite crystals in ALH84001 carbonate globules: potential Martian magnetofossils. *Geochimica et Cosmochimica Acta* 64, 4049–4081.
- Toner, B., Fakra, S., Villabos, N., Warwick, T., Sposito, G., 2005. Spatially resolved characterization of biogenic manganese oxide production within a bacterial biofilm. *Applied and Environmental Microbiology* 71, 1300–1310.
- Weiss, B.P., Kim, S.S., Kirschvink, J.L., Kopp, R.E., Sankaran, M., Kobayashi, A., Komeili, A., 2004. Ferromagnetic resonance and low-temperature magnetic tests for biogenic magnetite. *Earth and Planetary Science Letters* 224, 73–89.
- Yano, J., Kern, J., Irgang, K.D., Latimer, M.J., Bergmann, U., Glaziel, P., Pashkar, P., Biesiadka, J., Loll, B., Sauer, K., Messinger, J., Zouni, A., Yachandra, V.K., 2005. X-ray damage to the Mn₂C₄ complex in single crystals of photosystem II: A case study for metalloprotein crystallography. *Proceedings of the National Academy of Sciences of the United States of America* 102, 12047–12052.

Chapter 4

Anomalous Magnetic Orientation in Single Cell Magnetosome Sub-chains

This chapter discusses results for the STXM-XMCD experiments of a sub-population of MV-1 where sub-chains or no magnetosome chains are present. An observation of anomalous reversed sub-chain magnetic orientation in a single cell is discussed in the context of magnetosome formation and organization. A mechanism is proposed for the formation of anomalous magnetic oriented sub-chains in individual cells.

MV-1 cells were cultured and deposited on to grids by Prof. Dennis Bazylinski and Dr. Christopher Lefèvre. TEM measurements were performed by the author with the help of Marcia Reid. STXM-XMCD measurements were made by the authors and Prof. Adam Hitchcock at the Canadian Light Source and Advanced Light Source. The author of this thesis analyzed the data and wrote the first draft of the manuscript which was edited by Profs. Adam Hitchcock and Dennis Bazylinski. The manuscript has been submitted to PLoS ONE and is under review.

The prior published evidence indicates that all magnetosomes within a magnetotactic bacterium are magnetically oriented in the same direction. This evidence supports the magnetoaerotactic model; by forming a single magnetic dipole MTB may assist the aerotactic process which allows for cells to navigate to a chemically preferred environment. However it has been noted that some cells of the cultured magnetotactic bacterium *Candidatus Magnetovibrio blakemorei* strain MV-1 are known to have relatively wide gaps between groups of magnetosomes but still maintain the overall linear arrangement of the magnetosomes along the long axis of the cell. Much of the current work in understanding the magnetism of magnetosome chains has dealt with magnetosome chains that are straight and continuous despite the presence of a significant population of cells with discontinued or even no magnetosome chains. This study investigated the magnetic moment orientation of magnetosomes in individual cells of MV-1 using Fe 2p X-ray magnetic circular dichroism (XMCD) spectra measured with scanning transmission X-ray microscopy (STXM). We observed a significant number of cases in which there are sub-chains in a single cell, with spatial gaps between them, in which one or more chains are magnetically oriented opposite to the other sub-chains in the same cell.

4.1 – Magnetic Orientation Reversal of MV-1 cells

Figure 4-1 shows a STXM image of a typical population of cells of MV-1 from a cultured sample. The image was recorded in transmission using a photon energy of 709.8 eV, the peak of the Fe 2p_{3/2} signal for magnetite, and converted to optical density (OD) using the intensity in areas without cells in this image. Within a typical distribution there are many cells without magnetosomes. Furthermore, those cells with magnetosomes present occasionally have multiple sub-chains separated by spatial gaps. It is possible that the images capture MTB cells in the process of recruiting magnetosomes to mid-cell to form a single chain.

However, the images indicate that the magnetosomes are at or near single domain size. Thus they are mature and have already adopted a magnetic orientation which may be oriented oppositely to other magnetosomes in the cell. The frequency of cells without magnetosomes and those with interrupted chains was measured from this image and ones similar in order to gain a quantitative analysis of the diversity of magnetosomes in cells. Some cells were not included in the counting statistics as it was impossible to visually distinguish one cell from another (indicated by red question marks). Cells with visible gaps are indicated by arrows. In a sampling of 351 cells, 29% had no magnetosomes and 39% had gaps in their magnetosome chains.

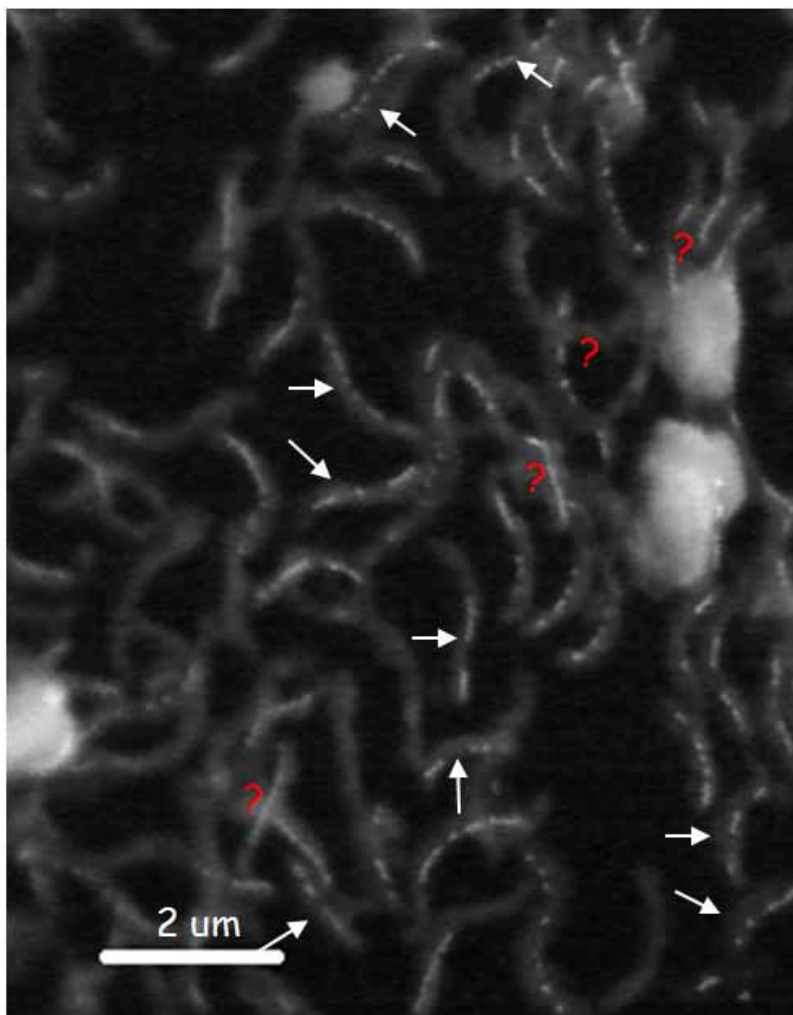


Figure 4-1 – A typical distribution of cultured MV-1 cells is shown in this STXM image (709.8 eV). Cells with magnetosome chains that have gaps are indicated by the arrows. It is difficult to distinguish the identity of one cell from another; these are indicated by question marks and were not used in statistical studies.

The percentage of cells with no magnetosomes or with magnetosome gaps represents 68% of the total sample; it is not expected that such a large portion of the population is still in the process of creating single magnetosome chains since the culture was sampled from the aerotactic band.

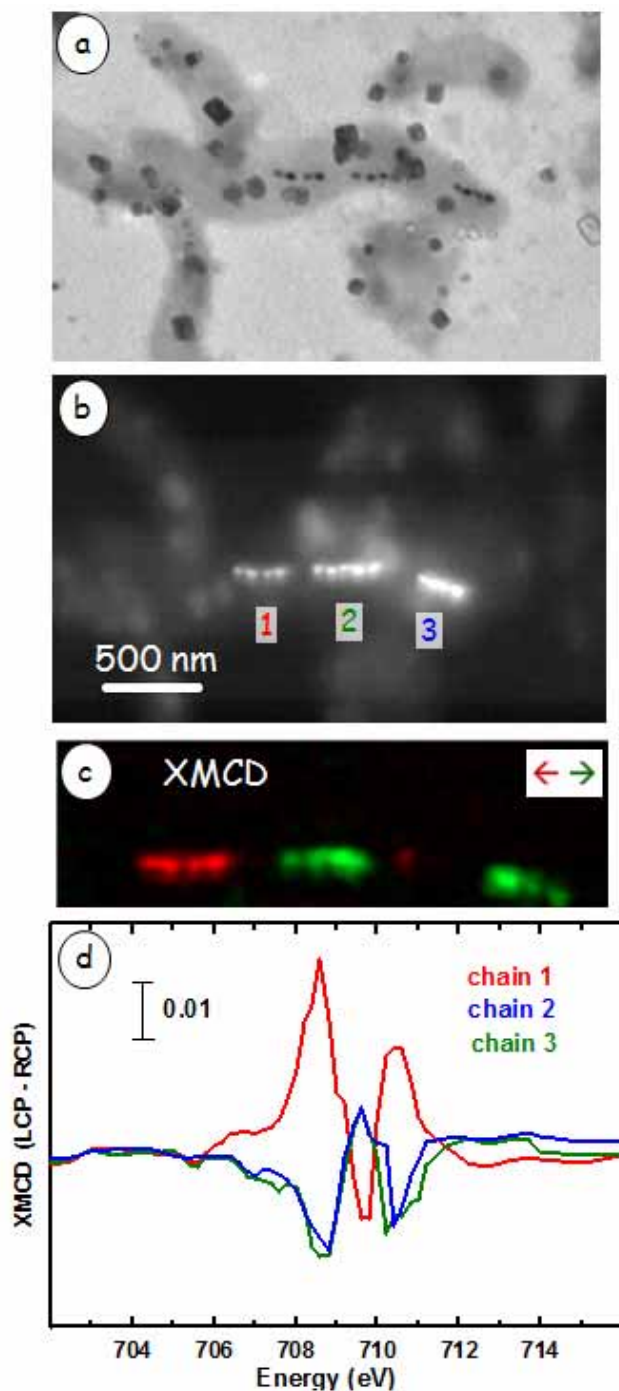


Figure 4-2 – a) a) TEM image of a cell showing gaps in the magnetosome chain. The rectangular dark objects are salt crystals from the growth medium. b) STXM image at 709.8 eV of the identical region. c) Color coded composite of the XMCD signal from the magnetosome chain. d) XMCD spectra of the 3 sub-chains.

Figure 4-2a shows a TEM image of an individual MV-1 cell while figure 4b is the corresponding STXM image of the same cell at 709.8 eV, the peak of the Fe L₃ signal. There are three magnetosome sub-chains in this cell, with gaps between them. The XMCD map of the three sub-chains (Figure 4-2c) is coloured falsely to show that there is an opposite magnetic orientation between chain 1 and chains 2 and 3. Chain 1 is oriented in the left direction, and chains 2 and 3 are oriented in the right direction. This is reflected in the opposite sense of the XMCD spectra for the three sub-chains (Figure 4-2d). On average, chain 1 has a larger XMCD signal than that of chains 2 & 3. These results show a counterintuitive example of magnetosome chain organization and alignment. Since the magnetosome sub-chains are oriented in opposite directions, the total magnetic moment will be diminished or cancelled altogether. This result brings several questions forward:

- Why are magnetosomes allowed to grow to a single domain size prior to creation of a single magnetosome chain?
- What is the model of magnetosome chain formation and organization?

Two models within the MTB community have been proposed for the dynamics of magnetosome chain formation. One postulate supports a mechanism where magnetosomes are synthesized at multiple sites and are recruited mid-cell by magnetic interactions during chain growth [SGF&06]. Alternatively, separate observations have shown that magnetosome chains are organized prior to magnetosome formation [KVB&04]. However, these studies may be dependent on the species of MTB studied. Different species may not use the same

mechanism of magnetosome formation and organization as they are related to the specific set of genes in the MAI that the species has retained and how they are expressed.

Figure 4-3a shows a single MV-1 cell containing a characteristic interrupted chain of magnetosomes. Figure 4-3b and 4-3c present the Fe $2p_{3/2}$ X-ray absorption spectra for the two chain sections, and their associated XMCD signals respectively. The spectral signals show there is an inversion of the magnetic signal of one with respect to the other. Figure 4-3d presents a color coded composite of the XMCD signals with that for the cellular material, as visualized at 704 eV, below the onset of the Fe 2p edge. This presentation clearly shows that the magnetic orientation of the chain section on the left is opposite to that of the chain section on the right. The superposition of two cells with separate chains is ruled out due to the pre-edge average image (blue in Fig. 2d) which is sensitive to the cell density. If two cells were superimposed in this image the pre-edge signal at the intersection would be larger than at the ends of the chain where the image is clearly that of an individual cell.

Of the single-cell reversed magnetic orientations observed, all have occurred when there are sub-chains separated by a distance. Magnetostatics and improper magnetosome recruitment may be the reason for these observations. From a 150 cell subset sample for which the XMCD was measured, there were 6 cells containing two or more sub-chains of magnetosomes with opposite magnetic polarities, resulting in a frequency of magnetic anomalies of 4.0 ± 0.2 % of the

total cell population, and a $9.9 \pm 0.4\%$ frequency with respect to those cells with magnetosome chain gaps. However, because the XMCD experiment yields magnetic information only for horizontally oriented chains (the XMCD intensity drops by the cosine of the deviation from horizontal) our frequency is an underestimation. We estimate that the XMCD signal can only be observed if the chain is horizontal within $\pm 20^\circ$ due to this attenuation and the statistical limits of our measurements. Taking into account this factor, the estimated frequency of this phenomenon for MV-1 would increase from $4.0 \pm 0.2\%$ to $18.0 \pm 0.9\%$ when considering the whole population of MV-1 and from $9.9 \pm 0.4\%$ to $44.6 \pm 1.8\%$ for MV-1 cells with magnetosome chains containing gaps. Furthermore Distances were calculated from the image shown in figure 4a. Distances of the gaps from left to right in figure 4a are 107 ± 8 nm and 96 ± 8 nm. Calculations based on a simple point magnetization model were performed using the chain setup seen in figure 4a. They show that the field at “magnetosome e” in chain 2 is approximately 9.6×10^6 A/m in the direction of its experimentally determined moment. Without the presence of “magnetosome f” the field at the magnetosome would be 2.8×10^6 A/m in the opposite direction of the moment. In the absence of a correspondingly oriented magnetosome, this field should be strong enough to reorient “magnetosome e” according to prior studies on the magnetic hysteresis of magnetosomes [DMF&98]. This suggests that the magnetosomes sub-chains may have nucleated and became full sized at larger distances than observed, and migrated only after reaching maturity.

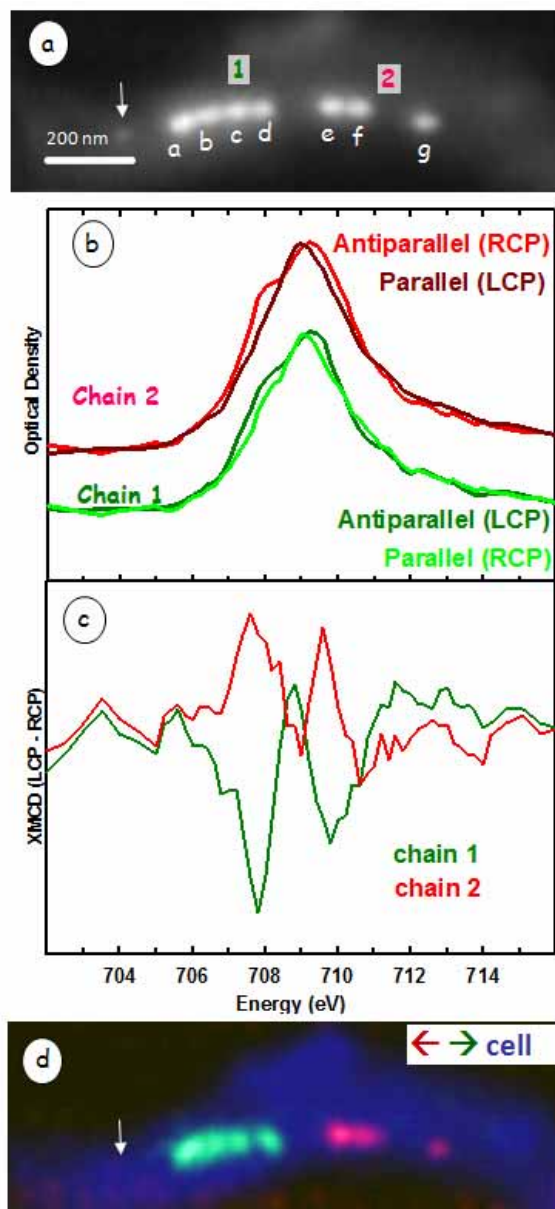


Figure 4-3 - a) STXM image (OD) of a single MV-1 cell that has a chain of magnetosomes containing two gaps. The two sub-chains are labelled chain 1 and chain 2. Each magnetosome has been labelled a-g. b) Fe $2p_{3/2}$ spectra from the left chain (upper) and the right chain (lower) recorded with the two circular polarizations. c) XMCD signals derived by subtracting the two circular polarization spectra. d) Color coded composite of the cell (OD image at 704 eV) (blue), magnetosomes with a leftward polarization (green), and a rightward polarization (red). The arrows in Figs a and d indicate a ‘pre-magnetosome’ – see text.

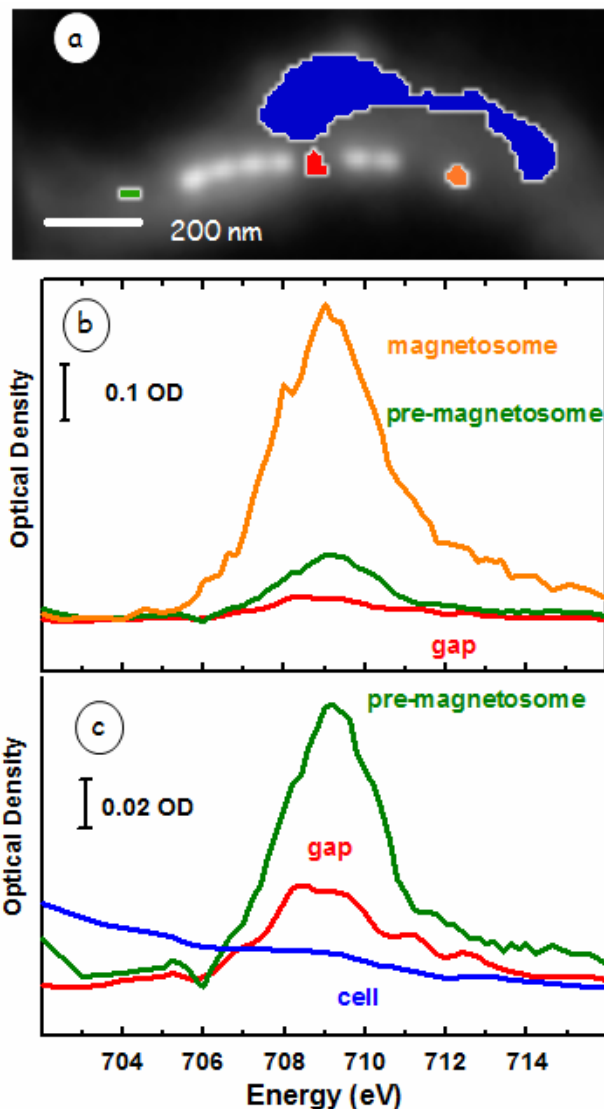


Figure 4-4 – a) STXM image at 709.8 eV of a cell with two gaps along the magnetosome chain. (b) Fe 2p_{3/2} spectra (average of left and right circular polarization data) of different regions of the cell: a single magnetosome (pink), the first gap (red), the “pre-magnetosome” (green), and the cytoplasm of the cell (blue) away from the magnetosome chain. (c) Expansion of the gap and pre-magnetosome spectra. The vertical lines indicate energies traditionally associated with Fe(II) and Fe(III) oxidation state signals.

The Fe $2p_{3/2}$ spectrum of the gap between two magnetosome sub-chains (red); that of an immature, possibly super-paramagnetic, magnetosome crystal (green); that of the cell cytoplasm (blue), and that of a single magnetosome (orange), are compared in Figure 4-4. This comparison shows that there is more iron within the gap than in the parts of the cell outside the magnetosome chain. Furthermore the spectral shape of the iron within the gap is distinct from that of the mature and immature magnetosome magnetite crystals. The intensity at 708.3 eV and 709.4 eV are traditionally associated with Fe(II) and Fe(III) oxidation states respectively (although the spectra of pure Fe(II) and pure Fe(III) species contain some signal at each energy). The gap area shows a higher Fe(II) content than the mature magnetosome crystal, which matches well with reference magnetite [GGL&06], or the immature magnetosome crystal, which has a similar Fe L_3 spectral shape to the mature one but is non-magnetic (zero XMCD).

It is possible that there is a physical blockage, for instance by lipids such that the magnetosome sub-chains are not able to coalesce with an external force. This has been postulated previously by Komeili [K07]. The excess iron present within the gap suggests that this is possible. Furthermore the iron content in the gap suggests that magnetosome synthesis may have been occurring and that a magnetosome organelle is creating the gap. However, TEM thin sections of cells with gapped magnetosome sub-chains did not show any evidence of magnetosome membrane formation.

4.3 – Proposed mechanisms of orientation reversal and insights into magnetosome chain formation

The finding of magnetotactic bacterial cells containing small chains of magnetosomes of opposite polarity has not been reported previously. Present understanding of the function of the magnetosome chain in magnetotactic bacteria states that the magnetosome chain aligns in a single magnetic orientation [BF04] however our results suggest that it is possible for a small subset of cells to obtain the opposite orientation. This brings to question the importance of magnetoaerotaxis and whether it is the primary function of magnetosome formation. If the number of magnetosomes in each section is approximately the same, the opposite magnetic orientation of the two chain sections would lead to a cancellation of their magnetic moments. Thus the net magnetic moment of the cell would be much smaller, possibly to the point where the interaction with the earth's magnetic field would be insufficient to impose an alignment of the cell for magnetoaerotaxis. While this may be detrimental to the individual cell, since there are a large fraction of cells without any magnetosomes at all, it is not a fatal situation. It is possible to postulate some models which are consistent with the observed results.

The calculated field caused by sub-chain 1 at “magnetosome e” is insufficient to cause re-orientation, however if the picture was static, and the magnetosomes were nucleated where they are seen in figure 4-4a then all magnetosomes would have adopted a single orientation as they grew into single domain. These

observations indicate that magnetosome particles may have well spaced nucleation sites or be inherited during cell splitting when cells are elongated and field strengths are not high enough to cause preferential alignment of magnetic moments. Furthermore, it indicates that, for the magnetosome sub-chains to not be influenced by neighbouring sub-chains and re-orient, the sub-chain must consist of more than one magnetosome to maintain the opposing orientation by creating a large enough local magnetic field. Lastly, the final observed sub-chain distances in the cases presented here signify that there is likely active transport of magnetosomes using non-magnetostatic interactions. Previous studies have shown that proteins allow for and are necessary for correct magnetosome chain formation via a non-magnetostatic magnetosome formation [KLN&06].

Largely separated nucleation sites offer independent growth of magnetosomes which would allow for independent orientation of each magnetosome (or magnetosome sub-chain) prior to coalescence into a single chain. If the distances between nucleation sites are large enough, a pre-existing chain would have no effect on magnetosomes forming at other nucleation sites provided there is an appropriate separation distance. The newly forming magnetosome crystal would have a 50:50 chance of being of either polarity. Those that form adjacent, or within the range where the magnetostatic interaction is large enough to coerce newly formed magnetosomes, form a chain with the same polarity. It may be that the magnetic field from one sub-chain at another magnetosome that is separated from the chain by a gap is too small for one chain to affect the magnetic

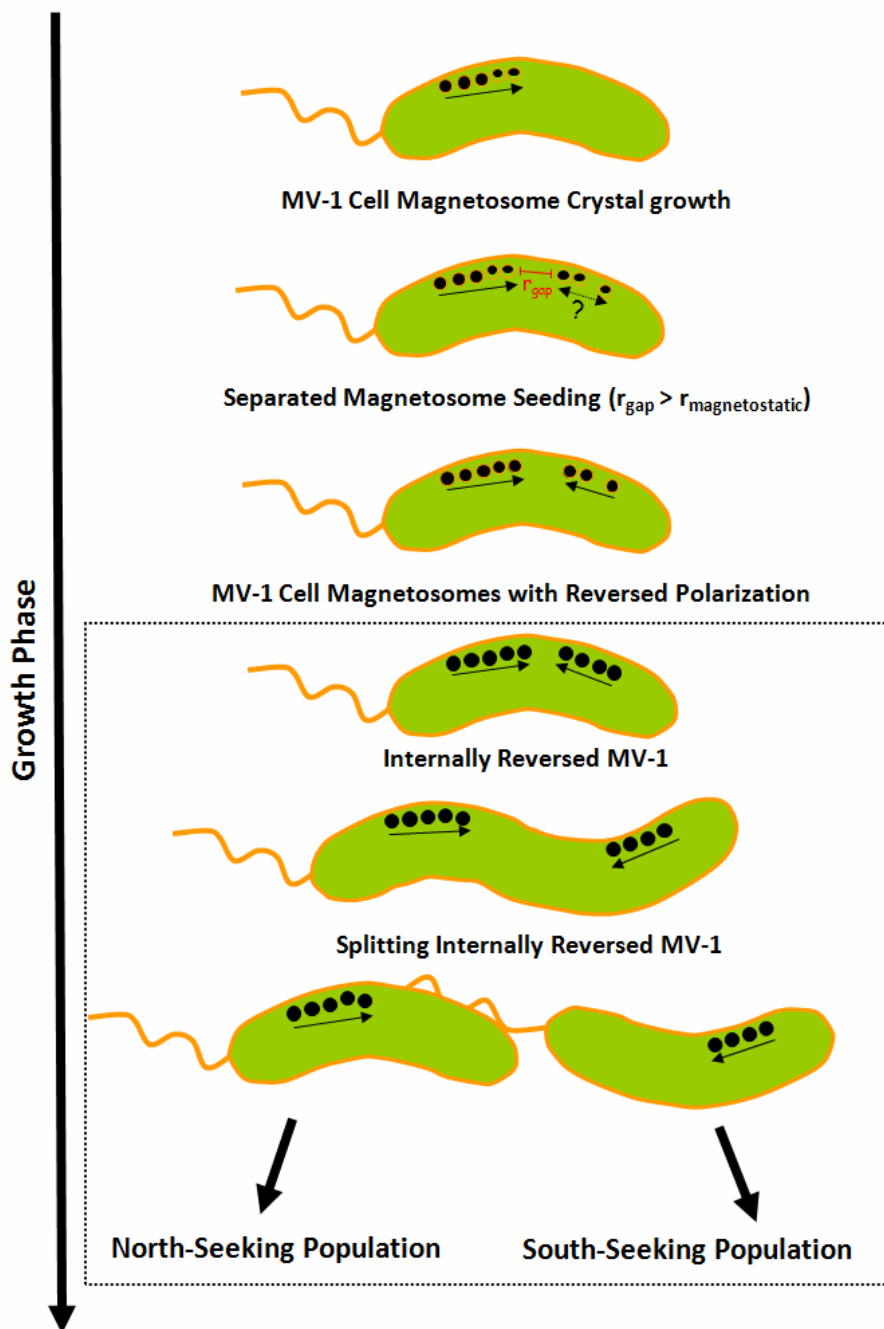


Figure 4-5 – Model of magnetosome magnetic orientation reversal in MV-1. Cells have multiple nucleation sites where the distances separating them overcome magnetostatic interactions. It is possible that once these cells with reversed magnetosome sub-chains split, they lead to two populations, one of which may exhibit south-seeking behaviour (dashed box).

orientation on the opposite chain. It is difficult to tell from the XMCD maps, as compared to higher resolution XMCD stacks, which were used to determine occurrences of sub-chains with opposing moments, whether the distances are sufficient to allow for magnetosome chains with opposite magnetic orientations. Komeili et al. [KLN&06] and Scheffel et al. [SGF&06] showed that, in cells of *Magnetospirillum* species, magnetosomes are localized and assembled by the filamentous actin-like protein MamK that appears to make up a prokaryotic cytoskeleton responsible for the stability of the magnetosome chain. An acidic magnetosome membrane protein, *MamJ* is responsible for anchoring the magnetosome to MamK [SGF&06]. In addition, it is thought that magnetosomes are aggregated in part by magnetic interactions [SGF&06]. However this is not suggested by our work, as multiple nucleation sites offer the chance for random orientation of magnetosomes. Furthermore magnetosome sub-chains with opposite magnetic moments are still moved closer by some action as postulated by magnetic field calculations. Cells of *Candidatus Magnetovibrio blakemorei* contain a *mamK* gene in their genome but not *MamJ*. This might suggest that the mechanism for magnetosome chain formation is slightly different in *Ca. Magnetovibrio blakemorei* from that in *Magnetospirillum* species and may be the reason for the presence of reversals between magnetosomes in MV-1. The presence of these peculiar magnetosome sub-chains with orientation reversal may help explain how south-seeking behaviour arises in a population of MTB. South-seeking behaviour refers to the unusual behaviour of a sub-population of

predominantly north-seeking MTB to have a preference to be south-seeking which is seemingly detrimental from an aerotactic standpoint. If cells accidentally adopt an oppositely aligned polarity via cell splitting of a reversed sub-chain cell presumably they would be swimming in the opposite direction. Although no evidence exists, the current thought to the south-seeking behaviour in polar MTB is by way of flagellar motion. If the flagella rotate in the opposite fashion, they will tend to swim upward. However, flagellar motion is dictated by external chemical responses suggesting that there are genetic mutations leading to this effect. In the oppositely oriented magnetosome chain model, it is possible to obtain the south-seeking behaviour with “typical” flagellar motion and oppositely oriented magnetosomes. A simple experiment to determine the orientation of magnetosomes with respect to its flagella in a south-seeking cell may shed light to this mechanism. This is outlined in Chapter 5.

Chapter 5

Summary and Future Work

The central findings of the STXM-XMCD technique for studying magnetotactic bacteria are summarized. The measurements and findings related to magnetic anomalous orientations in single cell MV-1 and its implications on magnetosome formation are also reviewed. A short proposal of future work using STXM-XMCD concludes this chapter.

5.1 – Summary of thesis studies

The previous STXM-XMCD thesis study of MTB by Karen Lam [L10] showed that it is possible to obtain XMCD information on individual single-domain magnetosome particles. Previous XMCD studies of MTB were limited to non-spatially resolved measurements [SWH&07, CSA&08, SWT&08], which only yield general information about magnetosomes. A concurrent polarization data collection scheme was used to increase the reproducibility and accuracy of STXM-XMCD measurements. The data collection method collects each polarization stack quasi-concurrently, such that the data collected for a Left Circularly Polarized stack image at one energy value is immediately followed by the Right Circularly Polarized stack image at the same energy. This was shown to be a more accurate and reproducible way to obtain XMCD information. By creating each polarization stack concurrently, it is possible to account for the optical density effects of radiation induced carbon buildup which adversely affect the XMCD spectrum.

The increased quality of XMCD measurements allows STXM to be used as a magnetically quantitative technique. As an example, the magnetic moment of two chains of MV-1 was calculated from XMCD data. Furthermore, STXM-XMCD allows for more analytical studies regarding magnetosome formation mechanisms. STXM-XMCD offers unique insight to the magnetism of MTB on the basis of a

single magnetosome (magnetically) or single cell (biochemically). Furthermore XMCD and XMCD mapping of magnetically sensitive information at the individual magnetosome level probed over many cells allows for a more general description of magnetosome formation and organization.

It was observed that significant populations of MV-1 have breakages or even no magnetosome chains within their cells. However, all of the studies regarding magnetism of magnetosome chains have been performed on single, continuous magnetosome chains or otherwise over multiple cells. STXM-XMCD was used to specifically survey the significant sub-population of cells with no chains or with chains containing gaps (sub-chains). Magnetosome sub-chains with large enough gaps occasionally show a magnetic orientation reversal with respect to one another. This result offers some insight into the mechanisms of magnetosome formation. In particular, the results suggest magnetosomes are nucleated at multiple discrete sites and that there is a process by which the magnetosomes to coalesce. Other questions may be posed from this result. In particular:

- What are the effects of a diminished or near zero cell magnetic moment on an individual cell?
- How are magnetosomes formed? Are they seeded locally and sequentially, or are they seeded at multiple nucleation sites and actively move into a single chain?

- What happens to magnetosome sub-chains of anomalous orientation MTB as they split? How are they shared between parent and daughter cell?
- What is the response of a polar MTB with a magnetosome chain that has a “reversed” orientation? Is south-seeking behaviour a property of the magnetic polarity of the cell or its flagellar motion?

Some of these questions may be answered using STXM-XMCD and could potentially be part of future studies of MTB.

5.2 – Future work

STXM-XMCD can provide insight into the origin of the south-seeking behaviour of polar MTB. The central question regarding south-seeking polar MTB is determining a mechanism leading to the observed south-seeking behaviour in polar MTB found in the northern hemisphere. Komeili has stated in his review that understanding the function of south-seeking behaviour and magnetoaerotaxis in general is one of several important issues with understanding MTB [K07]. The current postulation is that south-seeking bacteria rotate their flagella in the opposite sense from MTB moving towards magnetic north; however it is possible for MTB to be south-seeking by having the same flagellar motion but opposite orientation of the magnetosome chains. STXM-XMCD can be used to determine if the mode of south-seeking action is caused by a “reversed” magnetosome chain by measuring the moment relative to the flagella of individual south-seeking cells

and comparing that to normal north-seeking cells. If the south-seeking behaviour arises from a reversal in the magnetic polarization of the cell, every south-seeking polar MTB cell should have the opposite magnetic polarization than the north-seeking population. Flagella may be visualized using TEM by staining the sample after XMCD measurements have been performed.

5.2.1 – Magnetite and Greigite Reference Spectroscopy

Desulfamplus magnetomortis, BW-1 was the first cultured MTB that produces greigite magnetosome crystals. BW-1 was isolated, cultured and characterized by Lefèvre *et al* [LMA&11]. It has been shown that cultured BW-1 can produce both magnetite and greigite as they possess both sets of genes for production. In collaboration with Dr. D. Bazylinski, we have measured the XAS and XMCD of

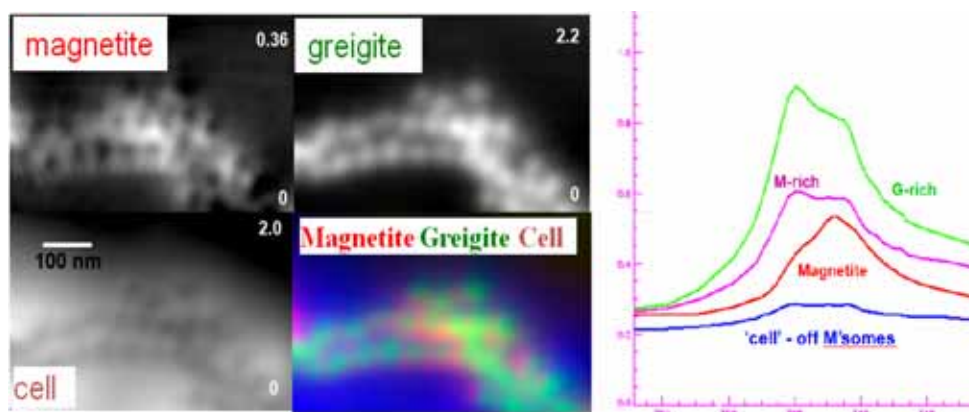


Figure 5-1 –Component structure based on the reference spectra provided on the right. The greigite reference spectrum was not available, so an internal reference was created using the assumption that the magnetosomes are half magnetite and half greigite.

cultured BW-1 that produce both sets of magnetosomes (figure 5-1). Although the average Fe L₃ spectrum of the magnetosomes is different from that of magnetite, a more definitive analysis is difficult because of the lack of reliable XAS and XMCD reference spectra of greigite.

It is important to determine the components present in the BW-1 cells both of the magnetosomes, and any other material present, such as pre-cursors. Traditional TEM diffraction studies can only determine the composition of crystals, whereas the STXM may also probe non-crystalline material that is present. An important project is obtaining the reference XAS and XMCD spectra of magnetite and greigite. Our group has obtained preliminary XAS and XMCD data for reference magnetite. Initial results of magnetite nanoparticles (Sigma-Aldrich) (figure 5-2) were obtained and compared to literature spectra. Our results show an additional peak (as opposed to a shoulder observed by Goering *et al* [GGL&06]) in the XAS of nano-magnetite occurring near ~707.8 eV. More measurements are needed in order to determine whether our results are spurious since there is a good deal of literature sources that agree with Goering *et al* [GGL&06]. Some suggestions for more accurate measurements of magnetite XAS and XMCD include:

- Measuring a sample in transmission mode
- Avoiding interaction with air causing oxidation
- Measuring a thin-film sample
- Magnetizing the sample *in situ*

By measuring a sample in transmission mode, the bulk of the sample is probed and is less sensitive to surface oxidation effects. Most literature XAS and XMCD spectra of magnetite have been measured in total electron yield mode which is more surface sensitive thus more surface oxidation sensitive. Similarly, avoiding contact with air will ensure that surface oxidation is minimal. This requires samples to be stored, transported and transferred in vacuum. Magnetization of the sample *in situ* ensures saturation magnetization of the sample as long as the field strengths at the sample are larger than 4 kG.

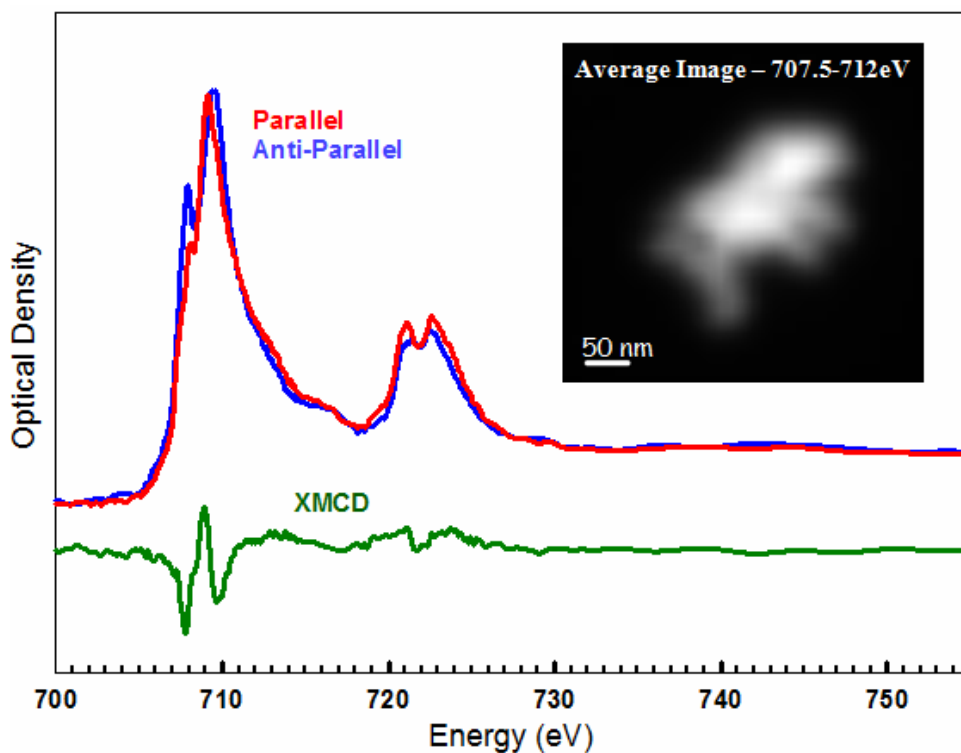


Figure 5-2 – XAS (Red, Blue) and XMCD (Green) spectra of reference XMCD from a nanomagnetite sample (Sigma-Aldrich) that was magnetized 2.5 kG. Inset shows an image of the particle that was measured.

Greigite synthesis and measurement poses additional problems due to its instability and ease of oxidation. Thus greigite must be prepared under anaerobic conditions. There are several anaerobic synthetic methods in the literature for producing greigite [W77, DS94, CRT&08].

5.2.2 – Mechanisms of Magnetosome Formation – Genetic Mutants

STXM-XMCD may be used on wild type cells and genetic mutants to understand the role of specific proteins in the mechanisms of magnetosome formation related to specific proteins. By measuring the magnetosome morphology and magnetism of individual cells of MTB with and without a specific gene, the function of that gene may be better understood. Gene deletion studies have typically used the TEM as an analytical technique to give insight into the distribution of magnetosomes and effect on organization. However, standard TEM measurements do not give information on the magnetism of the magnetosomes, which may provide useful information on the specific need for a function and its associated gene.

Preliminary studies on AMB-1 and AMB-1 Δ *MamK* have shown that the *MamK* deletion mutant have magnetosomes that are more widely dispersed in the cell. Furthermore, the XMCD shows that magnetosomes may adopt different orientations, either because of the distances between magnetosomes, or because *MamK* allows for anchoring of the magnetosome and without its presence, magnetosomes may tumble and re-orient themselves.

References

- A07** - Attwood D, 2007. Soft X-ray and Extreme Ultraviolet Radiation: Principles and Applications. Cambridge University Press: New York.
- AH08** - Ade H, Hitchcock AP, 2008. Polymer 49, 643–675.
- AHY03** - Antonov VN, Harmon BN, Yaresko AN, 2003. Phys. Rev. B 67, 024417.
- AWM03** - Arakaki A, Webb J, Matsunaga T. 2003. J. Biol. Chem. 278, 8745-8750.
- B63a** - Bellini, S, 1963a. Su di un particolare comportamento di batteri d'acqua dolce (On a unique behavior of freshwater bacteria). Institute of Microbiology, University of Pavia, Italy. internal report.
- B63b** - Bellini, S, 1963b. Ulteriori studi sui “batteri magnetosensibili” (Further studies on magnetosensitive bacteria). Institute of Microbiology, University of Pavia, Italy. internal report.
- B75** - Blakemore, RP, 1975. Science 190, 377–379.
- B82** – Blakemore RP, 1982. Annu. Rev. Microbiol. 36, 217-238.
- B95** - Bazylnski, DA, 1995. ASM News 61, 337–343.
- BB75** - Butler RF, Banerjee SK, 1975. J. Geophys. Res. 80, 4049–4058.
- BF04** - Bazylnski DA, Frankel RB, 2004. Nat. Rev. Microbiol. 2, 217-230.
- BDH&01** - Dallin LO, de Jong M, Hallin E, Lowe DS, Silzer RM, 2001. Particle Accelerator Conference 4, 2680-2682.
- BFG&88** - Bazylnski DA, Frankel RB, Garratt-Reed AJ, Mann S 1988. Nature 334, 518–519.
- BFK80** - Blakemore, R, Frankel RB, Kalmijin AJ, 1980. Nature 286, 384-385.
- BGF94** - Bazylnski DA, Garratt-Reed AJ, Frankel RB, 1994, Microsc. Res. Techniq. 27, 389-401.
- BL99** - Blatch GL, Lassel M. 1999. BioEssays 21, 932–39.

- CGP&06** - Coker VS, Gault AG, Pearce CI, van der Laan G, Telling ND, Charnock IM, Polya DA, Lloyd JR, 2006. *Environ. Sci. Technol.* 40,7745-7750.
- C54** – Calhoun BA, 1954. *Phys. Rev.* 94, 1577-1585.
- CFT&12** – Chao W, Tyliczszak T, Rekawa S, Anderson E, Naulleau P, 2012. *Optics Express* 20, 9777-9783.
- CPL&07** - Coker VS, Pearce CI, Lang C, van der Laan G, Patrrick RAD, Telling ND, Schüler D, Arenholz E, Lloyd JR, 2007. *Eur. J. Mineral.* 19, 707-716.
- CPP&08** - Coker VS, Pearce CI, Patrrick RAD, van der Laan G Telling ND, Charnock JM, Arenholz E, Lloyd JR 2008. *Am. Mineral.* 93, 1119.
- CRT&08** – Chang L, Roberts AP, Tang Y, Rainford BD, Muxworthy AR, Chen Q, 2008. *J. Geophys. Res.* 113, B06104.
- CSA&08** - Carvallo C, Sainctavit P, Arrio MA, Menguy N, Wang Y, Onanguema G, Brice-Profeta S, 2008. *Am. Mineral.* 93, 880-885.
- CTV&09** - Coker VS, Telling ND, van der Laan G, Patrrick RAD, Pearce CI, Arenholz E, Tuna F, Winpenny REP, Lloyd JR, 2009. *ACS Nano*, 3, 1922-1928.
- DB99** – Dean AJ, Bazylnski DA, 1999. *Current Micribiol.* 39, 219-225.
- DMF&98** - Dunin-Borkowski RE, McCartney MR, Frankel RB, Bazylnski DA, Pósfai M, Buseck PR, 1998. *Science*, 282, 1868-1870.
- DPH&98** – Devouard B, Posfai M, Hua X, Bazylnski DA, Frankel RB, Buseck PR, 1998. *Am. Min.* 83, 1387-1398.
- DRS92** - Donaghay PL, Rines HM, Sieburth JM 1992. *Arch. Hydrobiol. Beih. Ergebn. Limnol.* 36, 96-108.
- DS94** – Dekkers MJ, Schoonen MAA, 1994. *Geochim. Cosmochim. Acta* 58, 4147-4153.
- DZJ&99** – Dresco PA, Zaitsev VS, Gambino RJ, Chu B, 1999. *Langmuir* 15, 1945-1951.
- FB80** - Frankel, RB, Blakemore, RP, 1980. 15–18, 1562–1564.
- FB94** - Frankel, RB, Bazylnski, DA, 1994. *Hyperfine Interactions* 90, 135–142.
- FBM&07** - Faivre D, Böttger L, Matzanke B, Schüler D 2007. *Angew. Chem. Int. Ed.* 46, 8647–8652

- FBT&81** - Frankel RB, Blakemore RP, Torres de Araujo FF, Esquivel DMS, Danon J, 1981. *Science* 212, 1269-1270
- FBW79** - Frankel, RB, Blakemore, RP, Wolfe, RS, 1979. *Science* 203, 1355–1357.
- FDG&05** - Funk T, Deb A, George SJ, Wang HX, Cramer SP, 2005. *Coord. Chem. Rev.*, 249, 3.
- FDN95** - Filipponi A, Di Cicco A, Natoli, CR, 1995. *Phys. Rev. B.* 52, 15122.
- FS08** - Faivre D, Schüler D 2008. *Chem. Rev.* 108:4875–4898.
- FSA&11** – Fischer A, Schmitz M, Aichmayer B, Fratzl P, Faivre D. 2011. *J. R. Soc. Interface* 8, 1011-1018.
- G05** - Gitai Z 2005. *Cell* 120, 577–586.
- GGL&06** – Goering EJ, Gold S, Lafkoti M, Schuetz G, 2006. *Europhys. Lett.* 73, 97-105.
- GLG&07** – Goering EJ, Lafkoti M, Gold S, Schuetz G, 2007. *J. Mag. Magn. Mat.* 310, e249-e251.
- GRS&12** - Goldhawk DE, Rohani R, Sengupta A, Gelman N, Prato FS, 2012. *WIREs Nanomed Nanobiotechnol.* 4, 378-388.
- H00** - Hitchcock AP, 2000. *J. Electron Spectroscopy Rel. Phenom.* 112, 9-29.
- HBG&91** - Heywood, BR, Bazylinski, DA, Garratt-Reed, AJ, Mann, S, Frankel, RB, 1991. *Naturwissenschaften* 77, 536–538.
- J08** - Junge K. 2008. Die Funktion der CDF-Transporter MamB und MamM beim magnetosomalen Eisentransportin *Magnetospirillum gryphiswaldense*. Doctoral thesis. Univ. Bremen. Ger. 141 pp.
- JS09** – Jogler C, Schüler D 2009. *Annu. Rev. Microbiol.* 63, 501-521.
- JKS&09** – Jogler C, Kube M, Schübbe S, Ullrich S, Teeling H, Bazylinski DA, Reinhardt R, Schüler D, 2009. *Environ. Microbiol.* 11, 1266-1267.
- JWF&00** - Jacobsen C, Wirick S, Flynn G, Zimba CJ, 2000. *Microscopy.* 197, 173-184.
- K07** – Komeili A. 2007. *Annu. Rev. Biochem.* 76, 351-366.
- KVB&04** - Komeili A, Vali H, Beveridge TJ, Newman DK. 2004. *Proc. Natl. Acad. Sci. USA* 101, 3839–3844

- KLN&06** - Komeili A, Li Z, Newman DK, Jensen GJ. 2006. *Science* 311, 242–45.
- KLB&12** – Kalirai S, Lam KP, Bazylinski DA, Lins U, Hitchcock AP, 2012. *Chemical Geology* 300-301, 14-23.
- L10** – Lam KP, 2010. “XMCD of individual magnetosomes in magnetotactic bacteria using STXM”, Thesis. McMaster University: Hamilton.
- LFB11** - Lefèvre CT, Frankel RB, Bazylinski DA, 2011. Magnetotaxis in Prokaryotes. eLS (submitted).
- LJG&05** - Lerotic M, Jacobsen C, Gillow JB, Francis AJ, Wirick S, Vogt S, Maser J, 2005. *J. Elect. Spectrosc. Relat. Phenom.* 144, 1137–1143.
- LHO&10** – Lam KP, Hitchcock AP, Obst M, Lawrence JR, Swerhorne GDW, Leppard GG, Tyliczszak T, Karunakaran C, Wang J, Kaznatcheev K, Bazylinski DA, Lins U., 2012. *Chemical Geology* 270, 110-116.
- LMA&11** - Lefèvre, CT, Menguy N, Abreu F, Lins U, Posfai M, Prozorov T, Pignol D, Frankel RB, Bazylinski DA, 2011. *Science* 334, 1720-1723.
- MF89** - Mann S, Frankel RB, 1989. *Biom mineralization: Chemical and Biochemical Perspectives*, eds. Mann, S., Webb, J. & Williams, R. J. P., VCH Publishers, New York, 389–426.
- MM00** – Muxworthy AR, McClelland E, 2000. *Geophys. J.Int.* 140, 101-114.
- MSC&03** – Morrall P, Schedin F, Case GS, Thomas MF, Dudzik E, van der Laan G, Thornton G, 2003. *Phys. Rev. B.* 67, 214408.
- KSD&97** – Kuiper P, Searle BG, Duda LC, Wolf RM, van der Zaag PJ, 1997. *J. Elect. Spec. Rel. Phenom.* 86, 107-113.
- PBG&09** – Pérez N, Bartolomé F, García LM, Bartolomé J, Morales MP, Serna CJ, Labarta A, Batlle X, 2009. *Appl. Phys. Lett.* 94, 093108.
- PDM&95** - Penninga I, deWaard H, Moskowitz BM, Bazylinski DA, Frankel RB 1995. *J. Magn. Magn. Mater.* 149, 279–286.
- PSB&06** - Pradel N, Santini CL, Bernadac A, Fukumori Y, Wu LF. 2006. *Proc. Natl. Acad. Sci. USA.* 103, 17485–17489.
- PSM&95** - Proksch RB, Schäffer TE, Moskowitz BM, Dahlberg ED, Bazylinski DA, Frankel RB 1995. *Appl. Phys. Lett.* 66, 2582–2584.
- PVH&02** - Pattrick RAD, van der Laan G, Henderson CMB, Kuiper P, Dudzik E, Vaughan DJ, 2002. *Eur. J. Mineral.* 14, 1095-1102.

- RA00** - Rehr, J.J., Albers, R.C., 2000. *Rev. Mod. Phys.* 72, 621-654.
- S92** – Stohr J, 1992. *NEXAFS Spectroscopy*. Springer-Verlag: Berlin.
- SGF&06** - Scheffel A, Gruska M, Faivre D, Linaroudis A, Plitzko JM, Schüler D 2006. *Nature* 440, 110–114.
- SMB&90** - Sparks NH, Mann CS, Bazylinski DA, Lovley DR, Jannasch HW, Frankel RB 1990. *Earth Planet. Sci. Lett.* 98, 14–22.
- SB06** - Spring S, Bazylinski DA, 2006. Chapter 2 – Magnetotactic Bacteria. In: *The Prokaryotes* Editors: Falkow S, Rosenberg E, Schleifer KH, Stackebrandt E, Dworkin M. Volume 2. 842-862. [Online]
- SBE06** - Simmons SL, Bazylinski DA, Edwards KJ, 2006. *Science*. 311, 371-374.
- SRA&95** - Szabinsky SI, Rehr JJ, Ankudinov A, Albers RC, Eller MJ, 1995. *Phys. Rev. B.* 52, 2995-3009.
- SS06** - Stohr J, Siegmann HC, 2006. "Magnetism: From fundamentals to nanoscale dynamics". Springer-Verlag: New York.
- SSF&04** – Simmons SL, Sievert SM, Frankel RB, Bazylinski DA, Edwards KJ, 2004. *Appl. Environ. Microbiol.* 70, 6230-6239.
- SSP&06** - Smith MJ, Sheehan PE, Perry LL, O'Connor K, Csonka LN, Applegate BM, Whitman LJ, 2006. *Biophys. J.* 91, 1098-1107.
- SWH&07** - Staniland S, Ward B, Harrison BA, van der Laan G, Telling N, 2007. *Proc. Natl. Acad. Sci. USA* 104, 19524-19528.
- SWT&08** – Staniland S, Williams SW, Telling N, van der Laan G, Harrison A, Ward B, 2008. *Nat. Nanotechnol.* 3, 158-162.
- ST03** - STXM 5.3.2 User Manual, Advanced Light Source, Berkeley California, (version April 2003).
- TBS&94** - Thornhill RH, Burgess JG, Sakaguchi T, Matsunaga T, 1994. *FEMS Microbiol. Lett.* 115, 169-176.
- TCC&09** - Telling ND, Coker VS, Cutting RS, van der Laan G, Pearce CI, Patrick RAD, Arenholz E, Lloyd JR, 2009. *Appl. Phys. Lett.* 95, 163701-163703.
- UKS&05** - Ullrich S, Kube M, Schubbe S, Reinhardt R, Schüler D 2005. *J. Bacteriol.* 187, 7176–84.
- VT91** - van der Laan G, Thole BT, 1991. *Phys. Rev. B* 43, 13401-13411.
- W77** – Wada H, 1977. *Bull. Chem. Soc. Jap.* 50, 2615-2617.

WTP87 – Wolfe RS, Thauer RK, Pfenning N, 1987. FEMS Microbiol. Lett. 45, 31-35.